Year : 2017

Characterizing Fracture Aperture and Transport Dynamics with Hydrogeophysics: Theoretical and Expérimental Advances

Shakas Alexis

UNIL | Université de Lausanne

Faculté des géosciences et de l'environnement
Institut des sciences de la Terre

Characterizing Fracture Aperture and Transport Dynamics with Hydrogeophysics: Theoretical and Experimental Advances

Thèse de doctorat

Présentée à la
Faculté des géosciences et de l'environnement
Institut des sciences de la Terre
de l'Université de Lausanne
par

Alexis Shakas

Diplôme (M.Sc.) en Géophysique Appliquée
IDEA League Joint Master Program
ETH Zürich – TU Delft – RWTH Aachen

Jury

Prof. Dr. Michel Jaboyedoff, président du jury
Prof. Dr. Niklas Linde, directeur de thèse
Prof. Dr. Klaus Holliger, Expert
Prof. Dr. Philippe Davy, Expert
Prof. Dr. Stewart Greenhalgh, Expert

Lausanne, 2017

IMPRIMATUR

Vu le rapport présenté par le jury d'examen, composé de

Président de la séance publique :	M. le Professeur Michel Jaboyedoff
Président du colloque :	M. le Professeur Michel Jaboyedoff
Directeur de thèse :	M. le Professeur Niklas Linde
Expert interne:	M. le Professeur Klaus Holliger
Expert externe :	M. le Professeur Philippe Davy
Expert externe :	M. le Professeur Stewart A. Greenhalgh

Le Doyen de la Faculté des géosciences et de l'environnement autorise l'impression de la thèse de

Monsieur Alexis SHAKAS

Titulaire d'un
Master in Applied Geophysics
de l'IDEA League (ETH Zürich, TU Delft, RWTH Aachen)

intitulée

Characterizing Fracture Aperture and Transport Dynamics with Hydrogeophysics: Theoretical and Experimental Advances

Lausanne, le 27 octobre 2017

Pour le Doyen de la Faculté des géosciences et de l'environnement

Professeur Michel Jaboyedoff

ii

Dedicated to my mother,
who didn't need to understand Maxwell's equations,
to make this possible…

Contents

List of Figures

List of Tables

Abbreviations

1D . . . . One Dimensional

2D . . . . Two Dimensional

3D . . . . Three Dimensional

BTC . . . . Breakthrough Curve

CTD . . . . Conductivity Temperature Pressure

DDA . . . . Discrete Dipole Approximation

DFN . . . . Discrete Fracture Network

EM . . . . Electromagnetic

FD . . . . Fractal Dimension

FDTD . . . . Finite-Difference Time-Domain

GPR . . . . Ground Penetrating Radar

H . . . . Hurst Exponent

LCL . . . . Local Cubic Law

pdf . . . . Probability Density Function

REV . . . . Representative Elementary Volume

RMS . . . . Root Mean Square

TE . . . . Transverse Electric

TM . . . . Transverse Magnetic

WRMSE . . . . Weighted Root Mean Square Error

Résumé

Les fractures sont omniprésentes dans la croûte terrestre. Sur une échelle de quelques cm à plusieurs km, les fractures peuvent servir de conduits ou de barrières aux écoulements des fluides et jouent un rôle majeur dans divers processus et applications comme l'extraction des eaux souterraines, la migration des contaminants dans les roches fracturées, le stockage souterrain des déchets nucléaires mais aussi la séquestration du dioxyde de carbone et le stockage géothermique. Les propriétés géométriques d'une fracture telles que les variations d'ouverture sur son plan influencent l'écoulement et le transport du fluide. Au sein d'une fracture, la caractérisation statistique des ouvertures est délicate puisque celles-ci présentent souvent une auto-affinité ; une propriété qui implique des motifs similaires à plusieurs échelles spatiales. Les expériences hydrologiques classiques par leur caractère discret sur le terrain ne fournissent pas d'informations directes sur les variations d'ouvertures. Cette limitation peut en partie être surmontée par l'hydrogéophysique qui combine des méthodes géophysiques avec des expériences hydrologiques. Dans cette étude, nous présentons des avancées expérimentales et théoriques dédiées à l'utilisation du géoradar (GPR) seul et aussi combinées avec des essais push-pull afin de caractériser plus précisément l'ouverture des fractures. Sur le plan théorique, nous avons utilisé des solutions analytiques et développé un cadre de modélisation pour simuler les réflexions GPR dans le milieu fracturé. Les fractures qui le composent sont caracterisées par des ouvertures hétérogènes mais sont intégrées dans une matrice de roche uniforme. En présence de cette hétérogénéité, nous avons démontré que les approches classiques qui reposent sur une ouverture de fracture uniforme, conduisent à des estimations fortement biaisées de l'ouverture moyenne. Ce cadre de modélisation est important pour l'utilisation du GPR dans un aquifèr fracturé mais convient également à d'autres applications, telles que l'imagerie des fractures dans le béton. Sur le plan expérimental, nous avons réalisé les premières expériences permettant la visualisation de la migration d'un traceur salin lors d'un test push-pull. Les données GPR obtenues ont permis de mesurer la dynamique du panache du traceur et de décrire la nature des fractures. De plus, elles ont mis en évidence des effets de densité qui sont délétères pour les inférences de la dynamique et des processus naturels d'écoulement, comme l'écoulement ambiant. Pour remédier à ces effets, des mesures ont été réalisées en ajoutant de l'éthanol au traceur salin afin d'obtenir une flottabilité neutre tout en conservant la conductivité électrique. La comparaison des résultats pour les deux types de traceurs montrent que l'ajout d'éthanol permet d'éliminer les effets de densité. C'est pourquoi nous suggérons que des traceurs de densité neutre soient utilisés pour les expériences hydrogéophysiques. Enfin, nous introduisons un modèle simultané qui peut simuler les expériences push-pull et GPR. Ce modèle pourrait permettre d'inférer les propriétés d'une fracture par les données réels, ce qui serait pertinent en utilisant des méthodes Markov-chain Monte-Carlo.

Mots clefs : Hydrogéophysique, GPR, push-pull, fractures, densité.

Abstract

Fractures are ubiquitous in the Earth's crust. From the scale of a few cm to several km, fractures can act as conduits or barriers to fluid flow and play a major role in several processes and applications, including groundwater extraction, contaminant migration in fractured rock, underground storage of disposed nuclear waste and sequestration of carbon dioxide, as well as geothermal heat migration. A fracture's geometrical properties such as aperture variations along its plane influence fluid flow and transport within. Nevertheless, it is a challenging task to statistically characterize aperture variations of a single fracture because these are often self-affine; a property that implies similar patterns over several spatial scales. Classical hydrological tests are spatially sparse and do not provide direct information about aperture variations. This limitation can partly be overcome by hydrogeophysics, which combines geophysical methods with hydrological experiments. Here, we present experimental and theoretical advances on the use of ground penetrating radar (GPR) alone and also combined with push-pull tests for improved fracture aperture characterization. On the theoretical aspect we used analytical solutions to develop a modeling framework that simulates GPR reflections from fractures with heterogeneous aperture distributions, embedded in a uniform rock matrix. In the presence of aperture heterogeneity in a single fracture, we demonstrate that classical aperture-inference approaches that rely on uniform fracture properties lead to biased estimates of mean aperture. The modeling framework is suitable for GPR use in fractured rock but is also suitable for other applications such as fracture imaging in concrete. On the experimental side, we present the first experiments in which the migration of a saline tracer is imaged during a push-pull test. The GPR data are informative about the dynamics of the tracer plume and the fractures involved in the experiment, but also highlight density effects that decrease our ability to infer natural flow dynamics and processes, such as ambient flow. We address the density issue by introducing a neutrally-buoyant, yet electrically conductive tracer, which consists of ethanol mixed with a saline tracer. A comparison of results from the two types of tracer tests demonstrates that the addition of ethanol diminishes the density effect; we therefore suggest that neutrally buoyant tracers should be used in hydrogeophysics. Finally, we introduce a simultaneous modeling approach that can simulate the combined experiments. The coupled model can be applied within a Markov-chain Monte-Carlo inversion of the data from the combined experiment to infer a fracture's geometric properties.

Key words: Hydrogeophysics, GPR, push-pull, fractures, density effects.

Unicentre

CH-1015 Lausanne

http://serval.unil.ch

Year : 2017

Characterizing Fracture Aperture and Transport Dynamics with Hydrogeophysics: Theoretical and Expérimental Advances

Shakas Alexis

Shakas Alexis, 2017, Characterizing Fracture Aperture and Transport Dynamics with Hydrogeophysics: Theoretical and Expérimental Advances

Originally published at : Thesis, University of Lausanne

Posted at the University of Lausanne Open Archive http://serval.unil.ch
Document URN : urn:nbn:ch:serval-BIB_220FD26BA6AF8

Year : 2017

Characterizing Fracture Aperture and Transport Dynamics with Hydrogeophysics: Theoretical and Expérimental Advances

Shakas Alexis

Shakas Alexis, 2017, Characterizing Fracture Aperture and Transport Dynamics with Hydrogeophysics: Theoretical and Expérimental Advances

Originally published at : Thesis, University of Lausanne

Posted at the University of Lausanne Open Archive http://serval.unil.ch
Document URN : urn:nbn:ch:serval-BIB_220FD26BA6AF8

Chapter 1

Introduction

The shallow subsurface is a source of freshwater and energy, it hosts ecosystems that support much of life on Earth and all agricultural activity, and also serves as a repository for anthropogenic wastes. For example, one of the sustainable development goals set by the World Health Organization (WHO), to be met by 2030, is to "Ensure the availability and sustainable management of water and sanitation for all" (WHO, 2017). Water safety plans were first introduced by WHO in 2004 and have since been implemented in 48 countries. These guidelines often concern small-scale water supply providers that are independently surveyed and exploit regional groundwater; that is, the water contained in the subsurface. Groundwater is often preferred as a source of drinking-water (Schmoll, 2006), particularly, the Swiss Federal Office for the Environment states that "more than 80% of the drinking and process water supply comes from the predominantly locally used groundwater sources" (FOEN, 2009). Therefore, characterizing the hydrogeology of a groundwater site is essential for risk assessment and safe drinking water management.

The sharp population increase, accompanied with a world wide shift to a more resource-demanding lifestyle is leading to a growing demand for energy (UN, 2017). In an increasing effort to reduce fossil fuel emissions, geothermal energy alternatives have been in the spotlight for several decades (Stauffer et al., 2013). Efficient geothermal heat extraction requires that the shallow ground and groundwater conditions are locally assessed. Formations with low permeability (e.g., crystalline rock) are usually preferred in order to prevent groundwater pollution from leakage of working fluids (Watanabe and Takahashi, 1995). A thorough understanding of the local conditions at the field-scale is necessary for assessing both the risk and potential of geothermal energy reservoirs. Nuclear energy provides another viable solution, but the issue of safe storage of spent nuclear fuel remains (Tsang et al., 2015). Planned subsurface repositories for nuclear waste are situated deep in geologic formations with low permeability, such as crystalline rock, and are designed to host the nuclear waste for thousands of years. Clearly, exhaustive planning must be made to decide on safe locations for such facilities and it is preferable to enable continuous monitoring (e.g., risk of leakage into groundwater).

Growing population and associated lifestyle changes do not only concern energy. The increasing demand for agriculture, particularly intended for meat production (Tilman and Clark, 2014), coupled with the projected growth in industrial activity (e.g., USDoE, 2016, Ch.

9) are leading to an accumulation of carbon dioxide (CO_2) in the atmosphere. One proposed way of reducing CO_2 emissions is geologic carbon sequestration; that is, the underground storage of CO_2 in stable geologic formations, such as depleted oil and gas reservoirs. Proper identification of a potential CO_2 storage site as well as site monitoring during and after CO_2 injection are critical for safe long-term storage.

Among these and other applications, such as hydrocarbon exploration or mining, the importance of improving our understanding of the properties and processes that take place in the shallow subsurface is evident. Yet, the subsurface is invisible to the eye and thus suitable disciplines have been developed to study its processes and properties. One such discipline is hydrogeophysics that involves the use of geophysical methods – techniques and instruments that map physical properties to measurable responses of the subsurface – for hydrogeologic investigations – the study of water, or more generally fluid flow and transport through geological formations – in order to better understand, characterize and even predict subsurface processes (Rubin and Hubbard, 2005).

A hydrogeophysical survey can provide quantitative information about subsurface properties and processes, which can be useful for forecasting. Fig. 1.1 presents a flow chart with the main steps involved in designing a hydrogeophysical analysis, from the onset of creating a general understanding of how subsurface processes might function, that is, from building the conceptual model (sec. 1.3) to creating a forward model (sec. 1.4). Data, observations and forward models are combined in a hydrogeophysical inversion framework. This process may be repeated until an adequate final model is decided upon, that can be used to predict the (site-specific) subsurface response. For example, a model that well describes the flow and transport properties of a fractured rock aquifer can also be effectively used to predict the spatial migration of a contaminant over time. While the model may be designed on initial assumptions and data from hydrology, geophysics can offer complementary information to further refine the model through joint or coupled inversion (e.g., Moorkamp et al., 2016, Ch. 7), to reject the model (Linde, 2014), or even select the most appropriate model through an ensemble of possibilities (Brunetti et al., 2017). Other alternatives to the work flow described in Fig. 1.1 can be found, for example, in NRC (1996, Fig. 6.1) or Ferré et al. (2009).

1.1. GPR in fractured rock hydrogeophysics

One of the central challenges in groundwater hydrology is to accurately characterize fractured rock heterogeneity (NRC, 1996; Faybishenko et al., 2005). Flow and transport in fractured rock can be very unpredictable, partly because of the highly anisotropic, multicomponent and multi-scale behavior of fractured rocks (Neuman, 2005). Obtaining sufficient information to characterize fractured rock heterogeneity through hydrological tests alone is difficult, partly because hydrological data is often spatially sparse as it is measured along boreholes. For example, artificial tracer tests involve the injection of a volume of tracer in the fractured system and its (partial) recovery, either at another location during a dipole test or at the injection location during a push-pull test (e.g., Leibundgut et al., 2011, Ch. 4). The measured tracer concentration during the recovery phase is called the breakthrough curve (BTC). Het-
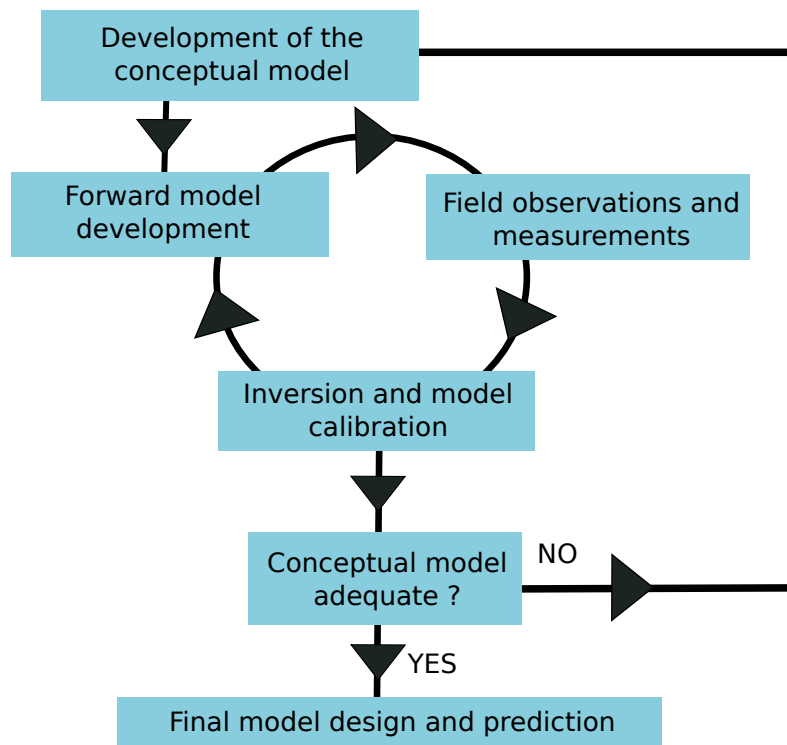
Figure 1.1 – Flow chart identifying the steps involved in the hydrogeophysical model development process. The first step is to construct a conceptual model that is a generalization of the natural system of interest, and based on that, create a forward model. Field observations and measurements are then combined with the forward model in an inversion framework to create a final model that can adequately describe the subsurface properties and processes of interest. Using the final model, predictions can be made.

erogeneities in the geometrical properties of fractures often manifest as low concentrations of tracer arriving at later times and a resulting BTC that is skewed (e.g., Moreno et al., 1990; Keller et al., 1999; Becker and Shapiro, 2000, 2003). Flow and transport modeling can be used to fit the shape of the BTC and to implicitly characterize heterogeneity (e.g., Berkowitz, 2002). Nevertheless, tracer data lack direct information, at least, about (1) the contact area between the tracer and the fracture walls (i.e., number and size of fractures involved), (2) the dynamics of the tracer away from the borehole location and (3) ambient flow in the system. Accordingly, hydrogeophysical investigations have met success since they can partially provide such complementary information through geophysical techniques (Binley et al., 2015).

The use of geophysics for hydrologic investigations has been growing over the last two decades as the potential of geophysical methods has been increasingly accepted by the hydrologic community (Ferré et al., 2009; Binley et al., 2015; Lane et al., 2016). Geophysical investigations are suitable for accompanying hydrological studies over several spatial scales, ranging from the laboratory ($\sim 10^{-3} \leftrightarrow 10^1$ m), to the local ($\sim 10^{-1} \leftrightarrow 10^2$ m) and regional ($\sim 10^1 \leftrightarrow 10^5$ m) scales (Rubin and Hubbard, 2005). Additionally, geophysical methods are often performed in a time-lapse manner (i.e., repeated measurements over time) and thus provide valuable information about dynamic changes in a hydrogeologic system.

Ground penetrating radar (GPR) has been widely used in geophysics to detect and characterize fractures. A GPR system emits a high-frequency electromagnetic (EM) wave that propagates and is scattered at interfaces of differing electrical properties (e.g., Jol, 2008). Low-loss dielectric media, such as crystalline rock permit for significant penetration depths (tenths of meters) of the GPR signal. In fractured media, the strength of the scattered signal arising from fractures depends on the fracture geometrical properties, including the orientation, size and aperture variations of the fracture as well as the electrical properties of the fracture filling. In general, fractures oriented parallel to the survey direction will provide the strongest signal but fractures oriented perpendicularly can also be detected (Tsoflias et al., 2004; Tsoflias and Hoch, 2006). Applications that utilize GPR for fracture detection vary from assessing sites for storing spent nuclear fuel (Olsson et al., 1992), quarry management (e.g., Grasmueck, 1996; Grandjean and Gourry, 1996), efficient mining (e.g., Porsani et al., 2006), assessing rock fall hazard (e.g., Jeannin et al., 2006), assessing deterioration of buildings (e.g., Leucci et al., 2007; Sambuelli and Calzoni, 2010) as well as aquifer characterization (Dorn et al., 2012).

In hydrogeophysics, time-lapse GPR is used to map dynamic changes in hydrogeological systems (e.g., Rubin and Hubbard, 2005, Ch. 7). For example, Tsoflias et al. (2001) present time-lapse changes in the reflected GPR signal caused by a pumping test in a fractured aquifer. Hydrogeophysical tracer tests that utilize electromagnetic methods usually use a saline (hence more electrically conductive) tracer to obtain a time-lapse response. Ramirez and Lytle (1986) document one of the first GPR time-lapse imaging of a saline tracer test in fractured granite. Saline tracer migration has since been imaged with cross-hole tomography (Day-Lewis et al., 2003), surface reflection (Talley et al., 2005; Tsoflias and Becker, 2008; Becker and Tsoflias, 2010) and single-hole reflection (Dorn et al., 2011) GPR, all during dipole pumping tests. Recently, saline tracer migration and associated tracer density effects were also imaged during push-pull tests (Shakas et al., 2016) and compared with similar tests performed with a neutrally buoyant saline tracer (Shakas et al., 2017).

1.2. Some properties of rock fractures

The geologic setting that we examine in this thesis is fractured rock, although some methodologies introduced (e.g., the novel neutrally buoyant tracer introduced in Chapter 5) are also applicable to other geological settings.

Fractures are discontinuities in the material properties of rocks that form primarily as a response to mechanical stress (NRC, 1996). In the simplified schematic of Fig.1.2, fracture generation is displayed as the vertical and horizontal displacement of two rough surfaces. These are often called mode I (vertical displacement) and mode II (horizontal displacement) fracturing, and mode II fractures are also called faults. The separation forms a void space that can be further altered by chemical, hydraulic or thermal processes and the fracture void can be gas filled, fluid filled, can include gouge (unconsolidated rock) or a combination of all three (NRC, 1996). During this separation, some areas of the fracture may remain in contact and form impermeable regions along the fracture plane. More importantly, mineralization
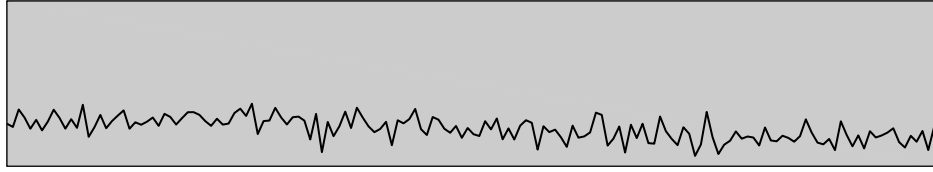
(a) An initial crack in the rock is generated as a result of mechanical stress.
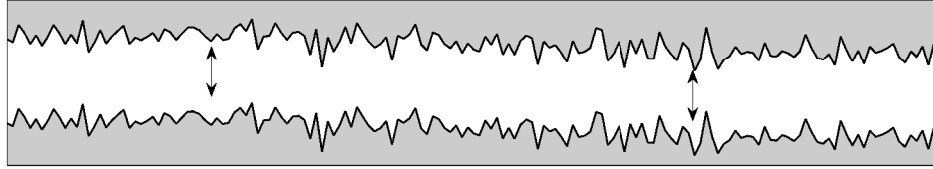
(b) A void space is generated by vertical displacement.
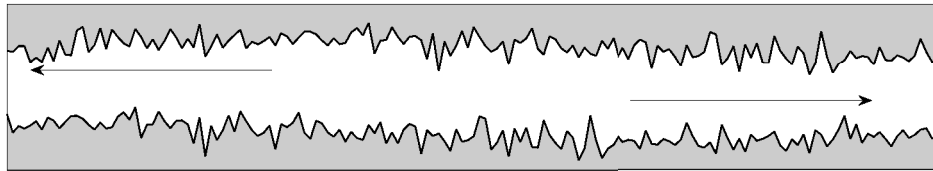
(c) Horizontal displacement generates further complexity in the void space between the two rough walls.

Figure 1.2 – Simplistic schematic of fracture generation. The scale is omitted in this figure to highlight the scale-invariance of this process.

can form in the later stage of fracture development and can increase the total fracture surface that is impermeable considerably (NRC, 1996). Therefore, the connectivity of open void spaces along a fracture (Tsang and Tsang, 1987; Tsang et al., 1988; Tsang and Tsang, 1989; Tsang and Neretnieks, 1998; de Dreuzy et al., 2012) as well as their global connectivity in a network of fractures (de Dreuzy et al., 2001a,b, 2002) will greatly impact fluid flow within the rock.

1.2.1. Fractal geometry

The geometrical properties of fractures, such as surface roughness, aperture and length, often display similar variations across several spatial scales (Bonnet et al., 2001). For example, laboratory, field and regional measurements suggest that fracture length (e.g., Velde et al., 1991; Leary, 1991; Odling, 1997; Bour et al., 2002) can be well described by a power-law distribution, suggesting self-affinity. In a similar manner, fracture surface roughness can be described by statistically self-affine patterns over several scales (e.g., Poon et al., 1992; Odling, 1994; Schmittbuhl et al., 1995). Laboratory measurements of fracture aperture also suggest statistical similarity (Belfield, 1994; Lanaro, 2000), although such studies are less frequent because of the inherent difficulty in directly measuring fracture aperture.

Most naturally occurring patterns are best described by *fractal* geometry, a field of mathematics first introduced by Mandelbrot (1975) to describe irregular and fragmented shapes. A central notion of fractal geometry is self-similarity; that is, the exact or statistically approximate repetition of a geometrical pattern across several scales (Fisher et al., 2012, Ch. 1). This concept does not arise in traditional Euclidean geometry where shapes have a characteristic scale (e.g., radius of a circle, r), can be described by mathematical formulas (e.g., circle area, $A = \pi r^2$) and are usually smooth (i.e., differentiable) when sufficiently magnified. In an ideal case, a self-similar fractal is scale-invariant meaning that it exactly repeats itself at all spatial scales. Natural patterns, such as fracture aperture or length, have upper and lower bounds that may result from a physical origin or may appear because of limited measurement resolution (mostly lower bound) or limited sample size (mostly upper bound). This means that many natural patterns may appear fractal within a limited bandwidth (Bonnet et al., 2001).

A less restrictive notion than self-similarity that can be used to characterize fracture properties is self-affinity (Mandelbrot, 1985, 1989). Self-affinity in the aperture field can be explained as follows: considering a planar fracture in the horizontal ($x - y$) dimensions, and assuming the magnitude of the aperture is indicated by the vertical (z) dimension, an increase in the scale of the x and y axes by a factor r must be followed by a factor r^H in the z axis so that the aperture remains statistically identical (Fisher et al., 2012, Ch. 1). The x and y dimensions in this case refer to the fracture length and width. The factor H is called the Hurst exponent (Hurst, 1951), it varies between 0 and 1 and it is related to the fractal dimension (FD) for 2D shapes by $FD = 3 - H$. Self-affine aperture variations along a fracture plane imply that measurements will reveal similar patterns in laboratory, field and regional investigations, by the appropriate scaling factor H. A decreasing H will increase the fractal nature of the aperture field and an increasing H will produce smoother aperture variations at larger scales. A synthetic example showing the effect of H on fracture aperture is shown in Fig. 1.3. The aperture field is created following the formulation by Adler et al. (2012, sec. 2.2.2), described in more detail in sec. 1.4.1 and 3.3.3.

1.2.2. Fluid flow and transport in fractured media

Subsurface fluid flow and transport results from various processes at different scales (e.g., Hubbert, 1940). Nevertheless, it is sometimes possible to define a representative elementary volume (REV) below which the properties of a system may be approximated by an average (homogeneous) medium (e.g., Bear, 1972). Therefore, physical theories that use a REV rely on the notion of a continuous medium.

The concept of a REV cannot be easily applied to fractured media partly because of their fractal nature (Snow, 1969; Long et al., 1982). The latter implies heterogeneous properties over a large range of scales and results in flow and transport that deviates from idealized test-cases (e.g., Berkowitz, 2002; Faybishenko et al., 2005). For instance, heterogeneous apertures along the fracture plane can create a tortuous path that may lead to flow channeling (e.g., Moreno et al., 1990; Tsang and Neretnieks, 1998; Keller et al., 1999; Fiori and Becker, 2015; Ishibashi et al., 2015). The connectivity of fractures (primarily) along with flow channeling,
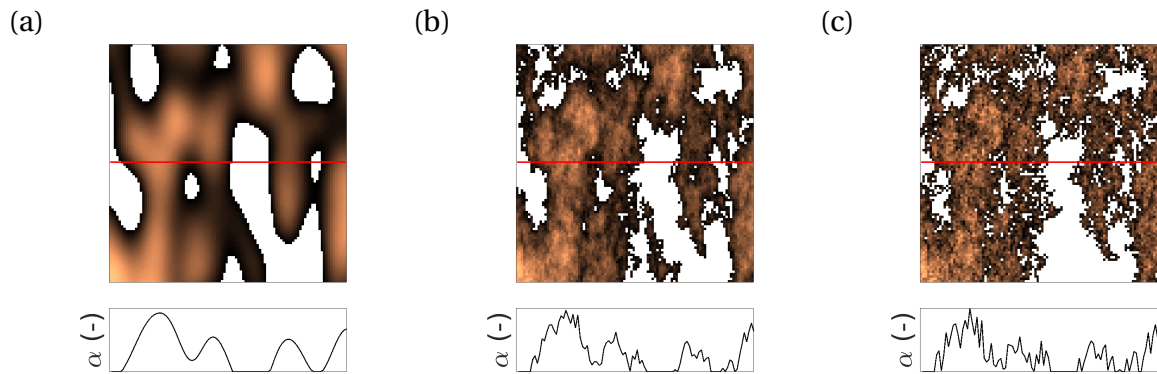
Figure 1.3 – Synthetic fracture aperture (α) along a rectangular fracture plane as a function of the Hurst exponent (H). The Hurst exponent is (a) $H = 1$, (b) $H = 0.5$ and (c) $H = 0.25$. Larger apertures are shown in lighter color than smaller apertures, and zero apertures (contact regions) are transparent. Below each fracture plane, a cross section of the aperture variation along the middle cross section of each fracture (solid red line) is plotted. No units are given along the axes to highlight the self-affine property of fracture aperture.

as well as other effects such as matrix diffusion or hydrodynamic dispersion, can lead to non-Fickian transport; that is, the deviation of transport behavior from the linear diffusion over time predicted by Fick's law (e.g., Moreno et al., 1988; Thompson and Brown, 1991; Bodin et al., 2003; Le Borgne et al., 2006; Gouze et al., 2008; Le Borgne and Gouze, 2008). Tracer tests conducted in fractured rock reveal strong non-Fickian transport characteristics that manifests as a long "tail" in the BTC (e.g., Becker and Shapiro, 2000; Kang et al., 2015). While many mechanisms have been suggested and used to reproduce the observed tailing (e.g., Berkowitz, 2002, and references therein) recent studies have shown that heterogeneous aperture (hence heterogeneous velocity fields) within a fracture can also account for the late time behavior (e.g., Wang and Cardenas, 2014; Fiori and Becker, 2015).

1.3. The conceptual model

Conceptual models are an essential building block and often the departure point of the scientific process (NRC, 1996). A conceptual model aims to identify and describe the main features of a system and serves as a premise on which further theories, often described by geometrical, physical and/or mathematical relations, are constructed. To create a conceptual model we must make some simplifications/generalizations about the complexity of the natural system. These are often derived from expert knowledge, field observations or experimental measurements and can be further refined when more knowledge is available, often following data collection or forward/inverse modeling (Fig. 1.1). For instance, a conceptual model will determine how processes (e.g., fluid flow) are affected by subsurface properties (e.g., fracture aperture).

In this thesis we seek accurate and efficient simulations of EM wave interaction with a single fracture. The fracture has heterogeneous properties (aperture and filling) along its plane and is embedded in a low-permeability rock matrix. As simplifying assumptions for the conceptual model we consider at least the following for the rock matrix:

1. **Negligible permeability.** The experiments we present herein were performed in fractured crystalline rock that is characterized by low porosity (Le Borgne et al., 2006; Ruelleu et al., 2010). In general, the permeability of crystalline rock varies from $10^{-18}\,\mathrm{m}^2$ m to $10^{-13}\,\mathrm{m}^2$ (e.g., Brace, 1984). Assuming fluid flow within the fracture can be approximated with the parallel plate model (more on this in sec. 1.4.3) with an aperture of 1 mm, the computed permeability of the fracture is $10^{-8}\,\mathrm{m}^2$.

2. **Homogeneous electrical properties.** This claim is supported by Dorn et al. (2012) who performed a cross-hole tomography study and showed that the GPR velocity is practically constant at the depth where the experiments are performed. This assumption may also be valid for several other rock settings, particularly when a limited EM frequency range is considered (e.g., Parkhomenko, 2012).

With these simplifications in mind, we can assume (1) no fluid flow in the rock matrix and (2) constant attenuation and dispersion of the GPR signal within a homogeneous rock matrix. In the following, we discuss a conceptual model that is suitable for our purpose.

Discrete Fracture Network   Fractured rock can be conceptualized in various ways, with the two end-members of the spectrum being (1) a completely uniform and isotropic continuum and (2) a highly heterogeneous, anisotropic medium with multi-scale behavior (Lee and Farmer, 1993; Neuman, 2005). One conceptual model used to describe the latter case is the notion of a Discrete Fracture Network (DFN) (Long et al., 1982).

A DFN considers fractures as the main conduits for flow and transport and the properties of the network are computed as a function of fracture aperture, length, density, orientation as well as fracture connectivity and filling material (Singhal and Gupta, 2010). Initially the use of DFN's was limited to fractures with homogeneous aperture and filling (e.g., Long et al., 1982; Dverstorp and Andersson, 1989). More advanced models account for tortuous flow paths through individual fractures (Cacas et al., 1990; Dverstorp et al., 1992) as well as transport (Cacas et al., 1990; Nordqvist et al., 1992) or retention of tracers (Cvetković et al., 2004; Cvetković and Frampton, 2012). The properties of DFN networks as a function of fracture length and permeability have also been extensively studied (de Dreuzy et al., 2001a,b, 2002). Current DFN modeling frameworks can account for fracture and network scale heterogeneities to accurately simulate flow and transport (Erhel et al., 2009; Ishibashi et al., 2012; Hyman et al., 2015). Fig. 1.4, adapted from Fig. 1 in de Dreuzy et al. (2012), shows a schematic description of 3D DFN models with the same connectivity (percolation ratio) but with decreasing (average) fracture length.

DFN's have been especially appealing for hydrogeological purposes but their use in hydrogeophysical studies has been limited. Nevertheless, geophysical techniques such as GPR hold a promising potential for imaging 3D fracture networks (e.g., Liu, 2006; Dorn et al., 2013).
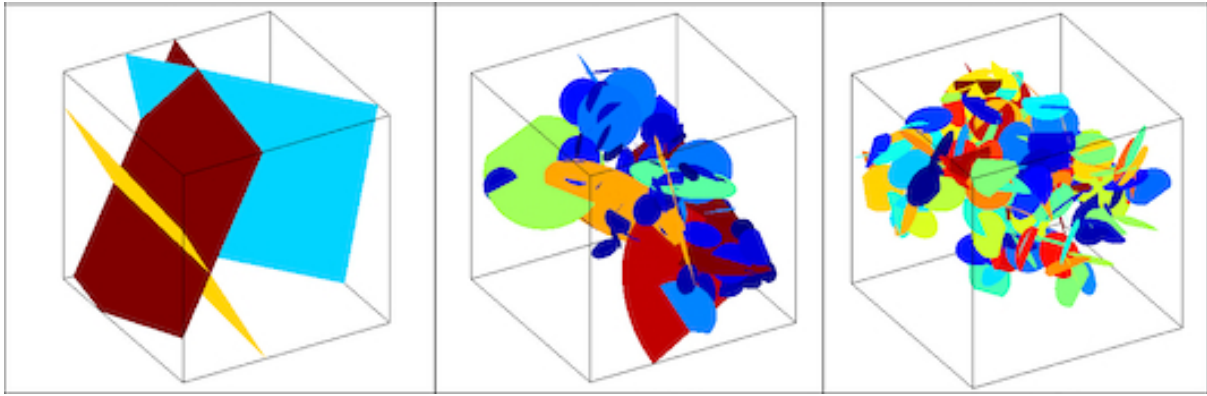
Figure 1.4 – Examples of discrete fracture networks, modified from de Dreuzy et al. (2012). The three networks have the same connectivity (percolation ratio, see reference from more details) but the average length of the fractures, here indicated with different colors, decreases from left to right.

In this thesis we adopt the DFN conceptual model for characterizing fractured rock but we focus the analysis on a single fracture within the network.

1.4. Forward modeling

Forward modeling refers here to numerical solutions that represent the response of a natural process or system. Based on either physical or empirical mathematical formulations, forward models take as input the parameters that describe a system and the experimental design (e.g., source/receiver properties). The parameters may relate directly to a physical property or indirectly on another (e.g., petrophysical) relation (Tarantola, 2005, sec. 1.3).

In an ideal scenario a forward model would precisely reproduce all the attributes in the observed data. Practically, one can never construct an exact representation of reality and therefore all forward models make approximations and assumptions that result in errors in the predicted response. In numerical implementations of forward models, additional sources of error occur such as numerical dispersion (e.g., Taflove and Hagness, 2005, Ch. 4). Additional deviations from the modeled and observed response occur because of uncertainties in the measurement process (data errors).

In this section we introduce two forward models but in the bulk of this work we focus on the latter; one for simulating flow and transport in a single fracture and another for simulating GPR reflections from fractures with heterogeneous properties. While the latter is capable of simulating the reflections arising from several fractures, the former forward model only assumes one fracture. Thus, in the following we address the properties of a single fracture.
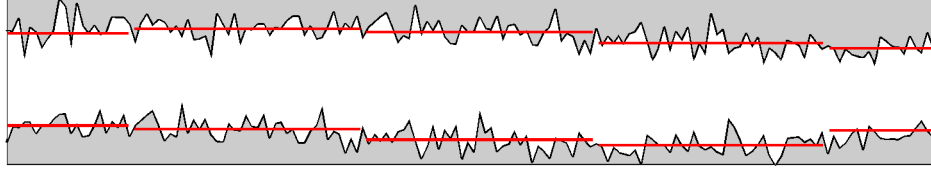
(a) Approximation of the local aperture from Fig. 1.2c as a collection of parallel plates (solid red lines).
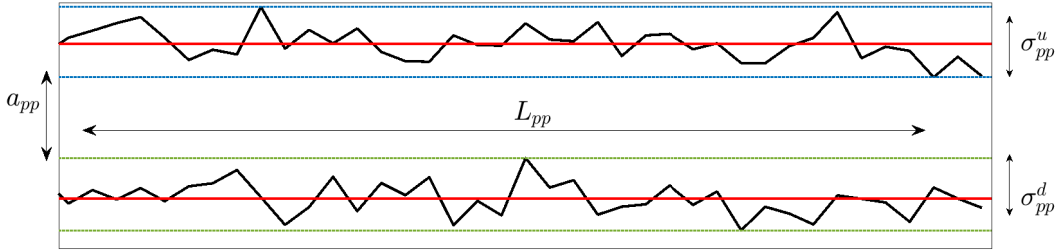
(b) Enlarged view of the middle parallel plate from (a). The separation between the plates corresponds to the averaged local aperture a_{pp} over a length L_{pp}. The roughness of the top and bottom segments of the segment are indicated by $\sigma_{\text{pp}}^{\text{u}}$ (dotted blue lines) and $\sigma_{\text{pp}}^{\text{d}}$ (dotted green lines) respectively.

Figure 1.5 – Discretization of a rough fracture with the parallel plate model.

1.4.1. Fracture properties

Fracture aperture

Local aperture can be defined as the point-wise variation in aperture along a fracture and it can be computed in several ways (Oron and Berkowitz, 1998). If the aperture variation of a real fracture could be measured and plotted on a graph of aperture size on the horizontal axis against frequency of occurrence on the vertical axis, this would provide the aperture distribution. A complete representation of the aperture distribution is practically impossible as it necessitates measurements at all spatial scales. Instead, aperture is usually measured over a truncated range and fitted with an appropriate distribution function, such as normal (Oron and Berkowitz, 1998), log-normal (Renshaw, 1995), gamma (Tsang and Tsang, 1987) or power-law (Belfield, 1994; Lanaro, 2000).

Variations in aperture can not be accounted for at all spatial scales in numerical forward models and therefore assumptions are made when simulating processes that depend on aperture variations. Here, we replace segments of a fracture with two smooth parallel plates having a fixed separation. This is shown in Fig. 1.5a for a simplified 1D fracture. In Fig. 1.5b, an enlarged view of the middle parallel plate from Fig. 1.5a is shown. Recently, we used this approach to model EM interaction with rough fractures (Shakas and Linde, 2015, 2017). Throughout this thesis we assume that a rough fracture can be approximated as a collection of parallel plates.

Fracture aperture can be spatially correlated along the fracture plane (Brown et al., 1986; Wang et al., 1988; Lee and Farmer, 1993). Spatial correlation suggests that aperture variations are similar over distances given by the correlation length. Mathematically, spatial correlation can be imposed on the aperture field with a correlation function such as the following:

$$C_h(u, v) = \sigma_h^2 \exp\left[-\left\{ \left(\frac{u}{l_{c1}}\right)^2 + \left(\frac{v}{l_{c2}}\right)^2 \right\}^H \right], \tag{1.1}$$

that can be found, for example, in Adler et al. (2012, sec. 2.3.2). The variance of the aperture field is given by σ_h^2, H is the Hurst exponent and $\{u, v\}$ denote the lag in the two spatial dimensions along the fracture plane. Two cutoff length scales are used, l_{c1} and l_{c2} that define a threshold above which spatial correlation disappears. The use of two length scales allows for anisotropic surface creation.

Real fractures have contact regions where the aperture is zero (NRC, 1996; Singhal and Gupta, 2010). Contact regions determine the spatial distribution of interconnected channels within the fracture and therefore influence channeling (e.g., Tsang and Neretnieks, 1998) and fluid percolation; the flow of fluid all the way through the fracture's boundaries (Broadbent and Hammersley, 1957). To allow for contact regions along the fracture plane we apply the following algorithm:

1. Create two fields, using Eq. 1.1, with zero mean.
2. Align them horizontally and shift one of them vertically by a constant value corresponding to the mean aperture.
3. Set any intersecting regions (negative values) to zero (contact regions).

Fig. 1.6 shows the aperture field of a synthetic fracture created with this algorithm for three different mean apertures.

Fracture filling

The void space between the two fracture walls hosts the fracture filling. In this thesis we use a uniform discretization for the fracture plane so all parallel plates in a fracture have the same surface area. The product of this area with the plate's aperture gives the volume of the void space which we assume to be fluid filled. We define the following fluid properties for each parallel plate:

- Tracer concentration (normalized by the maximum concentration).
- Density (ρ) in $\text{kg} \cdot \text{m}^{-3}$.
- Dynamic viscosity (μ) in $\text{kg} \cdot \text{s}^{-1} \cdot \text{m}^{-1}$.
- Electrical conductivity σ (sec. 1.4.2).
- Relative electrical permittivity ε (sec. 1.4.2).

The tracer concentration will determine the fluid density , dynamic viscosity and electrical properties of each cell. In addition to the electrical properties of the fracture filling, the electrical properties of the rock matrix also need to be defined for the GPR forward model.

(a)   (b)   (c)
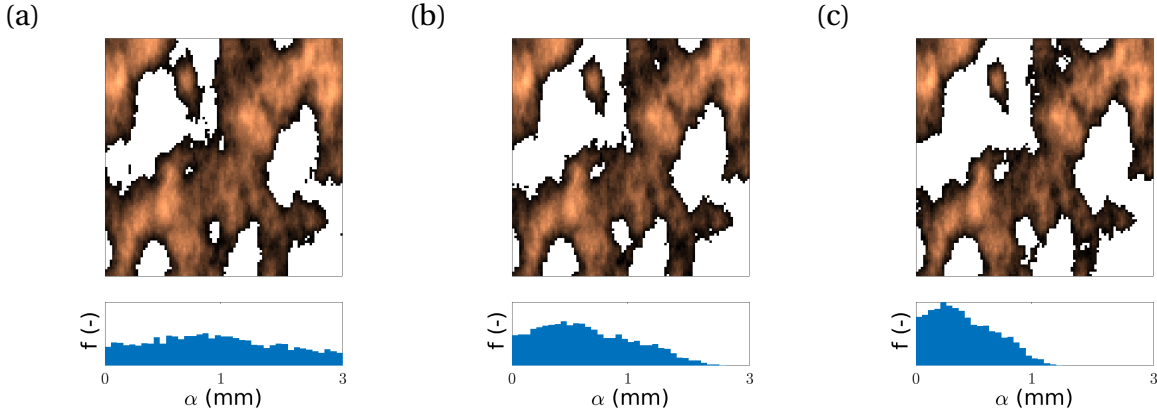
Figure 1.6 – Two self-affine 2D fields are created using the algorithm described in sec. 1.4.1, consisting of 100 × 100 cells, with a Hurst exponent $H = 0.8$ and correlation length of $l_c = 25$ cells in both horizontal dimensions. Three separations are applied between the fields which correspond to mean apertures of (a) 1 mm, (b) 0.5 mm and (c) 0.25 mm, and the resulting field corresponds to the fracture aperture field. Any intersecting cells are set to zero (contact regions and are made transparent in the figure, whereas larger apertures are shown in lighter color than smaller apertures. Note that there is no physical premise linking the mean aperture and contact regions in the creation of these aperture fields. Below each aperture field, the corresponding aperture distribution is shown.

Fracture size, orientation and position

The other geometrical properties of interest are the position, size and orientation of the fracture. We assume rectangular fractures with a variable length and width. Given the midpoint (center of the rectangle) of the fracture, we define the orientation using two angles: the dip and the azimuth. The dip (θ) corresponds to the declination from the vertical ($\hat{z} - \hat{y}$) plane and the azimuth, or dip direction, (ϕ) corresponds to rotations along the horizontal ($\hat{x} - \hat{y}$) plane. For example, a fracture with $\theta = 0°$ and $\phi = 0°$ is oriented along the vertical plane $|y| = |z|$, with $x = 0$. Increasing the dip to $\theta = 90°$ will orient the fracture along horizontal the $|x| = |y|$ plane with $z = 0$. If instead the azimuth is increased to $\phi = 90°$, the fracture will be oriented along the vertical $|x| = |z|$ plane with $y = 0$.

1.4.2. Ground penetrating radar

The analysis of EM wave propagation and scattering begins with the Maxwell equations (e.g., Jackson and Fox, 1999):

$$(a)\ \nabla \cdot \mathbf{E} = \frac{\psi}{\varepsilon_0}, \qquad (b)\ \nabla \cdot \mathbf{B} = 0,$$

$$(c)\ \nabla \times \mathbf{E} = -\frac{\partial \mathbf{B}}{\partial t}, \qquad (d)\ \nabla \times \mathbf{B} = \mu_0 \varepsilon_0 \frac{\partial \mathbf{E}}{\partial t} + \mu_0 \sigma \mathbf{E}, \qquad (1.2)$$

where $\mathbf{E}$ is the electric field ($V \cdot m^{-1}$), $\mathbf{B}$ is the magnetic field ($N \cdot A^{-1} \cdot m^{-1}$), ε is the electric permittivity ($F \cdot m^{-1}$), μ is the magnetic permeability ($N \cdot A^{-2}$), σ is the electric conductivity ($S \cdot m^{-1}$) and ψ is the electric charge density ($C \cdot m^{-3}$).

In the macroscopic treatment of Eqns. 1.2(a-d) the following constitutive relations are invoked: $\mathbf{D} = \varepsilon_0 \varepsilon_r \mathbf{E}$, $\mathbf{J} = \sigma \mathbf{E}$ and $\mathbf{B} = \mu_0 \mu_r \mathbf{H}$. These describe the interaction of EM fields with matter (e.g., Nabighian, 1991). The electric displacement field $\mathbf{D}$ ($C \cdot m^{-2}$) replaces the electric field within a dielectric material of relative electric permittivity $\varepsilon_r = \frac{\varepsilon}{\varepsilon_0}$ and the electric current density $\mathbf{J}$ ($A \cdot m^{-2}$) replaces the electric field within a conductive material of electric conductivity σ ($S \cdot m^{-1}$). The magnetic field strength is related to the magnetic flux $\mathbf{B}$ ($N \cdot m^{-1} \cdot A^{-1}$) by the relative magnetic permeability $\mu_r = \frac{\mu}{\mu_0}$. The constant values for the electric permittivity and magnetic permeability of free space are $\varepsilon_0 \equiv 8.854... \times 10^{-12} \, F \cdot m^{-1}$ and $\mu_0 \equiv 4\pi^{-7} \, N \cdot A^{-2}$ respectively. The former is defined by the latter in combination with the exact definition of the speed of light in vacuum, $c \equiv \frac{1}{\sqrt{\varepsilon_0 \mu_0}} \equiv 299\,792\,458 \, m \cdot s^{-1}$.

Stated in this manner, the constitutive relations are understood as homogenized spatial averages (Russakoff, 1970). A more intuitive and fundamental way of describing EM interaction and scattering with matter is the microscopic approach (e.g., Purcell, 2011, Ch. 11). The microscopic approach treats matter as discontinuous and composed of elements that are polarized from the incoming field and oscillate as dipoles at first approximation. The propagation of EM fields through electric and magnetic media is thus seen as the interaction of the vacuum fields with dipoles. Once polarized, the dipoles radiate a secondary field. The interference of the secondary (retarded) field with the primary (vacuum) field exactly reduces to the macroscopic fields $\mathbf{D}$ and $\mathbf{B}$. This approach of modeling EM interaction and scattering from very irregular objects was first proposed in the astrophysics community (Purcell and Pennypacker, 1973). A very informative overview of its use in astrophysics can be found in Yurkin and Hoekstra (2007) and a detailed description of the derivation and implementation of the approach in Kahnert (2003).

We recently adopted the microscopic approach with a further modification in order to model EM wave interaction and reflection from fractures with heterogeneous properties (Shakas and Linde, 2015, 2017). Our approach, that we call effective-dipoles, is described in detail in Chapter 2 and further expanded in Chapter 3. Using the effective-dipoles methodology, the fracture is discretized into dipole elements that correspond to parallel plates with varying aperture and electrical properties. The rock matrix is treated as homogeneous and we use analytic solutions for EM propagation within the rock and its interaction with each parallel plate. The formulation does not suffer from discretization errors due to numerical dispersion and discretization in Cartesian space, as do most classical numerical methods such as Finite-Difference Time-Domain (FDTD) formulations (Taflove and Hagness, 2005). Furthermore, is does not apply any boundaries in the domain and therefore does not introduce any artificial boundary reflections. When compared to FDTD schemes, the effective-dipoles approach is several orders of magnitude faster (Shakas and Linde, 2015).

Alternatively to numerical models, the thin-bed model can be used to simulate the reflected and transmitted GPR field from fractured media (e.g., Bradford and Deeds, 2006; Tsoflias and Hoch, 2006; Deparis and Garambois, 2008; Tsoflias and Becker, 2008; Sassen and Everett, 2009). The thin-bed model is analytically derived from the Maxwell equations and assumes
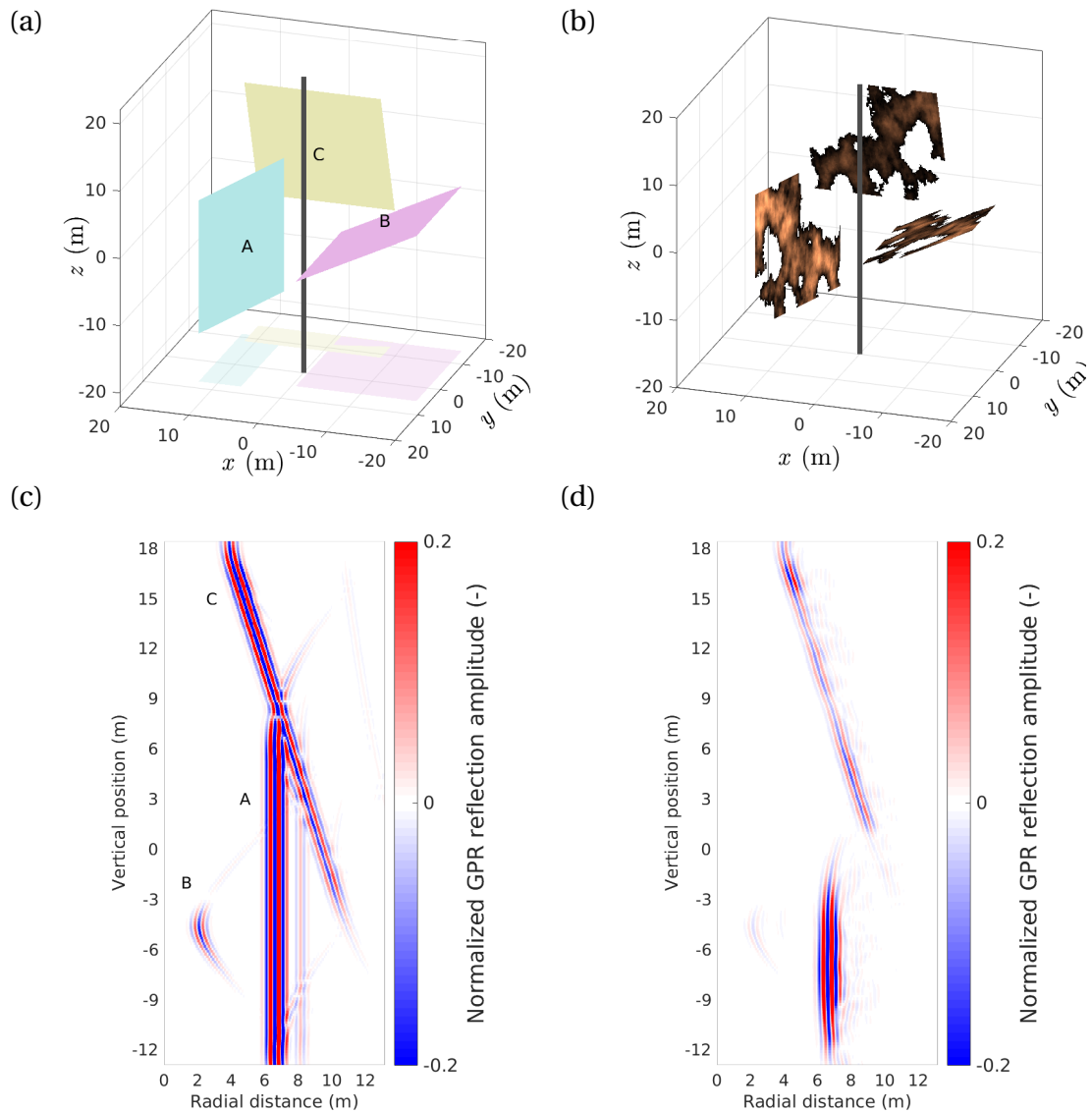
Figure 1.7 – Simulations showing the GPR reflections (c,d) from three fractures with homogeneous (a) and heterogeneous (b) aperture distributions (contact regions are transparent). For perspective purposes, the horizontal projection of each fracture is shown in (a). The fractures in (a) have the same position, orientation and mean aperture as in (b). The fracture aperture distributions in (b) are the same as the ones in Fig. 1.6, with fractures A, B and C corresponding to 1.6(a), 1.6(b) and 1.6(c) respectively. GPR reflections in (c) and (d) are computed using the methodology from Shakas and Linde (2015) at 5 cm intervals and are normalized to the maximum amplitude from (c). The color scale in (c) and (d) is adjusted to highlight the reflections from the upper fracture in (d) that are otherwise faintly visible.

that (1) fractures are homogeneous layers of infinite extent and (2) that the incoming GPR signal strikes a fracture at constant phase and amplitude. In Chapter 3 we show that even if the latter assumption is numerically valid, small scale aperture heterogeneities render the thin-bed model incapable of providing a good estimate of the mean fracture aperture.

In Fig. 1.7 we show simulated GPR reflection data from two domains; one where fractures have a homogeneous (constant) aperture and another where fractures are constituted by a heterogeneous aperture field with the same mean aperture as the homogeneous case. The reflections are computed with the effective-dipoles model using a vertically-oriented 100 MHz dipole source with a 1 m source-receiver separation. All fractures have constant electrical properties with $\varepsilon_r = 81$ and $\sigma = 0.1\ \mathrm{S \cdot m^{-1}}$. The rock medium electrical properties are $\varepsilon_r = 81$ and $\sigma = 0.001\ \mathrm{S \cdot m^{-1}}$. This electrical properties are close to realistic values for water filled fracture in granitic rock. The labels A, B and C in Fig. 1.7(a) and Fig. 1.7(c) provide a link between the fractures and their corresponding reflections. In general, the homogeneous case is characterized by coherent reflections while the heterogeneous case results in reflections that are more irregular and scattered. In both cases, fracture B gives a weak reflection because it of its sub-horizontal orientation (Olsson et al., 1992).

1.4.3. Flow and transport modeling

In the following we give the necessary equations to describe viscous, incompressible laminar flow within a parallel plate. The equations are stated and not derived but a thorough derivation is available in several of the references found in the bibliography, such as Lee and Farmer (1993); Zimmerman and Bodvarsson (1996); Zimmerman and Yeo (2000); Brush and Thomson (2003). Furthermore, extensions to the parallel plate model that account for more complicated geometries can be found in Oron and Berkowitz (1998); Lee et al. (2014); Wang et al. (2015). Additionally, we state the equations for describing solute transport through the advection-dispersion model. A derivation of the latter can be found in Cacas et al. (1990); Berkowitz (2002); Bodin et al. (2003); Faybishenko et al. (2005); Künze and Lunati (2012b).

Fluid flow through parallel plates

From a mathematical viewpoint, fluid flow is addressed by the Navier-Stokes equations that simplify, for a single-phase, incompressible fluid at steady state, to

$$\rho(\mathbf{u} \cdot \nabla)\mathbf{u} = -\nabla P + \mu \nabla^2 \mathbf{u}, \tag{1.3}$$

where $\mathbf{u}$ is the vector of fluid velocity, ∇P is the reduced pressure ($P = p - \rho g \zeta$, with pressure p and gravitational acceleration g in the direction ζ) and μ is the dynamic viscosity (e.g., Zimmerman and Yeo, 2000). Mass conservation is implied by fluid incompressibility, namely,

$$\frac{\partial \rho}{\partial t} + \nabla \cdot (\rho \mathbf{u}) = 0 \quad \rightarrow \quad \nabla \mathbf{u} = 0 \quad \forall \quad \rho = constant, \tag{1.4}$$

and if advective acceleration forces $\left(\rho(\mathbf{u} \cdot \nabla)\mathbf{u}\right)$ are small compared to viscous forces ($\mu \nabla^2 \mathbf{u}$), Eq. 1.3 can be reduced to the Stokes equations,

$$\nabla P = \mu \nabla^2 \mathbf{u}. \tag{1.5}$$

The Stokes equations (Eq. 1.5) correspond to three equations, one for each dimension in space, that link the pressure gradient to the mean flow rate.

Exact solutions for the Stokes equations are obtained by assuming laminar flow between parallel plates and applying no-flow and no-slip boundary conditions (Lee and Farmer, 1993; Zimmerman and Yeo, 2000; Brush and Thomson, 2003). The solution gives the velocity profile of a fluid under a constant pressure gradient ∇P along the direction perpendicular to the plates. For plates oriented along $\hat{x} - \hat{y}$ and aperture a_{pp} along the $\hat{z}$ direction, the velocity profile,

$$u(z) = \frac{|\nabla P|}{2\mu}\left(z^2 - \left(\frac{a_{\mathrm{pp}}}{2}\right)^2\right), \tag{1.6}$$

has the familiar parabolic form with the maximum velocity in the middle of the two plates. Integrating Eq. 1.6 along the $\hat{z}$ direction and multiplying by the width (w_{pp})of the plate gives the volumetric flux through the parallel plates,

$$Q = \frac{-|\nabla P| w_{\mathrm{pp}} a_{\mathrm{pp}}^3}{12\mu} \equiv \frac{-kA|\nabla P|}{\mu}. \tag{1.7}$$

To the right side of Eq.1.7 is the equivalent volumetric flow derived from Darcy's Law. Darcy's law in 1D states that the horizontal flow of a liquid with dynamic viscosity μ, through a porous medium with permeability k and cross sectional area A, is directly proportional to the pressure gradient $|\nabla P|$. The applicability of Darcy's law to the parallel plate model allows for the analogy between permeability and aperture. Namely, by replacing the area in Eq. 1.7 with $A = w_{\mathrm{pp}} a_{\mathrm{pp}}$ we get the relation $k = \frac{a_{\mathrm{pp}}^2}{12}$. Moreover, the product of permeability and area gives the well known "cubic law" relation:

$$kA = \frac{w_{\mathrm{pp}} a_{\mathrm{pp}}^3}{12}. \tag{1.8}$$

An analogous result to Eq. 1.8 can be obtained by solving the Reynolds equation from lubrication theory (Brown, 1987). Both approaches assume that (1) flow is laminar and (2) that the pressure gradient is uniform along the flow direction. Oron and Berkowitz (1998) use dimensional analysis of the Navier-Stokes equations to derive the conditions for which a rough aperture channel can be adequately approximated as a smooth parallel-plate. The authors conclude with the following three conditions (refer to Fig. 1.5b):

$$\frac{\sigma_{\mathrm{pp}}^{\{u,d\}}}{a_{\mathrm{pp}}} << 1, \quad \left(\frac{a_{\mathrm{pp}}}{2L_{\mathrm{pp}}}\right)^2 << 1, \quad \text{and} \quad Re \cdot \max\left(\frac{\sigma}{a_{\mathrm{pp}}}, \frac{a_{\mathrm{pp}}}{2L_{\mathrm{pp}}}\right) << 1. \tag{1.9}$$

The third condition in 1.9 introduces the Reynolds number, defined as $Re \cong \frac{\rho U a_{\mathrm{pp}}}{2\mu}$ where $U[\frac{\mathrm{m}}{\mathrm{s}}]$ is the characteristic velocity of the fluid flowing through the parallel plate.

A clarification must be made about the use of the cubic law (Eq. 1.8) in this thesis. There exists a vast amount of theoretical and experimental studies that examine the applicability of

the cubic law (e.g., Witherspoon et al., 1980; Brown, 1987; Pyrak-Nolte et al., 1988; Ge, 1997; Zimmerman and Yeo, 2000) in predicting flow through a fracture with rough walls. Initially, the cubic law was applied to the whole fracture in order to compute one equivalent aperture (Tsang, 1992). This approach has been gradually replaced by the point-to-point application of the cubic law, often termed as the "local cubic law" (LCL) (e.g., Oron and Berkowitz, 1998; Brush and Thomson, 2003; Konzuk and Kueper, 2004; Qian et al., 2011; Lee et al., 2014; Wang et al., 2015). In this thesis, we use the LCL model that allows us to directly link the fracture discretization used for flow and transport to the one used for modeling GPR reflections.

Solute transport

Transport of a solute through a rough fracture has also received considerable attention (e.g., Tang et al., 1981; Novakowski et al., 1985; Moreno et al., 1990; Nordqvist et al., 1992; Bodin et al., 2003). Once the fluid velocity has been determined along each parallel plate cell in the fracture plane, it can be used to compute the transport of a solute through the advection-diffusion equation (given for an incompressible fluid and $\nabla \cdot \mathbf{u} = 0$):

$$\frac{\partial}{\partial t}(c) + \nabla \cdot [c\mathbf{u} - D_{\mathrm{m}}\nabla c] = 0. \tag{1.10}$$

The concentration of the solute in Eq. 1.10 is denoted by c that can either have units (e.g., $\mathrm{kg \cdot m^{-3}}$) or represent a unit-less concentration by normalizing it with the maximum concentration. The fluid velocity is given by $\mathbf{u}$ in $[\mathrm{m \cdot s^{-1}}]$, D_{m} is the molecular diffusion coefficient of the solute in $[\mathrm{m^2 \cdot s^{-1}}]$. This formulation does not account for any interaction of the solute with the rock matrix.

Tracer flow and transport in MaFloT-2D

For modeling flow and transport of a tracer in a single fracture we modified an existing forward code (MaFloT-2D) that was developed by Künze and Lunati (2012b). MaFloT-2D is based on a Finite Volume algorithm and simulates density-driven flow, hydrodynamic dispersion, diffusion and advection in a 2D cross section of a porous medium by assigning the porosity (ratio of void volume to total volume) and permeability of each cell in the 2D section. The mass balance equation for a single incompressible fluid completely saturating a porous matrix is then solved to obtain the pressure distribution. Using the pressure solution, the Darcy velocity of the fluid within the plane is computed and used for transport. By discretizing the advection-diffusion equation in both time and space, the concentration at each time step is computed. More information about MaFloT-2D can be found in *www.maflot.com*.

Our modifications to MaFloT-2D are the following:

1. Assign the permeability of each cell using the permeability-aperture relation, $k = \frac{a^2}{12}$.
2. Assign the porosity of each cell (ϕ_c) as the void space between the parallel plates, $\phi_c = a \times L_c^2$, where L_c is the side-length of each cell (cells are square).
3. Scale diffusion to occur across the minimum cell interface area; MaFloT-2D originally simulates porous media, thus allowing the porosity between cells to change while the interface area remains the same. On the contrary, when fracture aperture changes

(a)   (b)   (c)
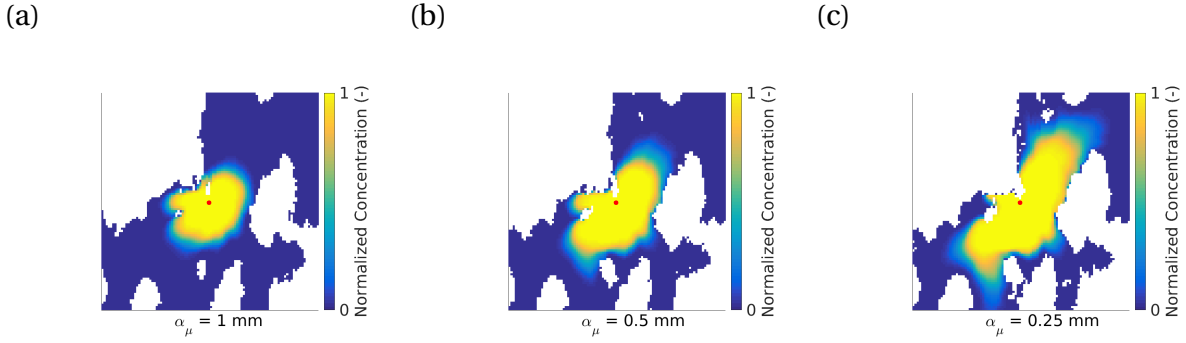
Figure 1.8 – Simulation of a tracer experiment using the modified version of MaFloT-2D (Künze and Lunati, 2012b). The simulation is computed for the fractures shown in Fig. 1.6, namely, (a) corresponds to Fig. 1.6a, (b) to 1.6b and (c) to 1.6c. Each figure shows the (normalized) distribution of the tracer after a 50 L injection in the middle of the domain (indicated by a red dot). Only the parallel plates that percolate with the injection location are used and the spatial dimensions of the domain are set to 20 × 20 m.

       along the plane, we take the minimum area between two cells to compute diffusion and dispersion.

4. Introduce contact cells (zero aperture) as no-flow zones.

Furthermore, we assign Dirichlet (zero-pressure) boundary conditions at the outer boundaries of fractures, thus allowing for pressure changes to equalize during the simulation of a tracer injection. Nevertheless, we create large enough fractures so that the tracer remains within the fracture volume during the simulation. To simulate the injection and withdrawal of a tracer during a push-pull test, we assign dynamic inflow and outflow boundary conditions at the injection location. Tailing in the breakthrough curve is possible through the heterogeneity of the aperture field (e.g., Fiori and Becker, 2015).

1.4.4. Simultaneous modeling

Here, we introduce the simultaneous model with an example where we simulate the injection and chasing of an electrically conductive tracer and the resulting GPR reflections. This particular model is chosen because it described the type of experiments that we present in sec. 1.5.2. The GPR reflections are computed in a time-lapse manner and are thus affected by the dynamic distribution of tracer in the fracture. The responses of both models are affected by the fracture's geometrical properties.

On the left column of Fig. 1.9 we show the distribution of tracer in fracture A of Fig. 1.7(b), at the onset of injection, end of injection and end of chasing phases of a push-pull test. On the right column we show the corresponding GPR reflection data that is computed taking into account the dynamic redistribution of tracer during the GPR monitoring along a borehole (e.g., 1.5.2. For this example we use the following parameters:
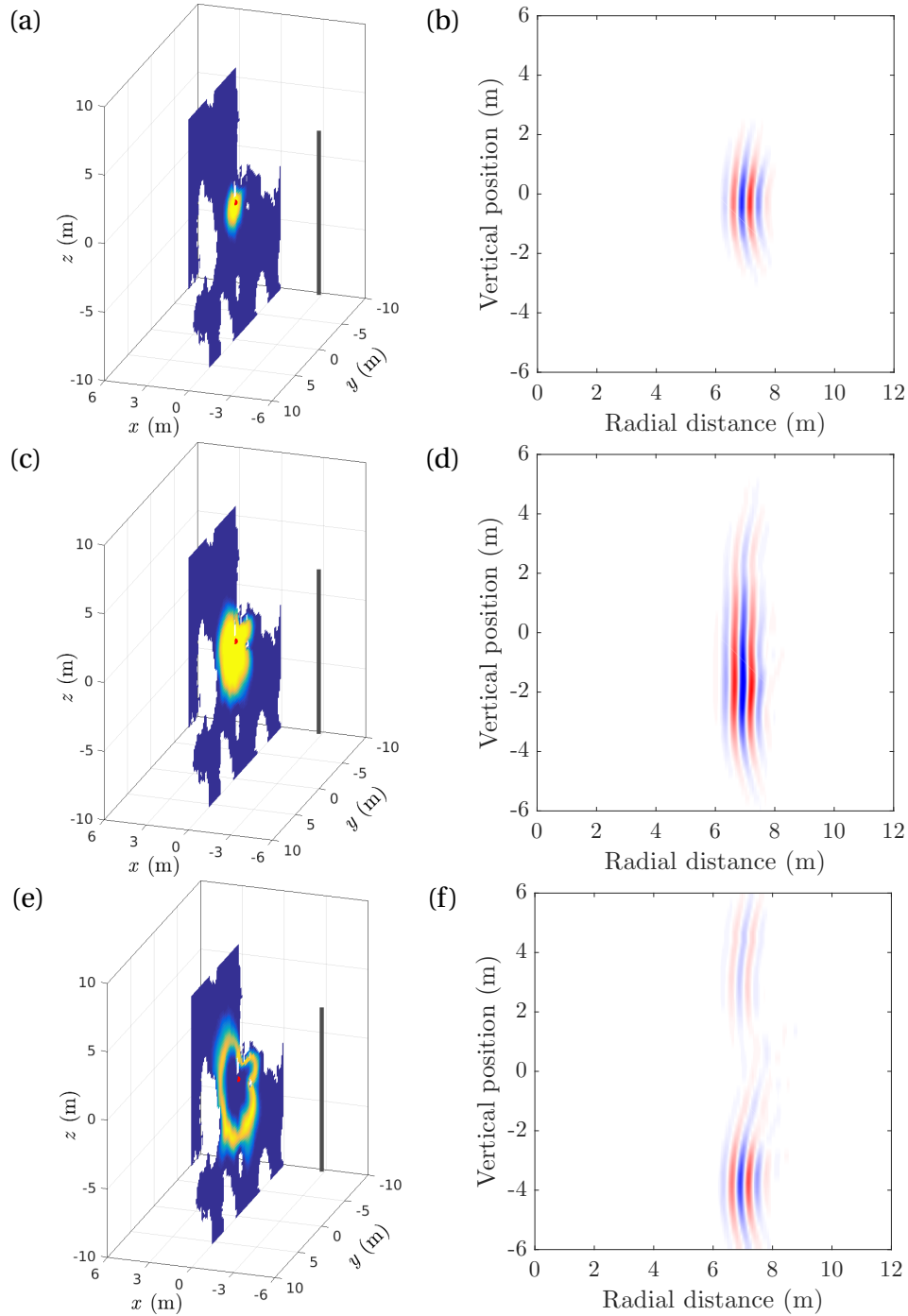
Figure 1.9 – A simultaneous simulation. (a) and (c) show the onset and end of a tracer injection and (e) shows the end of the chasing period. The color scale indicates regions of maximum (yellow) and no (blue) tracer. GPR reflection (difference) data are computed along the (solid black) vertical line in (a), (c), (e) and plotted in (b), (d), (f) respectively. The color scale indicates maximum positive (red) and maximum negative (blue) amplitudes of the vertical electric field. More detail can be found in sec. 1.4.4.

1. Tracer: V = 50 L, μ = 2 mPa·s, ρ = 10^3 kg·m^{-3}, σ = 35 mS·cm^{-1}, ε_r = 81.
2. Chaser: V = 50 L, μ = 1 mPa·s, ρ = 10^3 kg·m^{-3}, σ = 0.7 mS·cm^{-1}, ε_r = 81.

3. Pumping rate = $3\,\mathrm{L\cdot min^{-1}}$.
4. GPR dominant frequency: 100 MHz.
5. Antenna separation: 1 m.
6. Rock matrix: $\sigma = 10^{-3}\,\mathrm{mS\cdot cm^{-1}}$, $\varepsilon_r = 9$.

The tracer concentration can be converted to electrical conductivity, and vice versa using the relation proposed by Sen and Goode (1992). For molecular diffusion we apply the coefficient $D_\mathrm{m} = 2\cdot 10^{-9}\,\mathrm{m^2\cdot s^{-1}}$ in Eq. 1.10. The properties of the background fluid and the chasing fluid are identical.

1.5. Experiments

All experiments presented in this thesis took place at the Stang-er-Brune test site, just outside the town of Ploemeur in Brittany, France. Ploemeur is a town of 20,000 inhabitants that is located nearby an aquifer composed of fractured crystalline granite (Ruelleu et al., 2010). The aquifer is monitored by a dense network of $\sim$ 50 boreholes, ranging from 30 to 150 m in depth (French National Observatory, H$^+$, hplus.ore.fr/en). In this section, single-hole and single-well refer to experiments performed in one borehole while cross-hole and multiple-well refer to experiments performed in two or several boreholes. We only present experiments that were performed in a single borehole, that is, one borehole for the push-pull test and one borehole for the GPR monitoring. The experiments are discussed in more detail in Chapters 4 and 5.

Previous hydrologic tests on this site include single-hole and cross-hole flow meter experiments and hydraulic pumping tests (Le Borgne et al., 2004, 2006, 2007), thermal sensing experiments (Read et al., 2013; Klepikova et al., 2014; Read et al., 2014), atmospheric tracer tests (Marçais et al., 2015), and several convergent and push-pull tracer tests (Boisson et al., 2013; Kang et al., 2015). Geophysical techniques used include gravity measurements (Boy et al., 2009), seismic experiments (Pasquet et al., 2015) and single-hole and cross-hole GPR (Dorn et al., 2012). Hydrogeophysical monitoring experiments include single-hole GPR imaging of convergent tracer tests (Dorn et al., 2011, 2012) and single-hole monitoring of push-pull tests (Shakas et al., 2016, 2017). The combined single-hole GPR and push-pull experiments are discussed in more detail in chapters 4 and 5. Here, we introduce the methodology and discuss some aspects of our combined experiments.

1.5.1. Push-pull tracer tests

Push-pull tracer tests, also called single-well injection-withdrawal tests, involve the subsequent injection and extraction of a tracer in an isolated interval of one borehole well. An area of interest, for example an interval of the well intersected by an open fracture, is isolated with a double packer within which injection (push) and extraction (pull) takes place. The injection of the tracer can be followed by a chasing period, during which ambient water is injected to effectively clean the borehole interval and push the tracer further out into the formation.

In the extraction phase the pump is reversed and the concentration of inflowing tracer is measured over time to give the BTC. A detailed explanation of push-pull tests can be found in Istok (2012) or Neretnieks (2007).

Push-pull tests require one borehole and are often preferred from multiple-well tests because of their reduced cost and logistics. Nevertheless, the main advantage of push-pull is that the flow-reversal introduced during the pulling period minimizes the effect of heterogeneous advection on the tracer BTC. Heterogeneous advection is the separation of the tracer into different flow channels within a single fracture or a fracture network that occurs due to the strong disparity in aperture (e.g., Fiori and Becker, 2015). In a convergent tracer test the tracer is injected in one location and recovered in another so heterogeneous advection may introduce skewness in the BTC. In an ideal push-pull test the tracer is assumed to travel through the same pathways during the injection and withdrawal phases, so the effect of heterogeneous advection is often assumed negligible. If flow reversibility can be assumed, time irreversible processes such as diffusion will have a stronger effect on the BTC shape (more on this in sec. 1.5.1). An additional waiting period between pushing and pulling can help study irreversible processes (Istok, 2012; Neretnieks, 2007).

The main weakness of push-pull tests is that they provide data at only one spatial location and do not give any insight on the tracer flow field or the spatial heterogeneity of the system (e.g., Lessoff and Konikow, 1997). In fact, BTC's from a push-pull test are completely uninformative of the spatial extent of the tracer test (Hansen et al., 2016). A schematic of the measured tracer concentration as a function of an ideal push-pull test is shown in Fig. 1.10. In theory, the total initial mass of tracer is recovered in the BTC during a push-pull test. In the absence of other irreversible processes only molecular diffusion acts to change the shape of the injected tracer pulse.

Factors affecting the push-pull BTC

As indicated in Fig. 1.10, the ideal push-pull test will result in a slightly positively skewed BTC since later arrivals are subject to longer time for molecular diffusion. Molecular diffusion is a microscopic process that happens spontaneously, in which particles within a fluid move from regions of high concentration to regions of lower concentration. There exist several factors that cause deviations in measured data from the ideal push-pull BTC (Istok, 2012; Neretnieks, 2007; Hansen et al., 2016). Here, we only state the different flow related processes without a detailed theoretical analysis of each one. The effect of gravity-induced flow is discussed in chapters 4 and 5. Chemical processes such as adsorption of reactive transport are not discussed.

1. **Natural hydraulic gradient:** The existence of natural flow at a push-pull test site will introduce ambiguity in the BTC since the two flow phases will not have an equal effect on the tracer. One method of assessing the strength of natural flow on the BTC is to perform several tests with different waiting times, in conjunction with geophysical monitoring (e.g., Shakas et al., 2016, 2017).
2. **Matrix diffusion:** The flow of tracer into the rock matrix is called matrix diffusion (e.g., Lessoff and Konikow, 1997). Matrix diffusion will cause a slow down in the migration of tracer and a decrease in the peak of the BTC. Diffusion rates will vary depending on the
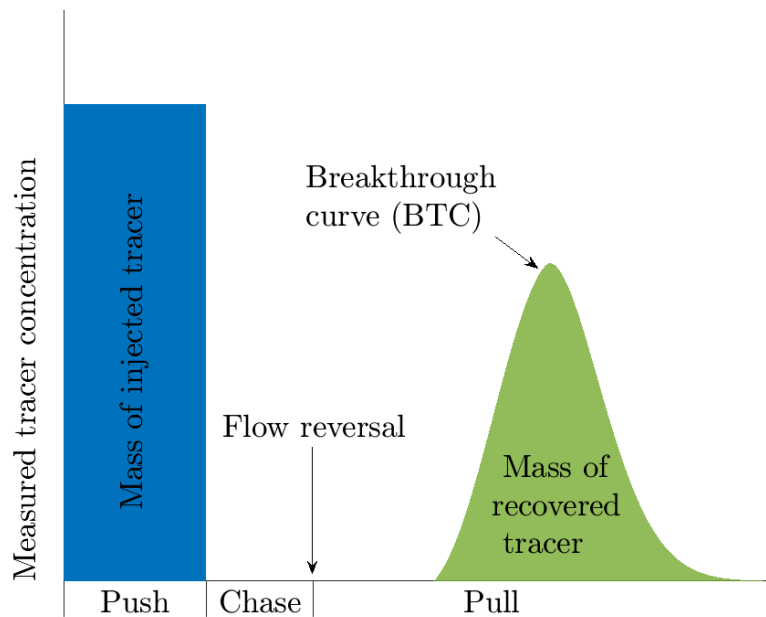
Figure 1.10 – Schematic of the measured tracer concentration vs. experiment time in an ideal push-pull test. Tracer injection is followed by a chasing period in which ambient water is injected to clear out the packed interval and push the tracer further into the formation. The flow is reversed during the withdrawal period and the measured tracer concentration in the packed interval constitutes the breakthrough curve (BTC). An additional waiting time can be introduced between chasing and flow reversal. The ideal BTC is only (slightly) positively skewed because of molecular diffusion. Note that no time units are displayed as the time scale of such experiments can vary from minuted to days. For the experiments presented in this thesis, the pushing and chasing period were approximately 30 min each and the pulling period was several hours (overnight).

    type of tracer used and on the permeability of the rock matrix. In many cases this effect can be deemed negligible (e.g., Becker and Shapiro, 2000, 2003).

3. **Dispersion-enhanced mixing:** The heterogeneous velocity field that results from aperture differences within a fracture will lead to local mixing of the tracer, that is termed hydrodynamic dispersion. Local mixing may occur for a variety of reasons including contact of the tracer with water that is in dead-end fractures, or Taylor dispersion caused from shear flow within the fracture (Novakowski et al., 1985).

In addition to the factors listed above, estimating the mean aperture of a fracture from push-pull tracer tests poses additional problems. Namely, Tsang (1992) discusses three equivalent aperture estimates that can be derived from hydraulic and tracer tests by assuming different geometries and flow processes:

1. **The mass balance aperture:** The area of the fracture is assumed known and the volumetric flow rate along with the mean residence time are used to compute an equivalent aperture.
2. **The frictional loss aperture:** A transport velocity is derived from pressure drop hydraulic measurements and Darcy's law is applied for a parallel plate fracture. The flow path length and the mean residence time of the tracer are then used to compute an equivalent aperture.
3. **The cubic law aperture:** Darcy flow is assumed between two parallel plates and pressure drop measurements, flow rates and fracture geometry are used to compute an equivalent aperture.

Tracers in hydrogeophysics

The design of a push-pull tracer test involves the choice of (1) tracer type, volume and concentration, (2) flow rate during the injection, chasing and withdrawal, (3) volume of chaser and an (4) optional waiting time. In order to monitor a tracer test with a geophysical method the tracer must have a measurable 'geophysical' signature. Geophysical techniques used for this purpose are electric or EM methods and the contrast in properties imposed by the tracer is typically a change in the electrical conductivity.

The most common method of creating an electrically conductive tracer is to add salt, usually table salt (NaCl), to freshwater (e.g., Day-Lewis et al., 2003; Kemna et al., 2002; Singha and Gorelick, 2005; Tsoflias and Becker, 2008; Dorn et al., 2011; Doetsch et al., 2012; Rosas-Carbajal et al., 2015; Shakas et al., 2016). Saline tracers are easy to prepare and handle and allow for continuous (and low cost) monitoring through electrical conductivity probes. However, high salt concentrations are often necessary to obtain a saline tracer that is detectable by geophysical techniques. This poses the potential problem of polluting a freshwater aquifer and at the same time introduces a strong density contrast of the saline tracer compared to the background water.

The density of a saline tracer, even when at low concentrations (e.g., Istok and Humphrey, 1995; Beinhorn et al., 2005; Kemna et al., 2002), poses a considerable concern for the reversibility of a push-pull test. Very few hydrogeophysical studies have addressed the density effect (e.g., Doetsch et al., 2012; Shakas et al., 2016; Haaken et al., 2017; Shakas et al., 2017), and when doing so have shown that density driven flow was not negligible. In Chapter 5 we introduce a new tracer that we call wethanalt. Wethanalt is a mixture of saline water and ethanol and allows us to create a neutrally-buoyant and electrically conductive tracer. We compare push-pull experiments with the neutrally-buoyant tracer to previous experiments with a saline tracer (presented in Chapter 4) and show that much higher salt mass is recovered in the former case, and the shape of the BTC is very different. These findings are also supported by single-hole GPR reflection images, that also give an insight to natural flow in the system when the neutrally-buoyant tracer is used.

Even though wethanalt is a promising tracer for use in hydrogeophysics, it will result in a tracer that is more viscous than water. Fig. 1.11 shows the change in density and dynamic viscosity of ethanol-water mixtures at different concentrations (plotted from tabulated data in (Hammond, 2016)). The two fluids are fully miscible and the density decreases almost linearly
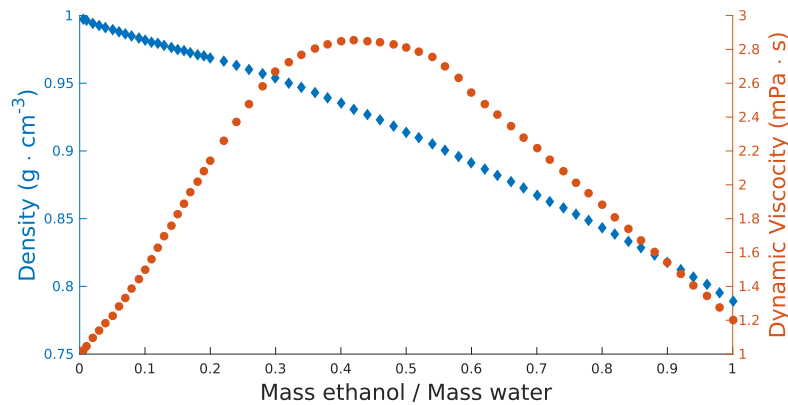
Figure 1.11 – Laboratory measurements of the density (blue diamond marker) and dynamic viscosity (red circle marker) of ethanol-water mixtures, reproduced from tabulated data in Hammond (2016). The density follows a relatively linear trend with slight changes in slope. The viscosity profile is non-linear and reaches a maximum at an ethanol percentage of ~ 45%. The two fluids are fully miscible.

when ethanol is mixed with water. The dynamic viscosity changes non-linearly and reaches a maximum value at an ethanol percentage of ~ 45%, but can be assumed approximately linear from 0% to ~ 30% of ethanol. The latter range is perhaps the most useful for wethanalt tracers. Experimental studies and theoretical arguments support that when a less viscous (μ_1) fluid displaces a more viscous (μ_2) fluid, mixing instabilities evolve at the fluid interface that gradually stabilize through molecular diffusion. Chui et al. (2015) present instabilities for a viscosity ratio of 10, i.e., a fluid with low viscosity displacing a fluid that is 10 times more viscous. By performing experiments in the viscosity ratio range of 1 to 25, they conclude that molecular diffusion stabilizes the process with time as $t\,\frac{\mu_2}{\mu_1}$. Nevertheless, the crossover time between unstable and stable displacement also depends on the flow rate of the displacing fluid; that is, faster flow rates induce faster stability. When designing a wethanalt tracer experiment, even though the viscosity ratios are bound to be small (maximum ~ 2.84) care must be taken to avoid instabilities. This can be achieved by adjusting the injection, chasing and withdrawal flow rates accordingly (see Chui et al. (2015) for more details) but for the viscosity ratio used in the experiments presented here, fingering instabilities have not been observed in the laboratory experiment.

1.5.2. Ground penetrating radar imaging

GPR is a high-resolution, non-destructive imaging technique used for various geophysical applications ranging from mapping fractures in the subsurface (e.g., Olsson et al., 1992; Grasmueck, 1996; Jeannin et al., 2006) to mapping fractures in marble blocks (e.g., Sambuelli and Calzoni, 2010; Patriarca et al., 2011), hydrocarbon detection in fractured rock (e.g., Lane et al., 2000; Babcock and Bradford, 2015) and hydrogeophysical imaging of tracer flow (Tsoflias et al., 2001; Tsoflias and Becker, 2008; Dorn et al., 2011; Tsoflias et al., 2015; Shakas et al., 2016, 2017). A recent overview of GPR developments is given by Slob et al. (2010).

Figure 1.12 – (a) Image of the 100 MHz MALÅ GPR receiver and transmitter antennas used for data acquisition, fitted with custom-made centralizers (white). (b) Image of the transmitter antenna in the GPR monitoring borehole that was fitted with a flexible liner (yellow).

GPR is based on transmitting and receiving high-frequency EM waves that are scattered from discontinuities in the electrical properties of matter. One of the basic principles of GPR is that EM waves are propagating. This implies that the propagating medium must be a low-loss dielectric and as a rule of thumb, less electrically conductive media will allow for larger investigation volumes. At the same time, discontinuities in electrical properties must be strong enough (usually more electrically conductive) compared to the background medium in order to be detectable.

The spatial scale of GPR investigations is also determined by the choice of antenna operating frequency that typically ranges between 10 - 1000 MHz (Jol, 2008). A GPR antenna creates a pulse of waves that propagate at several frequencies, but is usually centered around a dominant frequency. The dominant frequency is partly determined by the antenna manufacturer characteristics, such as the electrical circuit components and size, but also by the surrounding medium in the antenna's vicinity (e.g., Ernst et al., 2006).

Single-hole time-lapse monitoring

For all the experiments we used a MALÅ slim-hole antenna system with a dominant frequency of 100 MHz (Fig. 1.12a). The system consists of a transmitter and receiver antenna that are independently triggered and it is thus possible to perform surveys with changing transmitter-receiver separation, or with the transmitter and receiver in different boreholes (e.g., Dorn et al., 2012).

When a strong contrast in electrical conductivity exists, such as when a saline tracer is present in a fracture, most of the energy in the GPR signal is reflected rather than transmitted (e.g., Tsoflias and Becker, 2008). In this case GPR data will be more informative if collected in reflection mode, as in the single-hole setup. Nevertheless, one known ambiguity of single-hole GPR reflection data is that they lack azimuth information about the fracture locations (Olsson et al., 1992). This effect can be clearly seen in Fig. 1.7(b) where reflections from fractures around the borehole (Fig. 1.7(c)) overlap in the modeled GPR response. Azimuth ambiguity can be partly overcome when using a directional antenna (Slob et al., 2010).

To accurately detect time-lapse changes in the GPR signal, the position of the antenna system in the borehole must be the same when a measurements is repeated. To assure that the GPR system was centered along the borehole we attached custom-made flexible centralizers to the top and bottom of each antenna (Fig. 1.12a). Additionally, to (1) avoid that electrically conductive tracer entered the GPR monitoring borehole, (2) allow for smooth movement of

the antennas along the borehole and (3) minimize pressure disturbances from the moving antennas affecting the push-pull test, we installed a flexible liner (http://www.flut.com/) in the GPR borehole (see Fig. 1.12b and sec. 4.3). Once a time-lapse survey was successfully completed, we focused our analysis of GPR data on difference imaging; the subtraction of the background GPR trace obtained before the onset of the push-pull test, from later traces obtained during the push-pull test. We provide a detailed description of difference imaging and the processing steps performed on the GPR data in sections 4.4 and 5.3.4.

Dynamics of the combined experiments

Here we make a remark about the dynamics of the combined experiments described in Chapters 4 and 5: The speed at which the tracer migrates within the fractures ($v \sim 3 \times 10^{-3}\,\mathrm{m\cdot s^{-1}}$, see sec. 4.6.2) is minute compared to the speed at which EM waves propagate in granite ($v \sim 10^8\,\mathrm{m\cdot s^{-1}}$). During the acquisition of one GPR trace, the tracer distribution can be consequently assumed stationary. Furthermore, the speed at which the antennas move in the borehole during data acquisition ($v \sim 10^{-1}\,\mathrm{m\cdot s^{-1}}$), while closer in magnitude to the tracer migration speed, is still large enough to approximate each GPR section as a 'snapshot' of the experiment. Nevertheless, the coupled model takes into account the dynamics of the tracer between the computation of each trace.

1.6. Objectives

One of the primary objectives of this thesis is to establish a forward modeling framework for computing GPR propagation and scattering in heterogeneous fractured rock (Chapter 2). The forward model must take into account fracture heterogeneity and also be fast enough for being used in probabilistic inversion framework (Tarantola, 2005). Another objective is to investigate the assumption of homogeneity in fracture properties that is often made when the thin-bed model is invoked. The thin-bed model can be analytically derived from Maxwell's equations by assuming that fracture properties are homogeneous, that the fracture is of infinite extend and that the incoming GPR wave arrives as a plane wave over the whole fracture plane. These assumptions are further examined and the validity of the thin-bed model is tested in the presence of heterogeneous fracture aperture distributions (Chapter 3).

On the experimental side, the primary objective is to show that push-pull tests can be complemented with single-hole GPR time-lapse imaging to obtain quantitative information that is otherwise unavailable. In Chapter 4 GPR reflection data are shown to provide information about (1) the spatial extent of the tracer test, (2) the number and the orientation of the fractures involved, (3) the importance of density-driven flow, (4) the strength of ambient flow and even (4) estimates of the tracer velocity. Another experimental objective is to examine the possibility of using neutrally buoyant tracers that can be detected by electrical and EM geophysical methods. One such tracer is deionized water, that is electrically resistive and usually has negligible density difference to the surrounding formation water in a freshwater aquifer. In both experimental campaigns described in Chapters 4 and 5 we injected deionized water during a push-pull test (100 and 1000 L respectively) but did not obtain a strong enough

signature in the GPR reflection data. Instead, in Chapter 5 we introduce a different approach to obtain a neutrally-buoyant and electrically conductive tracer for by mixing a saline tracer with ethanol.

A final objective is to develop a simultaneous model that simulates tracer flow and transport in a single fracture and simulates the time-lapse GPR signature associated with the dynamics of the tracer experiment. The simultaneous model, presented in sec. 1.4.4, is currently used in a Markov-Chain Monte-Carlo inversion framework to statistically infer the geometrical properties of a single fracture, from both synthetic and field data. The results are not presented in this thesis.

1.7. Outline

In the next four chapters we present work that has been published in peer-reviewed journals and herein slightly modified to fit the theme of this work. Namely,

- In Chapter 2 we develop the theoretical framework for our proposed effective-dipoles model. We first validate the model with an existing numerical code and further used it reproduce (laboratory) GPR reflection data from Grégoire and Hollender (2004).
- In Chapter 3 we examine the effect of aperture heterogeneity when a fracture is assumed to have homogeneous properties - an assumption commonly made when invoking the thin-bed model. We begin by verifying the suitability of the effective-dipoles method to simulate GPR reflection data resulting from heterogeneous fractures. We then verify the applicability of the thin-bed model in inferring the true aperture from noise-contaminated synthetic data, created using the effective-dipoles method, a constant aperture fracture model and a suitable modeling domain. Finally, we investigate the aperture estimates obtained with the thin-bed model when the GPR reflection data is created from a fracture with a heterogeneous aperture distribution. The latter is assigned using a geostatistical model and noise-contaminated data are created using the effective-dipoles model.
- In Chapter 4 we present results from the first combined push-pull and GPR single-hole monitoring experiments. The experimental methodology is explained and the theory of GPR difference imaging is briefly described, as well as the processing steps applied to the GPR data. Results from push-pull tests, with and without a waiting time between the injection and withdrawal phase are analyzed. Also, results from a static GPR antenna experiment are shown and the dynamics of the BTC are compared to the corresponding GPR signal.
- In Chapter 5 we present results from the first hydrogeophysical experiment where a neutrally buoyant tracer is imaged. We propose a new type of tracer that is a combination of a saline tracer with pure ethanol, which we call wethanalt. Wethanalt is suitable for any hydrogeophysical application where electric or EM methods are used to image a tracer experiment. GPR reflection data and BTC's from the wethanalt experiments are compared to similar experiments performed with the (classical) saline tracer presented in Chapter 4 and the effect of density is assessed.

Chapter 6 concludes with a summary of this work, some remarks on current limitations and an outlook. In appendix A we provide the effective-dipoles formulation with an example in MATLAB code format.

Chapter 2

Effective modeling of ground penetrating radar in fractured media using analytic solutions for propagation, thin-bed interaction and dipolar scattering

Alexis Shakas and Niklas Linde.

2.1. Abstract

We propose a new approach to model ground penetrating radar signals that propagate through a homogeneous and isotropic medium, and are scattered at thin planar fractures of arbitrary dip, azimuth, thickness and material filling. We use analytical expressions for the Maxwell equations in a homogeneous space to describe the propagation of the signal in the rock matrix, and account for frequency-dependent dispersion and attenuation through the empirical Jonscher formulation. We discretize fractures into elements that are linearly polarized by the incoming electric field that arrives from the source to each element, locally, as a plane wave. To model the effective source wavelet we use a generalized Gamma distribution to define the antenna dipole moment. We combine microscopic and macroscopic Maxwell's equations to derive an analytic expression for the response of each element, which describe the full electric dipole radiation patterns along with effective reflection coefficients of thin layers. Our results compare favorably with finite-difference time-domain modeling in the case of constant electrical parameters of the rock-matrix and fracture filling. Compared with traditional finite-difference time-domain modeling, the proposed approach is faster and more flexible in terms of fracture orientations. A comparison with published laboratory results suggests that the modeling approach can reproduce the main characteristics of the reflected wavelet.

2.2. Introduction

Identification and characterization of permeable fractures within rock formations is a central research topic in hydrology (NRC, 1996). The flow and transport behavior in fractured media can be very complex and difficult to infer from traditional hydrological experiments (Neuman, 2005). A promising approach is to combine hydrologic measurements with ground penetrating radar (GPR) data (e.g., Olsson et al., 1992). Both surface reflection and cross-borehole tomographic monitoring studies have been used to infer the spatial distribution of tracer plumes and to dynamically image tracer transport through preferential flow paths (Birken and Versteeg, 2000; Tsoflias et al., 2001; Day-Lewis et al., 2003; Talley et al., 2005; Becker and Tsoflias, 2010; Dorn et al., 2011, 2012). Furthermore, the ability of GPR to provide information about mm-thick fractures has been demonstrated theoretically (Hollender and Tillard, 1998; Bradford and Deeds, 2006; Tsoflias and Hoch, 2006), through controlled experiments (Grégoire and Hollender, 2004; Tsoflias et al., 2004; Sambuelli and Calzoni, 2010) and by field-based investigations (Tsoflias and Hoch, 2006; Sassen and Everett, 2009; Dorn et al., 2011, 2012). In the complex environment found in most fractured rock systems, efficient and effective interpretation of GPR measurements must rely on forward models that accurately simulate the experiments.

When an electromagnetic wave impinges on a thin layer, a series of complex interference phenomena occur that alter both the phase and amplitude of the reflected and transmitted waves. Such phenomena have been studied extensively in optics and exact solutions are available by applying the macroscopic Maxwell's equations and associated boundary conditions

on the sides of a dielectric slab (e.g., a fluid filled fracture). These solutions have been used in geophysics to describe how the GPR signal reflected from fractures varies as a function of material properties, fracture thickness (aperture) and orientation (Tsoflias and Hoch, 2006; Tsoflias and Becker, 2008).

Numerical GPR forward modeling schemes do not incorporate the analytic nature of the effective reflection coefficients since space discretization and medium parameterization implicitly account for boundaries, across which the macroscopic Maxwell's equations are solved. As spatial discretization becomes finer, the macroscopic numerical solutions approach the analytically derived Fresnel reflection and transmission coefficients. However, the finite spatial discretization gives rise to errors, especially when modeling irregular geometries or fine-scale structures. Sub-discretization schemes have been recently proposed (e.g., Diamanti and Giannopoulos, 2009) but the computational demand still remains for 3D implementations. Moreover, irregular geometries still pose a problem since FDTD codes usually implement a Cartesian grid and tilted planar surfaces are not discretized exactly; a known problem that is often referred to as "staircasing". In numerical solvers based in the time domain, insufficient temporal sampling can also give rise to numerical dispersion (Bergmann et al., 1998). Ray-tracing algorithms can include effective reflection coefficients, but they rely on the plane wave assumption being valid everywhere along an interface and only consider the far-field region of electromagnetic radiation. Furthermore, ray-tracing workflows are often based on algorithms developed for seismic processing (Dorn et al., 2012) and ignore the polarized response of GPR sources and reflections.

A more general approach is to consider a fracture as a polarizable dielectric and conductive anomaly, in which many infinitesimal dipoles are induced and oscillate in response to the incident field. This approach is exactly described by the microscopic Maxwell's equations (e.g., Purcell, 2011, Ch.11), in which matter is seen as a collection of polarizable particles. The macroscopic boundary conditions can then be derived as limiting cases of the microscopic approach through the Ewald-Oseen extinction theorem (Fearn et al., 1996). The macroscopic approach is thus an averaged version of the microscopic formulation, the latter not only being correct in the quantum regime but also more intuitive (Feynman et al., 1964, Ch.10-11). A numerical modeling application of the microscopic Maxwell's equations has been used extensively by the astrophysical community to describe light scattering from dielectric objects — see Yurkin and Hoekstra (2007) for an overview — but we are not aware of applications to GPR scattering.

We propose a forward modeling approach that uses analytic solutions to simulate the propagation of electromagnetic waves within homogeneous media and the scattering of the waves from fractures. The fractures are seen as dielectric and conductive anomalies that are polarized by the incident EM field and are defined as rectangular planes with a given midpoint, azimuth, dip, thickness and material filling. Each fracture plane is discretized into polarizable elements, a formulation which enables simulating heterogeneous tracer concentrations in the fractures by varying the electrical properties of each element over time, and also accounts for the change in direction and magnitude of the incident electric field along the fracture plane. The elements are modeled as infinitesimal dipoles that are polarized linearly and in parallel to the incident electric field. The main difference from the astrophysical formulation are that we only assign effective dipoles along the plane of the

fracture. To account for the effect of the dipoles along the direction normal to the fracture plane we apply the Ewald-Oseen extinction theorem and scale the dipoles by the effective reflection coefficients of a thin layer. Another difference is that we only consider the incident field caused by the external source and do not account for interactions between elements. We use analytical expressions of the Maxwell equations in a homogeneous space to describe the propagation of the EM field to and from each element and allow for frequency-dependent attenuation and dispersion through the Jonscher constitutive formulation (Jonscher, 1999). The resulting forward modeling scheme is free from boundary effects related to the modeled domain size and also from discretization errors. We begin by describing the theory before proceeding with how we discretize a fracture, and, finally, we compare our forward modeling scheme to simulations based on a well-established numerical code and to laboratory data.

2.3. Theory

The electromagnetic properties of matter that characterize the velocity, attenuation and dispersion of electromagnetic (EM) energy in dielectric media are the magnetic permeability μ (N·A^{-2}), the electric permittivity ε (F·m^{-1}) and the conductivity σ (S·m^{-1}), or equivalently the resistivity, ρ (Ω·m), with $\rho = \frac{1}{\sigma}$. These parameters are in general complex-valued and frequency dependent, while for many practical geophysical purposes it is safe to assume the magnetic permeability to be constant and equal to the value in vacuum, $\mu_0 = 4\pi^{-7}$N·A^{-2}. Reflections and transmissions arise at the boundary between contrasting media and are a form of energy scattering. For geophysical purposes it is customary to use the macroscopic Maxwell equations as the governing physical principles to describe such systems (Nabighian, 1991). and the link between the propagating field to a given medium is made through the constitutive relations, $\mathbf{D} = \varepsilon\mathbf{E}$ and $\mathbf{J} = \sigma\mathbf{E}$, where $\mathbf{E}$ (V·m$^-$1) is the incident electric field arising from a distant source, $\mathbf{J}$ (A·m$^-$2) is the resulting current density and $\mathbf{D}$ (C·m$^-$2) is the electric displacement field.

There is a theoretical distinction between permittivity and conductivity because the first describes polarization effects resulting from bound charge and the second conduction effects resulting from free charge. In practice, these two parameters can be combined since one can only measure the in-phase and out-of-phase components of the current (Hollender and Tillard, 1998). It is thus convenient to define the effective permittivity ε_e (F·m^{-1}) with real and imaginary parts that characterize the propagation properties of the material: wave velocity, attenuation and dispersion.

2.3.1. The microscopic viewpoint

While the electric displacement field **D** was introduced by Maxwell and is proportional to the "bound" charge density within a dielectric (Purcell, 2011), it is only an approximation resulting from spatial averaging of a microscopic process that involves interaction between fields and particles that make up matter. The microscopic description was introduced by Lorentz (1909) and considers a dielectric as a collection of particles that undergo electronic polarization from an externally applied electric field. The applied field exists independently of the dielectric medium and travels through the dielectric medium at the speed of light in vacuum, that is, in the free space between the particles of the dielectric. As it travels through the medium it polarizes the particles that make up the dielectric, inducing moments of charge distribution in each particle. For neutral dielectrics it is only the electric dipole moment that needs to be considered and polarization can be seen as the result of an induced charge separation that generates an electric dipole moment for separation dL (m) between two opposite charges of equal magnitude q (C) and orientation. The electric field produced by such a dipole moment can be accurately calculated for an observation distance r (m) much larger than the charge separation dL producing the dipole moment and becomes exact in the limiting case, $\frac{dL}{r} \to 0$, in which the induced dipole is often called a point dipole. The dipole $\mathbf{p} = q \cdot dL \hat{\mathbf{p}}$ is oriented along $\hat{\mathbf{p}}$, which is the vector pointing between the two charges q, from the negative to the positive charge. The electric field of the point dipole is given by:

$$\mathbf{E}_\mathrm{d}(\mathbf{r}, \mathbf{p}) = \frac{1}{4\pi\varepsilon_0}\left(k^2(\hat{\mathbf{r}} \times \mathbf{p}) \times \hat{\mathbf{r}} + (3\hat{\mathbf{r}}(\hat{\mathbf{r}} \cdot \mathbf{p}) - \mathbf{p})\left(\frac{1}{r^2} - i\frac{k}{r}\right)\right)\frac{e^{ikr}}{r}, \tag{2.1}$$

where $\hat{\mathbf{r}}$ is a unit vector pointing from the point dipole to the point of observation $\mathbf{r} = r\hat{\mathbf{r}}$, r [m] is the magnitude of $\mathbf{r}$, $\varepsilon_0 \equiv 8.854... \times 10^{-12}\,\mathrm{F \cdot n^{-1}}$ is the electric permittivity in vacuum and $k\,(\mathrm{rad \cdot m^{-1}})$ is the wavenumber in vacuum. The implicit time dependence ($e^{-i\omega t}$) has not been included in eq. 2.1. The vacuum wavenumber is given by $k = \omega c^{-1}$, where $\omega\,(\mathrm{rad \cdot s^{-1}})$ is the angular frequency and $c \equiv 299792458\,\mathrm{m \cdot s^{-1}}$ is the speed of light in vacuum. Equation (2.1) includes the near, intermediate and far-fields generated by a dipole **p** located at the origin of the coordinate system. We use the subscript d in the electric field ($\mathbf{E}_\mathrm{d}$) to denote that it corresponds to a point dipole. A generalized expression for the electric field at an arbitrary location **r** generated from a dipole located at $\mathbf{r}'$ is easily obtained through the substitution $\mathbf{r} \to \mathbf{r} - \mathbf{r}'$. A detailed derivation of Eq. (2.1) can be found in classical electrodynamics textbooks (e.g., Jackson and Fox, 1999, Ch. 9).

Each particle in a dielectric medium is polarized by a superposition of the applied field generated by a source far away and the fields generated by all the other particles present in the dielectric. For a uniform distribution of polarizable particles and at large observation distances compared to the inter-particle spacing, one can define the average electric dipole moment $\langle \mathbf{p} \rangle$ (C·m) per unit volume V (m^3) as the polarization density $\mathbf{P} = \frac{\langle \mathbf{p} \rangle}{V}$ (C·m^{-2}). The average dipole moment of a homogeneous and isotropic region that is polarized by an incident plane wave gives the same polarization response as one would get by summing the fields of the individual particles. The polarization density **P** links the microscopic approach to the macroscopic description through the process of spatial averaging of the dipoles. The

electric displacement field can be written explicitly as $\mathbf{D} = \varepsilon_0 \mathbf{E} + \mathbf{P}$, highlighting that the macroscopic description implicitly includes the contribution from all the polarized particles in the electric displacement field, $\mathbf{D}$, through spatial averaging (Russakoff, 1970).

2.3.2. From a microscopic to a macroscopic description

The equivalence between the microscopic and macroscopic formulations has been rigorously proven through the Ewald-Oseen extinction theorem (Born and Wolf, 1999). This theorem states that for homogeneous and isotropic media that are linearly polarized by an externally applied field, the interaction between all the induced dipoles exactly cancels out parts of the applied field such that the resulting field propagates exactly as the electric displacement field $\mathbf{D}$ predicted by the macroscopic Maxwell's equations. This reduces the macroscopic theory to a special case of the microscopic approach, which is in its nature a more fundamental and intuitive description (Feynman et al., 1964).

Numerical implementations of the microscopic interactions between polarized dipoles and light have been long used by the astrophysical community. The discrete dipole approximation (DDA), or coupled-dipole approximation as introduced by Purcell and Pennypacker (1973) replaces a dielectric object with electric dipoles that are polarized by the local electric field. The local electric field takes into account the field radiated and induced by all the dipoles present, as well as the incoming field. This makes the DDA highly suitable for descriptions of irregular objects and the results compare well with exact theories, such as Mie and Rayleigh scattering (Yurkin and Hoekstra, 2007). Another important benefit of the DDA formulation compared to other numerical methods is that it does not require a bounded model domain; see Kahnert (2003) for an overview of numerical methods in EM scattering theory.

2.3.3. Reflection and transmission from scattering

The Ewald-Oseen extinction theorem applied to two semi-infinite regions of differing dielectric materials can be used to derive reflection and transmission coefficients (Fearn et al., 1996) that are identical to the Fresnel coefficients obtained by solving the macroscopic Maxwell's equations and matching boundary conditions across an interface. In the microscopic regime, the fields scattered from each particle superimpose exactly to give a resulting reflection and transmission that effectively occurs at the "boundary" between the two materials. It is worthwhile to note that the extinction of the applied field actually takes place throughout the whole volume of the dielectric, and not at the boundary as the macroscopic approach suggests. Moreover, the microscopic approach can account for conduction currents (Ballenegger and Weber, 1999).

In the case of a plane wave obliquely incident on a homogeneous dielectric layer of finite thickness (i.e. a planar fracture), the microscopic formulation successfully reduces to the effective Transverse Electric (TE) and Transverse Magnetic (TM) reflection coefficients that

are identical to those derived in optics (Lai et al., 2002):

$$R_{e,\{\text{TE,TM}\}} = \frac{R_{\{\text{TE,TM}\}}(1 - e^{-2ik_\text{t}d})}{1 - R_{\{\text{TE,TM}\}}^2 e^{-2ik_\text{t}d}}, \tag{2.2}$$

where the effective reflection coefficient for each mode can be readily computed by replacing the interface reflection coefficients, for TE or TM modes, in Eq. (2.2). The interface reflection coefficients depend on the incidence angle θ of the incoming wave, and are given by the following two equations:

$$R_\text{TE} = \frac{\mu_\text{t}\,k_\text{b}\cos\theta - \mu_\text{b}\sqrt{k_\text{t}^2 - k_\text{b}^2\sin^2\theta}}{\mu_\text{t}\,k_\text{b}\cos\theta + \mu_\text{b}\sqrt{k_\text{t}^2 - k_\text{b}^2\sin^2\theta}} \tag{2.3}$$

$$R_\text{TM} = \frac{\mu_\text{t}\,k_\text{b}\sqrt{k_\text{t}^2 - k_\text{b}^2\sin^2\theta} - \mu_\text{b}\,k_\text{t}^2\cos\theta}{\mu_\text{t}\,k_\text{b}\sqrt{k_\text{t}^2 - k_\text{b}^2\sin^2\theta} + \mu_\text{b}\,k_\text{t}^2\cos\theta} \tag{2.4}$$

To compute the wavenumber k_n, where the subscript n is used to denote a medium with effective permittivity $\varepsilon_{e,n}$ and magnetic permeability μ_n, one can use the following relation: $k_n = \omega\sqrt{\varepsilon_{e,n}\mu_n}$. In Eqns. (2.2 - 2.4) above, and in equations to follow, we use the subscript b to index the homogeneous matrix and t to index the dielectric and conductive thin-layer of thickness d. Frequency dependence of the reflection coefficient arises both through the explicit presence of the angular frequency in the wavenumber formula and the implicit frequency-dependence of the electric permittivity. These effective reflection coefficients have been successfully used in geophysical applications to describe GPR reflections from thin layers (Grégoire and Hollender, 2004; Tsoflias et al., 2004; Bradford and Deeds, 2006; Deparis and Garambois, 2008; Sassen and Everett, 2009).

2.3.4. Fractures seen as dipole scatterers

Reflections from a fracture with a homogeneous material filling would be accurately described by the effective reflection coefficient, Eq. (2.2), if the incoming electromagnetic field is a plane wave over the whole extent of the fracture. Since the wavelengths are often comparable in scale to the extent of the fractures, one can hardly expect the incoming field to strike with the same angle throughout. Therefore, energy exchanges across a fracture are often inadequately recovered by the Fresnel coefficients. We propose to circumvent this problem by discretizing fractures into regions along which the plane wave assumption is approximately valid. We can then treat the discretized regions from a microscopic perspective and describe the reflected energy using a combination of effective reflection coefficients and scattering from polarized dipoles.

We consider fractures embedded within a homogeneous and isotropic background dielectric medium with effective electric permittivity $\varepsilon_{e,\mathbf{b}}$ and magnetic permeability $\mu_\mathbf{b}$ (e.g. fractures in a uniform rock matrix). We account for the interaction of the electric field with this medium by replacing the vacuum wavenumber k in Eq. (2.1) by the wavenumber calculated in the background medium, $k_\mathbf{b} = \omega\sqrt{\varepsilon_{e,\mathbf{b}}\,\mu_\mathbf{b}}$. We thus replace the dipole-generated electric field ($\mathbf{E_\mathrm{d}}$) with the electric displacement field ($\mathbf{D_\mathrm{d}}$) by making the following substitution to Eq. (2.1):

$$k \to k_\mathbf{b} \implies \mathbf{E_\mathrm{d}}(x,y,z,\mathbf{p}) \to \mathbf{D_\mathrm{d}}(x,y,z,\mathbf{p}) \tag{2.5}$$

We proceed by discretizing each fracture into regions of constant thickness and length with homogeneous and isotropic electrical properties, which we refer to as elements. The homogeneity of each element allows us to assume a continuous distribution of dipoles within its volume with a response that can be described by the polarization density $\mathbf{P}$. Furthermore, by imposing the length of each element to be small compared to the wavelength of the incoming electric field, we can approximate the incoming wave to be plane over the extent of an element.

The electric displacement field ($\mathbf{D}^m$) scattered from an element indexed m is the superposition (summation) of the fields generated by all the dipoles within the element:

$$\mathbf{D}^m(x,y,z) = \sum_{n=1}^{N} \mathbf{D_\mathrm{d}}^m(x,y,z,\langle \mathbf{p}_n^m \rangle) = \mathbf{D_\mathrm{d}}^m\left(x,y,z,\oiiint \mathbf{P}^m(x',y',z')\,\mathrm{d}x'\,\mathrm{d}y'\,\mathrm{d}z'\right). \tag{2.6}$$

The summation in Eq. (2.6) is taken over the individual dipoles of a homogeneous element, but for observation distances that are large compared to the inter-dipole spacing we can replace this summation with a volume integral of the polarization density $\mathbf{P}$. We use primed coordinates to integrate over the volume of the element and unprimed coordinates to denote a different coordinate system outside the element that we call the experimental coordinate system, in which the observed field is measured. The element coordinate system is related to the experimental coordinate system by a dip and azimuth and the components of the electric field, when moving from one coordinate system to the other, can be calculated without loss of accuracy.

The Ewald-Oseen extinction theorem can be applied to reduce the dipole interaction along the direction normal to the element, z', to a process that is effective at the first intercepting boundary of the element with the incoming field. We denote the location of the first intercepting boundary by z_c. The reduction is achieved by the following substitution:

$$\iiint_{x',y',z'} \mathbf{P}^m(x',y',z')\,\mathrm{d}x'\,\mathrm{d}y'\,\mathrm{d}z' \to \iint_{x',y'} R_\mathrm{e}^m \overline{\mathbf{P}}^m(x',y',z_\mathrm{c})\,\mathrm{d}x'\,\mathrm{d}y', \tag{2.7}$$

where the polarization density $\mathbf{P}$ is replaced by a surface polarization density, $\overline{\mathbf{P}}\,(\mathrm{C \cdot m^{-1}})$. We use a line over vector quantities to indicate that they are surface variables that are evaluated over the first intersecting boundary of an element. The effective reflection coefficient R_e^m is applied locally for each element.

Furthermore, by allowing only elements with side length much smaller than the wavelength of the incoming wave, we can assume the incoming wave to be plane over the extent of an element. We use this assumption to reduce the surface integral over the intersecting boundary of the element to a simple multiplication by the boundary's area (A^m). Since the incoming wave is assumed to be a plane over the extent of an element, we only need to compute the polarization strength at one location along the first intercepting boundary and choose the center of the boundary, which we denote by $(x_\mathrm{c}, y_\mathrm{c}, z_\mathrm{c})$. The surface integral of Eq. (2.6) then becomes:

$$\iint_{x', y'} R_\mathrm{e}^m \overline{\mathbf{P}}^m(x', y', z_\mathrm{c})\, \mathrm{d}x'\, \mathrm{d}y' = A^m R_\mathrm{e}^m \overline{\mathbf{P}}^m(x_\mathrm{c}, y_\mathrm{c}, z_\mathrm{c}) \tag{2.8}$$

The right hand side term of Eq. (2.7) has the units of a dipole moment, but accounts for the total dipolar strength of an element. We call this term an "effective dipole" and denote it with the symbol $\mathbf{p}_\mathrm{e}^m\,(\mathrm{C \cdot m})$ for an element indexed m.

The effective dipole is proportional to the incoming electric field arriving from the antenna source, that we model as a dipole $\mathbf{p}_\mathrm{a}\,(\mathrm{C \cdot m})$ fixed at an arbitrary position $(x_\mathrm{a}, y_\mathrm{a}, z_\mathrm{a})$ in the experimental coordinate system (more on this in section 2.4.2). We denote the electric displacement field arriving from the antenna source by $\overline{\mathbf{D}}^m\,(\mathrm{C \cdot m^{-1}})$ to indicate that this field is computed along the first intersecting boundary of an element. The effective dipole is then given by:

$$\mathbf{p}_\mathrm{e}^m = A^m R_\mathrm{e}^m \overline{\mathbf{P}}^m(x_\mathrm{c}, y_\mathrm{c}, z_\mathrm{c}) = A^m R_\mathrm{e}^m \overline{\mathbf{D}}_\mathrm{d}(x_\mathrm{c}, y_\mathrm{c}, z_\mathrm{c}, \mathbf{p}_\mathrm{a}(x_\mathrm{a}, y_\mathrm{a}, z_\mathrm{a})). \tag{2.9}$$

The field $\overline{\mathbf{D}}_\mathrm{d}$ in Eq. (2.9) can be decomposed into a TE and TM mode and the corresponding effective reflection coefficients, Eqs. (2.2-2.4), can be used.

In summary, we use a microscopic approach up-scaled to the size of a dipole element that acts as an effective dipole, polarized by the source dipole (antenna), modulated by its effective reflection coefficient and scaled by its area of intersection with the incoming field. For a collection of many elements, the total scattered field is a superposition of the fields from every effective dipole. For M dipole elements, the total measured field $\mathbf{D}$ is:

$$\mathbf{D}(x,y,z) = \sum_{m=1}^{M} \mathbf{D}^m(x,y,z) = \sum_{m=1}^{M} \mathbf{D}_d^m\left(x,y,z,\mathbf{p}_e^m\right) =$$

$$\sum_{m=1}^{M} \mathbf{D}_d^m\left(x,y,z,A^m R_e^m \overline{\mathbf{D}}_d(x_c,y_c,z_c,\mathbf{p}_a(x_a,y_a,z_a))\right). \quad (2.10)$$

The recursive use of Eq. (2.1) in Eq. (2.10) arises from the representation of the antenna source and the fracture element as dipoles and highlights the similarity of our approach to the discrete dipole approximation used in astrophysics. A schematic of this interaction is shown in Fig. 2.1.
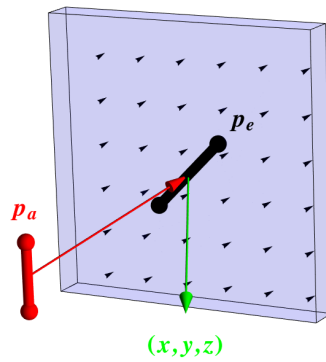
Figure 2.1 – Schematic of an element. The direction of the incident plane wave is shown by the (red) arrow pointing from the source dipole pa to the induced effective dipole pe. The secondary field (green) generated by the element is measured at the receiver location (x,y,z). The smaller (black) arrows are the "individual" dipoles within the dielectric.

2.4. Implementation

We now propose a strategy to implement the aforementioned effective-dipole forward modeling scheme. We begin by stating the underlying assumptions, we then proceed to give an effective description of the emitted GPR signals, proceed to generalize the method so that frequency-dependent properties can be assigned to the materials, and finally examine how to effectively discretize a fracture for a given survey configuration.

2.4.1. Assumptions about subsurface properties

The validity of the presented forward modeling scheme is limited by the following assumptions about the subsurface:

1. The rock matrix is a homogeneous and isotropic dielectric medium. This assumption is reasonable for many applications in fractured rock, for which the dominant heterogeneities are related to the fractures;
2. The fracture is a planar rectangular surface (other geometries could easily be considered);
3. The fracture filling is isotropic and polarizes linearly by the incoming field. The linear response is valid since the emitted signal is weak and well within the linear limits of dielectric Earth materials;
4. Magnetic effects are not taken into account and the magnetic permeability is set equal to μ_0 everywhere;

The forward problem is solved in the frequency domain.

2.4.2. Source signal generation

In a resistively loaded dipole antenna, a short pulse of current is exponentially damped along the antenna length and produces a dominant dipole moment that induces an electric field. The resulting electric field has a complicated structure arising from asymmetries in the antenna design, antenna coupling with the surrounding medium, noise in the system and other (often unknown) sources of error. We partly account for such uncertainties by modeling the antenna dipole moment with a generalized Gamma distribution (Stacy, 1962), thus allowing much more flexibility in the resulting shape of the dipole moment compared with a Gaussian distribution. The frequency-dependent response of the antenna dipole moment is given by:

$$\mathbf{p}_\mathrm{a}(\omega, \alpha, \beta, \gamma, \mu) = K(\omega - \mu)^{\alpha\gamma - 1} \mathrm{Exp}\left[-\left(\frac{\omega - \mu}{\beta}\right)^\gamma \right] \hat{\mathbf{r}}; \quad \omega > \mu \tag{2.11}$$

where α, β and γ are positive parameters that control the shape of the dipole moment distribution, $\hat{\mathbf{r}}$ is the orientation of the antenna, μ is a location parameter below which the distribution is zero-valued and K (C·m) is a normalization constant. Equation (2.11) reduces to a Gaussian distribution for $\alpha = 0.5$, $\gamma = 2$, $\mu = 0$ and with standard deviation β. Our approach to model an effective antenna source is similar, but not equivalent, to the newly-established full-waveform inversion method (Ernst et al., 2007). The latter approach has been successfully used in several studies to invert GPR data where the source wavelet is unknown (e.g., Klotzsche et al., 2013).

2.4.3. Frequency-dependent polarization

The polarization described until now is a form of electronic polarization, in which the bound charge distribution of a particle is instantaneously "reshaped" by the incoming field. The amount of reshaping is quantified by the electric susceptibility, $\chi_r = \varepsilon_r - 1$, where $\varepsilon_r = \frac{\varepsilon_e}{\varepsilon_0}$ and is in general frequency-dependent. The restoration time accompanied with the bound charge moving back in place causes an out-of-phase response that leads to energy loss. The overall effect of electromagnetic waves propagating through dielectric matter is to generate both polarization and conduction currents, a process often referred to as dielectric relaxation (Jonscher, 1999). For low-loss dielectric media, the Jonscher 'universal dielectric response' effectively describes the effects of polarization and static conduction for typical GPR frequencies (Hollender and Tillard, 1998). It can be reduced to three material-specific parameters; the real-valued high-frequency limit of the permittivity ε_∞ (F·m^{-1}), the static conduction loss σ_{dc} (S·m^{-1}) and the (unit-less) electric susceptibility χ_{r}. The frequency-dependent effective permittivity $\varepsilon_{\mathrm{e}}(\omega)$ is given by:

$$\varepsilon_{\mathrm{e}}(\omega) = \varepsilon_\infty + \varepsilon_0 \, \chi_{\mathrm{r}} \left(\frac{\omega}{\omega_{\mathrm{r}}}\right)\left(1 - \cot\left(\frac{n\pi}{2}\right)\right) - \frac{i\sigma_{\mathrm{dc}}}{\omega} \tag{2.12}$$

where ω_{r} is an arbitrary frequency best chosen as the dominant frequency of the emitted antenna signal and n is a dimensionless empirical parameter that ranges from 0 to 1 and characterizes the magnitude of dielectric loss.

2.4.4. Dipole discretization

To ensure that the electric field generated by the source arrives approximately as a plane wave over each element, it is necessary to use an element discretization that is much smaller than the dominant wavelength of the emitted signal. Note that only the first intercepting plane of a fracture needs to be discretized so the discretization is 2D. To determine appropriate discretization criteria, we perform a synthetic Monte-Carlo simulation in which we generate 100 fracture realizations of random thickness, orientation, and length (fractures are square), filled with water of conductivity $0.1\,\mathrm{S\cdot m^{-1}}$. The thicknesses were allowed to vary log-normally in the range of 0.1 mm to 10 cm while the orientation angles (0° to 60° in both dip and azimuth) and the fracture length (1 m to 10 m) were varied following a uniform distribution. The location of the midpoint of a fracture was randomly assigned to a maximum of 20 m away from the source location. The source and receiver were placed 3 m apart and we used a Gaussian distribution to generate the source dipole moment with a characteristic pulse corresponding to a dominant wavelength of 1 m, typical of a 100 MHz GPR antenna employed in crystalline rock.

To compare the gain in accuracy as a function of dipole discretization, we define a maximum discretization of 16 dipoles per (dominant) wavelength. This corresponds here to a dipole spacing of 6.67 cm in both tangential dimensions of a fracture. We compute the

Table 2.1 – Statistics of a Monte Carlo experiment with 100 fracture realizations. The measure used is the normalized root-mean-square difference in the (reflected) frequency response, at 500 frequencies spaced linearly from 1 MHz to 1 GHz, between the maximum (16 dipoles per wavelength) and coarser fracture discretizations.

Dipole Density	Maximum	75 % quartile	Mean	25 % quartile
1	0.43	0.29	0.22	0.15
2	0.34	0.24	0.15	0.09
4	0.15	0.06	0.04	0.02
8	0.02	0.01	0.01	0.01

forward model response at the receiver location with the fine discretization and for successive coarsening using 8, 4, 2 and 1 dipoles per wavelength. For a given coarsening (index c), we compute the deviation between the finest discretization (index t), that we assume to be the true response, to the coarser discretization, as the Root Mean Square (RMS) difference of N complex frequency amplitudes $\tilde{A}_i^{\{t,c\}}$ in the reflected response, given by:

$$\text{RMS}^c = \sqrt{\frac{1}{N} \sum_{1=1}^{N} \frac{|\tilde{A}_i^{\,t} - \tilde{A}_i^{\,c}|^2}{|\tilde{A}_i^{\,t}|^2}} \tag{2.13}$$

We compute the RMS deviation at 500 linearly spaced frequencies, from 1 MHz to 1 GHz, and tabulate the maximum, mean, 25% and 75% quartiles for each coarsening level in Table 2.1. The statistics show that the error is very small for 8 dipoles per wavelength, while the value of 4 dipoles per wavelength appears also satisfactory with one outlier which gives a 15% deviation and a mean error of 4%. The outlier corresponds to a large fracture (8 m side length) with a small thickness (0.1 mm), large dip (37°) and azimuth (29°), and a center that is located only 3 m away from the antenna midpoint. It is often the case in practical applications that the energy close to the GPR system (early arrivals) is dominated by the direct wave and the experimental accuracy is not sufficient to infer information from reflections in the near-borehole region. A discretization of 4 dipoles per wavelength appears thus sufficient for most practical applications.

A possible limitation of the current implementation of our forward-modeling approach is that we do not consider secondary reflections from neighboring fracture elements. With a discretization of 4 dipoles per wavelength (which amounts to dipoles placed ~33 cm apart in this analysis) the magnitude of the antenna-emitted electric field arriving at the center of each element is several orders of magnitude higher than the field arriving from the other elements. Therefore, using only the antenna source for polarizing each element has a negligible effect on the scattered response of a collection of elements.

2.5. Results

In this section, we compare the results of our effective-dipole (ED) forward modeling scheme with a FDTD code and to data from a laboratory experiment described by Grégoire and Hollender (2004).

2.5.1. Experimental set-up of the synthetic experiment

The synthetic study offers a comparison of our effective-dipole forward modeling scheme with numerical simulations based on GPRMax3D, a 3D FDTD code that has been used extensively for modeling GPR responses Giannopoulos (2005). The experimental layout is shown in Fig. 2.2. The background matrix material is homogeneous with $Re\{\varepsilon_e\} = 5\,\varepsilon_0$ and $\sigma_{dc} = 0.001\,\mathrm{S \cdot m^{-1}}$, where $\sigma_{dc} = i\omega Im\{\varepsilon_e\}$. The reflector is a conductive water-filled fracture oriented in the $\hat{y} - \hat{z}$ plane with material properties $Re\{\varepsilon_e\} = 81\,\varepsilon_0$ $\sigma_{dc} = 0.1\,\mathrm{S \cdot m^{-1}}$. The fracture (reflector) is square with a 2 m side length and 30 cm thickness. The thickness is chosen large enough to allow effective discretization with the FDTD code (2 cm node spacing in all 3 directions resulting in 15 nodes along the fracture thickness), but still within the thin-layer regime ($d = 0.3\,\lambda$) that is given by Bradford and Deeds (2006) as layer thicknesses less than $0.75\,\lambda$. For the FDTD code we used a spatial modeling domain consisting of a cube with an 8 m side length with absorbing boundaries (see bounding box in Fig. 2.2) to avoid boundary reflections.
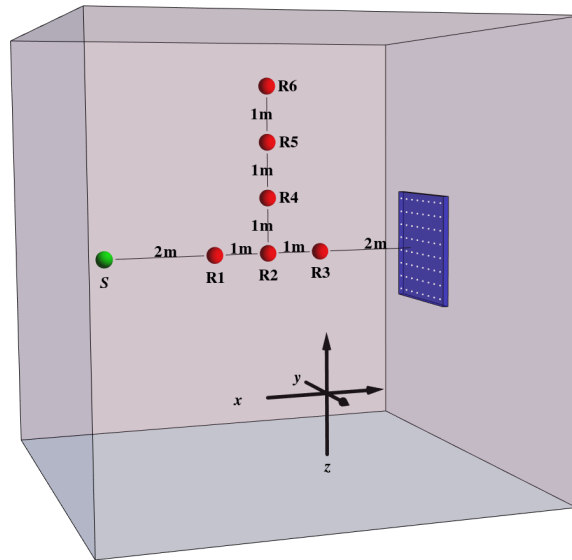
Figure 2.2 – Schematic of the synthetic experiment used to study propagation and reflection. The experiment coordinate system is shown with the axes in the bottom, receivers (red) are labeled R and the source (green) is labeled S. The square reflector is shown on the right (blue) with marks (white) indicating the dipole locations.

2.5.2. Comparison of propagation results without fracture

To compare propagation modeling results we use the horizontally placed receivers shown in Fig. 2.2. For the FDTD computation, we define a Ricker wavelet with central frequency of 100 MHz. The FDTD code implements a 'soft-source' by defining the current density over time at a given location in the grid to obtain a propagating Ricker wavelet. For our effective dipole computation we optimize the parameters of the source dipole moment distribution (described in section 2.4.2), starting with a Gaussian and using a local search algorithm to obtain a wavelet arriving at the first receiver, R1, that is similar, within 1% difference in amplitude and phase to the one obtained by the FDTD code. All subsequent results are normalized by the maximum amplitude of the propagating wavelet in R1, shown in Fig. 2.3a, and the same source parameters are used throughout section 2.5.3. The propagation results at each receiver location, R1, R2 and R3, are shown in Figs. 2.3a, 2.3b and 2.3c respectively. The results indicate that the two approaches produce very similar wavelets at all three receiver locations.
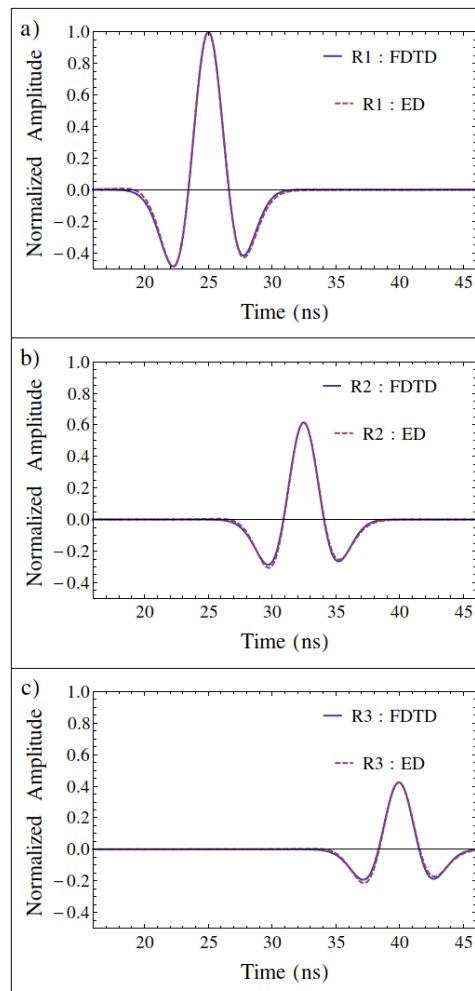
Figure 2.3 – Comparison of propagation from our effective-dipole (ED) and FDTD forward models, for the three horizontal receiver locations R1, R2 and R3 in Fig. 2.2.

2.5.3. Comparison of reflection results

To compare the differences in the reflected signal between our method and FDTD, we use both the horizontally placed receivers (R1, R2 and R3) and the vertically placed receivers (R4, R5 and R6) in Fig. 2.2. The results are presented in Figs. 2.4 and 2.5 respectively. The source pulse is generated using the same parameters and normalization as in the previous section. For all reflections, we see very good agreement between the early arriving energy, in both amplitude and phase, while the later arriving energy shows minor mismatches between the two methods.
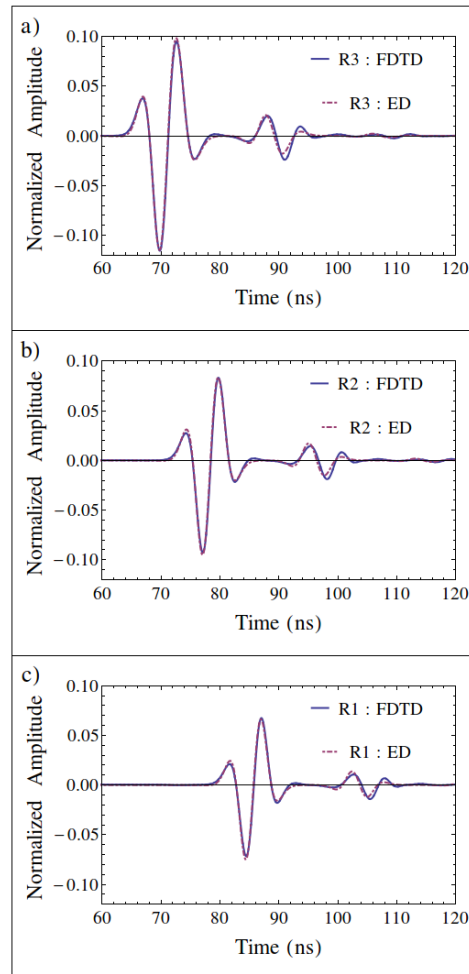
Figure 2.4 – Comparison of reflections from our effective-dipole (ED) and FDTD forward models, for the three horizontal receiver locations R1, R2 and R3 in Fig. 2.2.
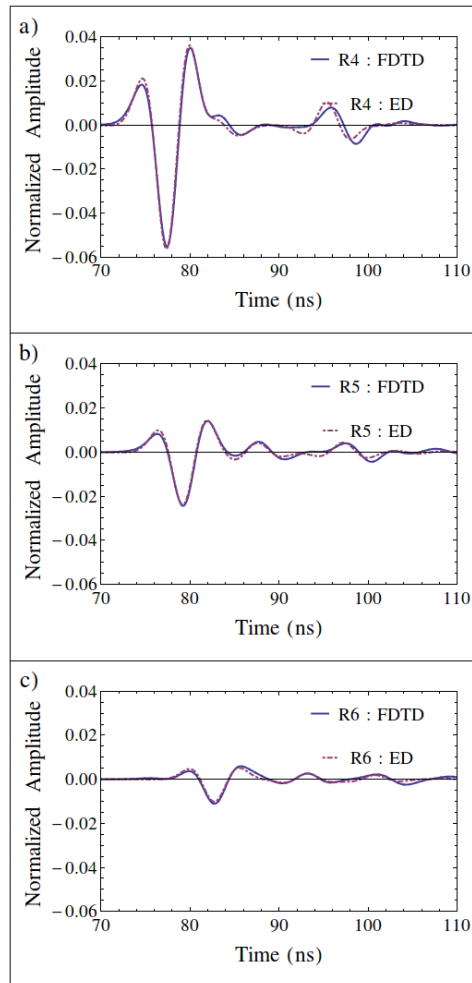
Figure 2.5 – Comparison of reflections from our effective-dipole (ED) and FDTD forward models, for the three vertical receiver locations R4, R5 and R6 in Fig. 2.2.

2.5.4. Comparison to laboratory results

In this section, we compare the results of our effective-dipole forward modeling scheme to the laboratory results presented by Grégoire and Hollender (2004). In these experiments (see Fig. 2.6), two granitic blocks are held apart by 5 and 2.5 mm, while the separation between the blocks is filled with materials of varying properties. The electric properties of the filling materials are measured in the laboratory using a dielectric probe kit, and a 900 MHz bi-static GPR antenna is used to measure the reflection arising from the thin layer. It was not possible to simulate this experiment with the FDTD code because of memory limitations in defining a sub-millimeter discretization in a meter-scale 3D domain.

As a first comparison between our effective-dipole simulation and the laboratory data, we use a Gaussian pulse with a central frequency around 900 MHz. We allow for frequency-dependent attenuation and dispersion using the Jonscher parametrization given in Eq. (2.12). Grégoire and Hollender (2004) give a set of reduced parameters that they use in an alternative formulation of the Jonscher parametrization. From these parameters it is possible to derive
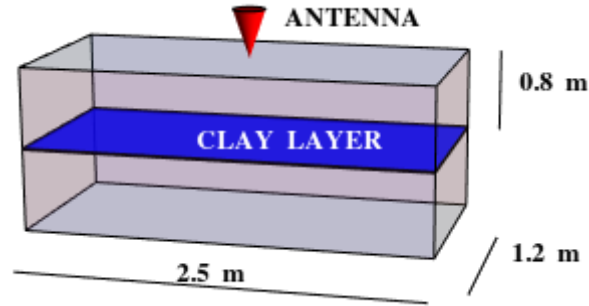
Figure 2.6 – Schematic of the laboratory setup by Grégoire and Hollender (2004). The rectangular (blue) sheet indicates the location of the reflective clay layer and the (red) cone indicates the location of the GPR antenna while the bounding cuboid (gray) represents the two granite blocks surrounding the clay layer.

Table 2.2 – Jonscher parameters used, to account for frequency dependent attenuation and dispersion, in simulating the laboratory results of Grégoire and Hollender (2004). The first three parameters are unit-less.

Material (Units)	n	χ	$\varepsilon_\infty/\varepsilon_0$	$\omega_c/2\pi$ (MHz)	σ_{dc} (S·m^{-1})
Granite	0.93	0.7	5.3	800	0.003
Saturated Clay	0.69	14	47	800	0.68

the original Jonscher parameters (see Table 2.2). Following Grégoire and Hollender (2004), we present the laboratory and simulated data (Fig. 2.7) normalized to the reflection from the 5 mm clay layer. The observed amplitude difference between the 5 mm and 2.5 mm saturated clay layer is reproduced well, but the wavelet shape and duration is poorly reproduced by using the Gaussian antenna-pulse. Figure 2.8 shows a comparison between the laboratory-measured and simulated (reflected) frequency amplitudes from the 5 mm layer.

We now investigate to what extent the agreement between the forward simulations and the laboratory data can be improved by allowing the shape of the antenna pulse to vary according to Eq. (2.11). For the 5 mm experiment, we search for the pulse that gives the smallest RMS, as defined in Eq. (2.13), between the laboratory-measured and modeled reflected energy spectrum, at 10 linearly spaced frequencies. We use a local search algorithm to compute the optimal pulse and converge to a solution with 7% RMS error, compared to the initial RMS of 30% that was obtained by using the Gaussian pulse as a source. In Fig. 2.8 we show the reflected frequency spectrum, obtained by applying the optimal pulse through Eq. (2.11), along with the frequencies used for the optimization. The optimal antenna pulse generates a signal with a significantly lower frequency content than the purely Gaussian pulse.

Our simulation results (Fig. 2.7) show that optimizing a generalized Gamma distribution to model the antenna-pulse shape can help to reproduce the pulse width and location of maxima and minima, as well as complex patterns in the signal such as the wide peak appearing after 3 ns. The amplitude and phase in the reflected signals seem to coincide, for the most part, except for the initial and final peaks that are not exactly reproduced in our simulations. Here, we do not seek to exactly reproduce each aspect of the reflected wave

46
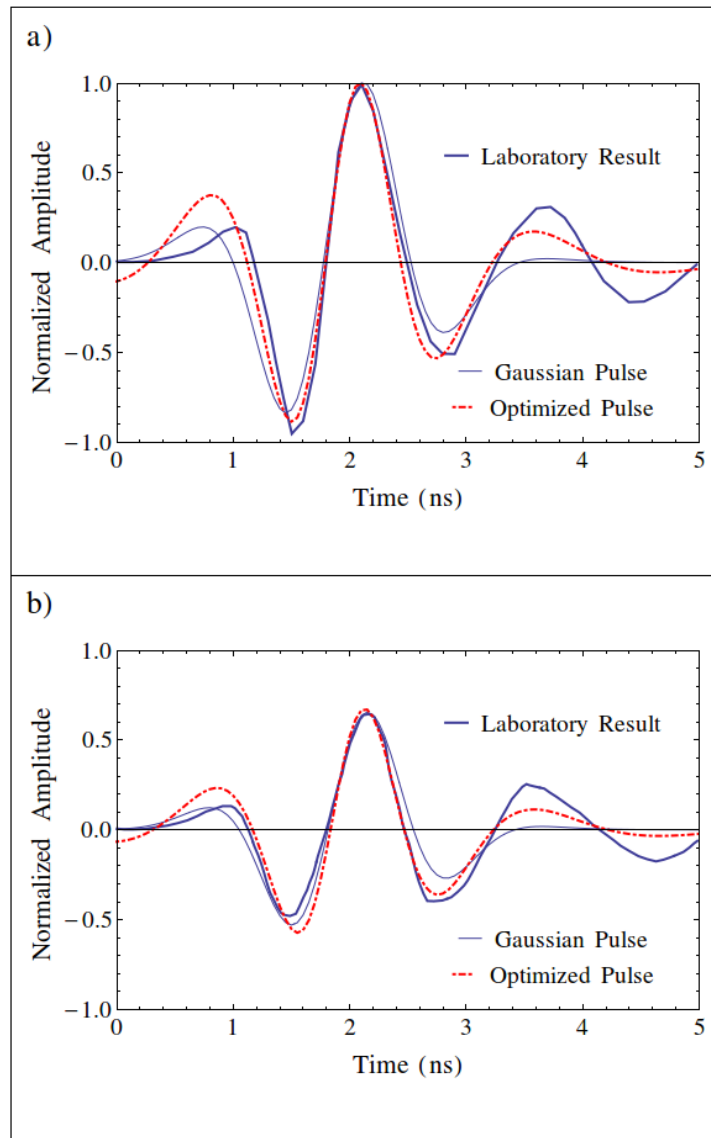
Figure 2.7 – Comparison of the reflected electric field acquired from laboratory data of Grégoire and Hollender (2004) and computed using the effective-dipole forward model with a Gaussian pulse and an optimized pulse as the antenna-source. Results are shown for (a) a 5 mm layer and (b) a 2.5 mm layer. The time origin for this plot is set as the onset of the reflection seen in the laboratory data, and the modeled reflections are time-shifted to match this onset time.

(that may also be affected by phenomena that we do not model, such as antenna ringing, but instead we aim to adequately reproduce the phase and amplitude of the dominant peaks.
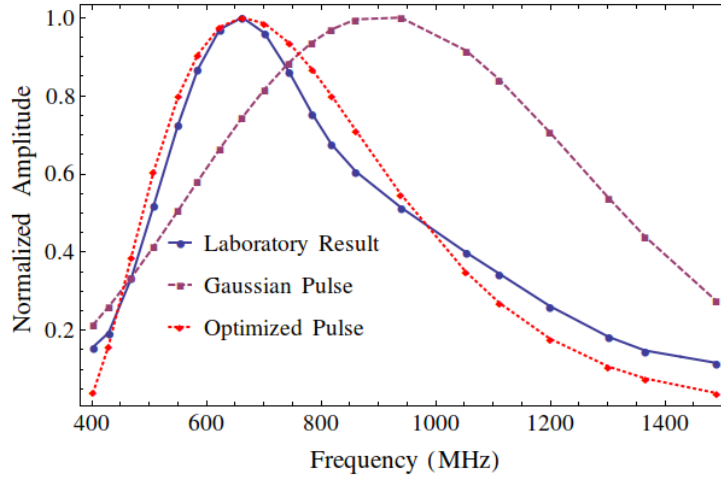
Figure 2.8 – Comparison between the reflected frequency spectra of the Grégoire and Hollender (2004) laboratory experiment (5 mm layer) using a Gaussian pulse, centered around 900 MHz, and an optimized pulse. The frequencies used for the optimization of the pulse are shown with markers on the plots and the parameters used to generate the optimal antenna pulse in Eq. (2.11) are $\alpha = 4$; $\beta = 0.05$; $\gamma = 0.79$; $\mu = 0.38$.

2.6. Discussion

The comparison between our effective-dipole method and FDTD simulations provides many illuminating results. Primarily, propagation of the electric field (Fig. 2.3) compares very well both in terms of attenuation and dispersion of the wavelet. Additional tests (not shown here) demonstrate significant numerical grid dispersion (e.g., when using a slightly coarser discretization of 3 cm) in the FDTD results, which is not a problem in our approach as analytic closed-form solutions are used in all calculations.

The reflected wavelets (Figs. 2.4 and 2.5) show some subtle differences between the two methods. For both horizontally and vertically placed receivers the results agree well between the FDTD and our effective-dipole formulation in both amplitude and phase. At closer inspection, one can see minor discrepancies in the later arrivals of the reflected energy. We have performed tests with higher conductivities of the water-filled fracture where the later arrivals are not visible, and instead only the first four peaks are prominent and agree well (as shown here) between the two methods. We postulate that these later arrivals are a result of the infinite internal reflections within the fracture, which are calculated in fundamentally different ways for the two methods. In our effective-dipole formulation we use analytical solutions from optics to account for the internal reflections while the FDTD code accounts for these iteratively. The latter would only approach the exact limit in the case of infinitely fine temporal sampling.

While numerical dispersion can be counteracted using finer discretizations, and boundary reflections can be minimized using a larger domain and/or more effective boundary conditions, it is often computationally demanding to apply efficient discretization schemes in an effective manner. This is especially evident when studying fractures with thicknesses

at the millimeter scale in a domain of several meters, let alone tenths of meters as in most field applications. Recent FDTD work has been focused on using sub-grid discretizations to model the interaction of EM waves with very small layers (Diamanti and Giannopoulos, 2009), but the problem of efficiently discretizing irregular geometries (e.g., highly dipping fractures) remains and the computational constraints are still high for 3D implementations. Our approach does not suffer from these drawbacks, and layers of arbitrarily small thickness can be considered at any distance from the source. Furthermore, there are no boundary effects in our formulation.

The comparison to the laboratory data, shown in Fig. 2.7, suggests that the effective-dipole forward model is physically sound, since the phase delays and, especially, the amplitudes of the measured and modeled wavelets match well. Furthermore, using the generalized Gamma distribution to define the dipole moment of the source allows us to model an effective signal that accounts for uncertainties in the emitted signal in a satisfactory manner. The optimized pulse generates a signal with significantly lower frequency content than the equivalent Gaussian pulse with a peak at the antenna dominant frequency, as is expected in practice for GPR applications.

For our effective-dipole model, the forward model has to be run individually for each source-receiver combination, but the approach is fully parallelizable and can be easily implemented using parallel computing. Computationally, the effective-dipole model provides a faster alternative to traditional numerical approaches and can decrease computation times by several orders of magnitude. In the synthetic experiment, the FDTD simulations takes approximately two hours while the effective-dipole model takes only 30 seconds to compute the response for each source-receiver pair, totaling 3 minutes for the whole experiment (2.9 GHz CPU with 7.5 GB RAM PC running Ubuntu). Typical discretizations for practical applications may be on the order of 1000 dipoles, for which one frequency component can be computed in approximately 0.5 second on a standard PC.

2.7. Conclusions

We present a forward model that describes the propagation of electromagnetic waves through a dense homogeneous dielectric medium and scattering at thin planar layers. We discretize the layers into elements that respond as polarized dipoles, modulated by the effective reflection coefficients of thin layers. We account for frequency-dependent electrical properties of the media through the Jonscher formulation, and model uncertainties in the emitted signal by using a generalized Gamma distribution as a current source. Our model compares well with finite-difference time-domain (FDTD) computations and does not suffer from numerical inaccuracies or boundary effects. Compared to FDTD, we are able to introduce reflectors of arbitrary size, thickness, material filling and orientation without compromising accuracy. We are also able to simulate laboratory data that we are not able to simulate with the FDTD approach. Optimizing the pulse shape through the generalized Gamma distribution further improved the agreement with the laboratory data. Computation times are orders of magnitudes smaller than FDTD and the approach is easily parallelizable. This forward

modeling approach will soon be coupled with flow and transport simulations in discrete fracture networks to infer transport behavior at experimental hydrological field sites.

Chapter 3

Apparent apertures from ground penetrating radar data and their relation to heterogeneous aperture fields

Alexis Shakas and Niklas Linde.

3.1. Abstract

Considering fractures with heterogeneous aperture distributions, we explore the reliability of constant-aperture estimates derived from ground penetrating radar (GPR) reflection data. We generate geostatistical fracture aperture realizations that are characterized by the same mean-aperture and variance, but with different Hurst exponents and cutoff lengths. For each of the 16 classes of heterogeneity considered, we generate 1000 fracture realizations from which we compute GPR reflection data using our recent effective-dipole forward model. We then use each (noise-contaminated) dataset individually to invert for a single 'apparent' aperture, i.e., we assume that the fracture aperture is homogeneous. We find that the inferred 'apparent' apertures are only reliable when fracture heterogeneity is non-fractal (the Hurst exponent is close to 1) and the scale of the dominant aperture heterogeneities is larger than the first Fresnel zone. These results are a direct consequence of the non-linear character of the thin-bed reflection coefficients. As fracture heterogeneity is ubiquitous and often fractal, our results suggest that robust field-based inference of fracture aperture can only be achieved by accounting for the non-linear response of fracture heterogeneity on GPR data.

3.2. Introduction

Rock fractures play an important role in many hydrogeological and geotechnical processes (e.g. NRC, 1996). For instance, fractures can act as conduits (or barriers) for fluid flow in petroleum and groundwater reservoirs. Hydraulically significant fractures play a determinant role in the transport of chemicals and their properties need to be known in order to determine suitable safety measures, such as in the design of a nuclear waste repository (Tsang et al., 2015). Moreover, fracture detection is important for rock-fall hazard assessment (e.g., Jeannin, Garambois, Grégoire, and Jongmans, 2006), safety inspection of buildings (e.g., Patriarca, Lambot, Mahmoudzadeh, Minet, and Slob, 2011) and can even aid as a precursor for volcanic eruptions (Kilburn and Voight, 1998). Therefore, the identification and characterization of rock fractures is arguably a fundamental problem in groundwater hydrology and applied geophysics. Nonetheless, this remains very challenging in practice as fracture properties often need to be deduced from indirect geophysical data or through hydrogeological experiments, such as tracer tests.

Rock fractures often have a material filling with highly contrasting electrical properties to the host rock, such as water–filled fractures in granite. Such a setting is ideal for ground penetrating radar (GPR) imaging since the strong property contrast - often both in terms of electrical permittivity and conductivity - makes it possible to detect, at high resolution, fractures with apertures that are several orders of magnitude smaller than the dominant wavelength of the source wavelet (e.g., Grasmueck, 1996). In the latter case, the interference of the source wavelet with the fracture walls results in a superposition of reflections (transmissions), such that no distinction can be made between the individual reflections (transmissions) arising from the two interfaces of the fracture. Below this limit, derived by Bradford and Deeds (2006)

as $\frac{3}{4}$ of the dominant GPR signal-wavelength, fracture aperture has been classically estimated by invoking the thin-bed approximation.

The ability of GPR to image fractures has been studied both theoretically (Bradford and Deeds, 2006; Deparis and Garambois, 2008) and in controlled experiments (Grégoire and Hollender, 2004; Tsoflias and Hoch, 2006). Field studies have successfully imaged fractures in reflection (Dorn et al., 2012) and transmission (Tsoflias et al., 2004; Sassen and Everett, 2009) mode. Furthermore, time-lapse imaging experiments have demonstrated the potential of GPR to dynamically image transport of electrically conductive tracers (Day-Lewis et al., 2003; Talley et al., 2005; Tsoflias et al., 2001; Tsoflias and Becker, 2008; Dorn et al., 2011; Shakas et al., 2016). A recent study by Tsoflias et al. (2015) suggests that multipolarization GPR data can better constrain flow chanelling, however, it is not always possible to obtain all components of the GPR signal (e.g., for conventional borehole GPR systems). Nevertheless, the challenge remains on how to effectively interpret the information content in the GPR signal to make reliable aperture estimates in the presence of fractures with heterogeneous properties (i.e., any fracture found in a natural system). To date, virtually all GPR studies have relied on the implicit assumption of constant aperture and material properties over the first Fresnel zone.

The impracticality of fully-numerical models, such as finite-difference time-domain (FDTD), to adequately simulate very thin and heterogeneous fractures is mainly related to discretization. Using the traditional FDTD approach, one would need to discretize a fracture with at least 10 nodes (e.g. 0.1 mm node spacing for a 1 mm aperture) to accurately capture the GPR source-wavelet interaction with the fracture filling. Assuming a 100 MHz dominant source-wavelength and a granitic host rock in a typical modeling domain (e.g. a cube that spans at least 10 meters in each dimension) the FDTD model would require Maxwell's equations to be solved on 10^{14} nodes. Such a problem is extremely challenging (often impossible) to model numerically. Additionally, inadequate discretization, the introduction of slanted surfaces in the often-used Cartesian grid and the artificial imposition of boundaries in the modeling domain lead to unwanted numerical artifacts. These disadvantages can be overcome with alternative modeling tools, such as the Finite Element method (e.g., Mukherjee and Everett, 2011), that can efficiently model fractures with the use of thin elements and mesh refinement, but has not been widely used in the GPR community.

An alternative approach to simulate GPR reflection and transmission in fractured rock is to use analytic solutions for thin-layer interference. Widess (1973) was the first to relate the effect of thin-bed (or thin-layer, as it was originally introduced) properties on geophysical data. In his classic article, Widess examined the reflective properties of a geological layer whose thickness is small compared to the incoming seismic wavelength. In the electromagnetic (EM) counterpart, the same response arises from solving Maxwell's equations on the boundaries of a thin-bed. This leads to the well-known optics phenomenon called 'thin-film interference' (e.g., Orfanidis, 2002, Ch. 5). The resulting equations can be separated into transverse electric (TE) and transverse magnetic (TM) modes.

Several studies use the EM thin-bed reflection coefficients to model the GPR response. For example, Grégoire and Hollender (2004) invert for the electrical properties of a filling between two granitic blocks using GPR reflection data from a laboratory experiment, Deparis and Garambois (2008) use common offset GPR reflection data to invert for electrical properties

and aperture of a single fracture, Tsoflias and Becker (2008) use multifrequency GPR to investigate the relationship between fracture aperture and fluid electrical conductivity, Sambuelli and Calzoni (2010) successfully model GPR reflections from a mm-thin fracture in a marble block and compare them with a controlled experiment and Sassen and Everett (2009) use polarimetric GPR transmission data to determine electrical properties and aperture of a single fracture. More recently, Babcock and Bradford (2015) use GPR reflection data to quantify electrical properties and thickness of thin and ultra-thin nonaqueous-phase liquid layers and Grobbe and Slob (2016) couple the thin-bed reflection coefficients to simulate the seismo-electric effect. In all these studies, the analogy between a fracture and a thin-bed is made.

The validity of the EM thin-bed solution depends on two conditions: (1) that the incoming field arrives as a plane wave over the whole thin-bed interface and (2) that the thin-bed extends infinitely along the plane of incidence. Both assumptions are violated to varying extent in practice. Another basic disadvantage of the thin-bed approach is that the aperture (thickness) and electrical properties of the bed are constant. In reality, fracture aperture variations within a fracture span several orders of magnitude (e.g., Bonnet, Bour, Odling, Davy, Main, Cowie, and Berkowitz, 2001). Moreover, studies that utilize GPR to detect the presence of an electrically conductive tracer in a fractured system are confronted with highly heterogeneous tracer distributions, and consequently electrical conductivity, in the involved fractures, that can lead to signal depolarization (Tsoflias et al., 2015).

Another way to solve the thin-bed interference problem relies on an analogy to the microscopic treatment of electromagnetic wave propagation in dielectric media. The analysis begins with the realization that optical phenomena, such as thin-bed interference, are in fact based on macroscopic (bulk) representations of the dielectric properties of a material that can be derived as space-time averages of a more fundamental microscopic treatment (Russakoff, 1970). Microscopically, a dielectric is treated as a collection of discrete elements (electrons at the smallest scale) that can be polarized by the incoming field. For the typical frequencies used in GPR applications (MHz to GHz range), the dominant mechanism is molecular polarization in which polar molecules (such as water) rotate in response to the incoming field and then release energy during relaxation (e.g., Jol, 2008, sec. 2.3). The collective sum of responses from all the polarizable elements exactly reproduces the (retarded) electromagnetic wave that one observes in dielectric media, which precisely reduces to the Fresnel equations on dielectric boundaries (Fearn et al., 1996) and accurately explains thin-bed interference (Lai et al., 2002).

We have recently presented how this analogy to the microscopic viewpoint can be used to efficiently simulate the electromagnetic response of a fracture of arbitrary properties, embedded within a homogeneous dielectric medium (Shakas and Linde, 2015). Our approach, that we refer to as the effective-dipole method, consists of discretizing the fracture into a large collection of dipole elements. Each element radiates as an electric dipole that is modulated by the thin-bed reflection coefficients. Discretizing the fracture into elements provides two advantages: (1) we can account for the variation of the incoming field (intensity and orientation) along the fracture for a given antenna radiation pattern and (2) we can account for variations in electric and geometric properties of a finite-sized fracture (i.e., allow for heterogeneity in the fracture filling and aperture). Moreover, the effective-dipole method

54

offers computation times that are several orders of magnitude smaller than FDTD simulations. A similar approach has been used by Michalski and Zheng (1990) to model radiation and scattering from perfectly conducting objects and later extended to magnetic dipoles in order to model underground unexploded ordnance by Shubitidze et al. (2002).

It is presently unclear if aperture estimation based on fully analytic forward models that rely on the thin-bed reflection coefficients is reliable in the presence of heterogeneous fracture properties. This question is addressed here by using our effective-dipole method, that offers the first opportunity to simulate realistic GPR responses from heterogeneous fractures. Initially, we confirm that the thin-bed forward model is reliable when considering a large enough and homogeneous fracture. Considering fractures with constant apertures, we demonstrate that aperture can be reliably estimated using a simple over-determined inversion scheme. We proceed by assigning heterogeneous fracture properties using the power spectrum method (a Fourier transform technique). We then demonstrate the ability of our effective-dipole method to reproduce 3D FDTD simulations for a fracture with a heterogeneous conductivity distribution. After this, we use the effective-dipole method to simulate noise-contaminated GPR reflection data from fractures with highly heterogeneous aperture distributions. To accomplish this, we create 16 classes of geostatistical models that all share the same mean aperture and variance, but exhibit different Hurst exponents and cutoff lengths. The Hurst exponent and cutoff-length define the trade-off between the fractal nature (equal aperture heterogeneity present at all scales) and size of the largest aperture heterogeneity, respectively. Within each class, we evaluate 1000 fracture realizations. From the resulting dataset, we infer the apparent constant-aperture of a homogeneous fracture whose GPR response, using the thin-bed forward model, best reproduces the data. These apertures are compared with spatial averaging weights derived from the sensitivity of the effective-dipole forward model for the given geometrical setup and a constant aperture fracture. Using these weights we obtain a weighted (mean) aperture, for each fracture realization, that we compare to the corresponding inferred (apparent) aperture. Based on this comparison, we present the conditions under which aperture heterogeneity leads to aperture estimates that are widely different from a linear average of the fracture aperture field.

3.3. Methodology and theoretical background

In this section, we first introduce the thin-bed forward model. We proceed by defining the modeling domain considered, with a single fracture present in a homogeneous rock matrix. We then describe the technique used to simulate heterogeneous fracture properties and use both FDTD and our effective-dipole method to simulate the GPR response for a fracture with a highly heterogeneous conductivity distribution. For all simulations, we use the same relative electric permittivity ($\varepsilon_r = 9$) and electric conductivity ($\sigma = 0.001$ S/m) for the background matrix.

3.3.1. The thin-bed forward model

The thin-bed reflection coefficients can be derived from the macroscopic Maxwell's equations by considering an electromagnetic field impinging a layer with contrasting electrical properties to a background material (e.g., Orfanidis, 2002, sec. 4.4). The same solutions are obtained by modeling the contrasting layers as a collection of dipoles and summing up their contribution (Lai et al., 2002). Both derivations rely on two basic assumptions: (1) that the incoming field strikes the layer with a constant (or periodic) angle, phase and amplitude everywhere and (2) that the layer has homogeneous properties and extends infinitely.

When these assumptions hold, the thin-bed reflection coefficients can be used to simulate GPR reflections resulting from a fracture with aperture a, through the following forward model:

$$\mathbf{E}_r(\mathbf{x}_s,\mathbf{x}_r,k_b,k_a,\theta) = \mathbf{E}_s(\mathbf{x}_s,k_b)\mathbf{R}_e(k_b,k_a,\theta)\mathbf{F}(*)\frac{e^{-ik_bx_r}}{x_r}, \tag{3.1}$$

where k_b (k_a) is the complex wavenumber $k = \frac{\omega}{c}\sqrt{\varepsilon_r + \frac{i\sigma}{\omega}}$ in the background matrix (thin-bed) that depends on the angular frequency ω, relative electric permittivity ε_r and electric conductivity σ. Both materials are assumed to be non-magnetic and the speed of light in vacuum is $c \equiv 299\,792\,458\,\mathrm{m\cdot s^{-1}}$, $\mathbf{E}_r$ is the electric field measured at the receiver location and $\mathbf{E}_s$ is the electric field from an infinitesimal electric dipole source $\mathbf{p}$,

$$\mathbf{E}_s(\mathbf{x}_s,k_b) = \frac{c^2}{4\pi\varepsilon_0}\left(k_b^2(\hat{\mathbf{x}}_s \times \mathbf{p}) \times \hat{\mathbf{x}}_s + (3\hat{\mathbf{x}}_s(\hat{\mathbf{x}}_s \cdot \mathbf{p}) - \mathbf{p})\left(\frac{1}{x_s^2} - i\frac{k_b}{x_s}\right)\right)\frac{e^{ik_bx_s}}{x_s}, \tag{3.2}$$

where $\hat{\mathbf{x}}_s$ is the unit vector and $x_s = ||\mathbf{x}_s||^2$ is the Euclidean distance. The dipole source $\mathbf{p}$ is described by a gamma distribution (Shakas and Linde, 2015) to allow for variations in the radiated electric field, $\mathbf{E}_s$. The 3D cartesian vectors $\mathbf{x}_s$ and $\mathbf{x}_r$ point from the source to the thin-bed center and from the thin-bed center to the receiver, respectively (see Fig. 3.1). The thin-bed reflection coefficients, $\mathbf{R}_e$, are given by (Orfanidis, 2002, sec. 7.2):

$$\mathbf{R}_e(k_b,k_a,\theta) = \frac{\mathbf{R}(1 - e^{-2iak_a\cos\theta})}{1 - \mathbf{R}^2 e^{-2iak_a\cos\theta}}, \tag{3.3}$$

where $\mathbf{R}$ may represent the transverse-electric (TE) or transverse-magnetic (TM) Fresnel reflection coefficient and the incidence angle θ is determined by the orientation of the vectors $\mathbf{x}_s$ and $\mathbf{x}_r$. Eq. (3.3) is not restricted to modeling a thin-layer but also reduces to the Fresnel reflection coefficients as the aperture increases (Lai et al., 2002), making the exponential term negligible.

Uncertainties in the forward modeling process, such as the coupling of the source and/or receiver, are often treated separately (e.g., Grégoire and Hollender, 2004; Deparis and Garambois, 2008). Here, we use $\mathbf{F}(*)$ to indicate source and receiver related modeling uncertainties, making our forward model analogous to the ones used by other authors. For the modeling exercises to follow, we set $\mathbf{F}(*) = 1$, since we use the same (known) source for both the effective-dipole and thin-bed forward models. Finally, the last term on the right hand side of

eq. (3.1) accounts for the dispersion, attenuation and spherical spreading of the reflected electric field propagating from the thin-bed to the receiver.
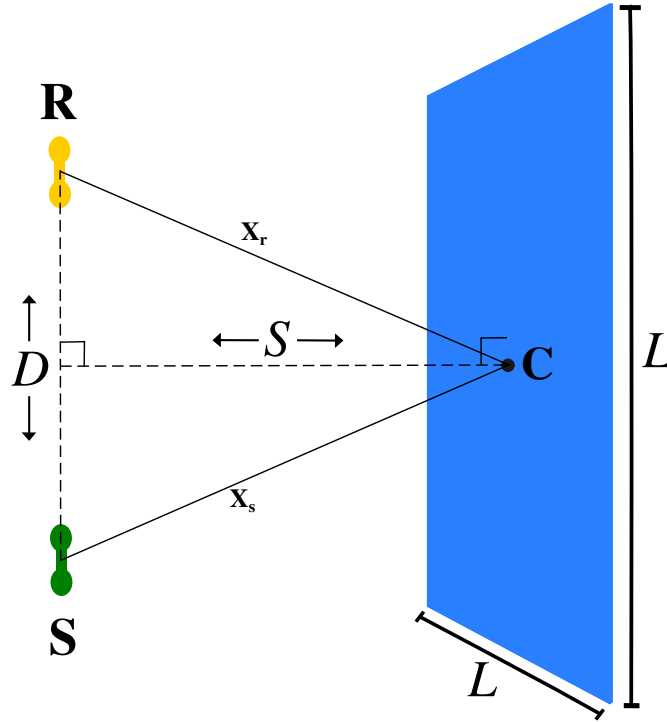
Figure 3.1 – Schematic of the fracture model and the acquisition geometry. The source (**S**) and receiver (**R**), offset by a distance D, are separated by the fracture by a distance S. The fracture midpoint is **C** and has a side length L. For the thin-bed forward model, the source propagates to the fracture midpoint and back to the receiver, shown by the vectors $\mathbf{x}_s$ and $\mathbf{x}_r$ respectively.

3.3.2. GPR response from a homogeneous fracture

In order to make a valid comparison between the thin-bed and effective-dipole forward responses, we must define an appropriate modeling domain such that the fracture is large enough to avoid that its edges contribute significantly to the reflected response. To accomplish this, we consider a square fracture with side length L and center **C** that is separated from both source and receiver by S. The source-receiver offset is given by D and the normal to the fracture plane at **C** runs through the source-receiver midpoint. A schematic of this model is shown in Fig. 3.1.

The fracture side length L must be large compared to the maximum source-receiver offset so that the boundaries do not affect the actual GPR response. The minimum side length necessary is expected to be inversely related to the maximum source-receiver offset (D_{max}). To compute this length, we set $D_{max} = 2$ m and create fractures with side length $L = \{5, 8, 10, 20, 30, 40, 50, 60\}$ m. We then simulate the GPR reflection data from these fractures, using the effective-dipole method, for different fracture apertures and conductivities $a = \{$ 0.1, 1,

10} mm and $\sigma = \{0.01, 0.1, 1\}$ S/m, respectively, and a constant relative electric permittivity, $\varepsilon_r = 81$. In Fig. 3.2 we present the simulated reflected traces for $L = \{5, 8, 10\}$ m, $a = 5$ mm and $\sigma = 0.1$ S/m. The effect of the fracture boundaries (also verified with FDTD simulations that are not shown here) manifests as a secondary reflection that diminishes and arrives later with increasing L (e.g., Pearce and Mittleman, 2002). For $L \geq 20$ m, we find that the difference in simulated amplitudes to the $L = 60$ m response is less than 0.01%. This is very small compared with typical error levels and we set $L = 20$ m in the following simulations.
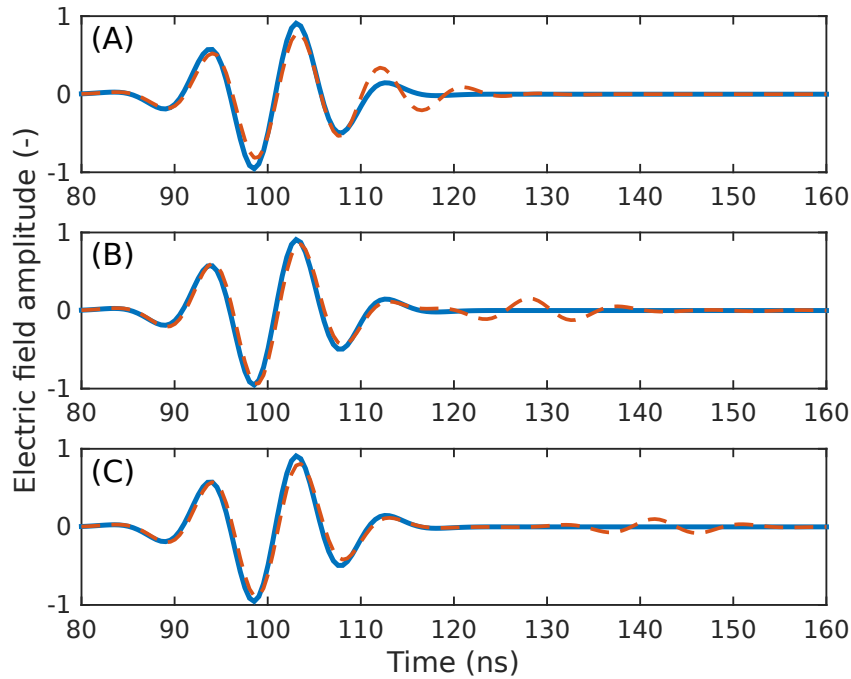
Figure 3.2 – Simulated reflected traces for fractures with $a = 5$ mm and L equal to (A) 5 m, (B) 8 m and (C) 10 m. Acquisition parameters are $S = 5$ m and $D = 2$ m (see Fig. 3.1). Results are presented for the thin-bed (solid) and effective-dipole (dashed) forward models. For each model type, the response is normalized such that the maximum amplitude is 1.

3.3.3. Fractures with heterogeneous properties

Natural fractures barely resemble thin-beds. Rock fractures are often the result of normal and shear stresses that create void space between two rough surfaces (NRC, 1996). The point-wise separation between the two surfaces is termed local aperture (Oron and Berkowitz, 1998).

For the effective-dipole method, we assume that a fracture is composed of a collection of parallel plates. Each parallel plate has a unique aperture a and represents one dipole element on which the thin-bed reflection coefficients, eq. (3.3), apply locally. Since eq. (3.3) is also valid for apertures above the thin-bed criterion, it can be used to model reflections from a fracture with apertures both above and below $\frac{3\lambda}{4}$. Furthermore, changes in the polarity of the incoming electric field (e.g., due to the varying separation from the source or due to the

antenna radiation pattern) imply that reflections from apertures above and below $\frac{3\lambda}{4}$ may interfere both constructively and destructively. In practice, however, the fracture aperture is almost always well below the thin-bed criterion (typically by one or two orders of magnitude).
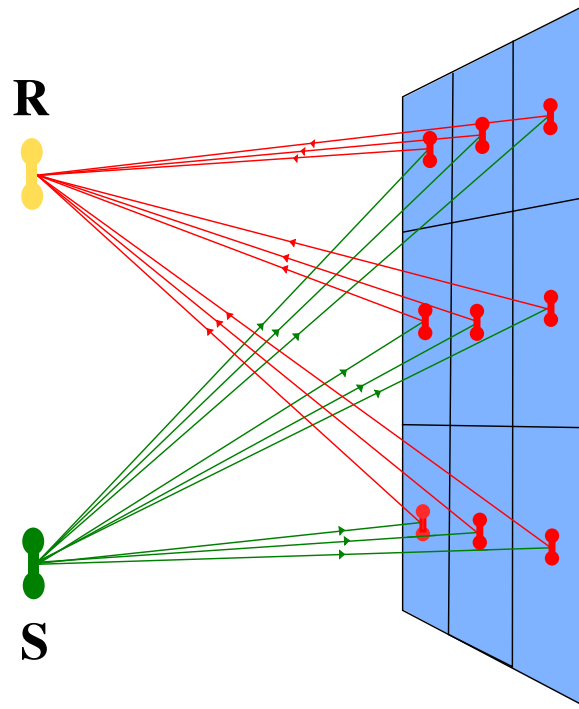
Figure 3.3 – Schematic of the effective-dipole forward modeling framework. A fracture is discretized into elements, and each element receives energy (green) directly from the source (S) and radiates (red) back to the receiver (R).

Self-affine aperture distributions

Local aperture variations are typically strong (e.g., Adler and Thovert, 1999, Ch. 4) and often exhibit statistically similar patterns over several scales (Bonnet et al., 2001). Such patterns can be reproduced mathematically by self-affine functions (Mandelbrot, 1982) and can be numerically computed using the power spectrum approach, that is based on taking the Fourier transform of a 2D Gaussian random field. In the following we use the algorithm by Adler and Thovert (1999) to generate a correlated random field (see their sec. 2.3.2 for details) using the following autocorrelation function:

$$C_h(u) = \sigma_h^2 \exp\left[-\left(\frac{u}{l_c}\right)^{2H} \right], \tag{3.4}$$

with input parameters being the variance σ_h, the cutoff length l_c and the Hurst exponent H. The cutoff length is the characteristic length over which correlations disappear and the

Hurst exponent, that varies over the range $0 \leq H \leq 1$, is related to the fractal dimension (*FD*) through $FD = 3 - H$ (Shepard et al., 1995).

Dipole coupling

Our effective-dipole forward model (Shakas and Linde, 2015) is based on an analogy to the microscopic analysis of Maxwell's equations (e.g., Purcell, 2011, Ch. 10). From a microscopic viewpoint, the polarization of dielectrics is a result of the cumulative contribution of many discrete polarizable elements. These elements (electrons at the smallest scale) are primarily polarized by the incoming electromagnetic field from an external source. In Shakas and Linde (2015), we upscaled the microscopic treatment to model propagation and scattering of GPR from fractures. We accomplished this by discretizing a fracture into dipole elements, where each element acts as a secondary source that is polarized by the GPR source (see Fig. 3.3).

Apart from energy from the source, each dipole element also receives energy from all the other elements (dipole coupling). When a fracture is planar (no topography), all dipole elements have the same orientation. This implies that the electric field always propagates perpendicularly between elements of the same fracture. A close look at eq. (3.3) reveals that when $\theta = \frac{\pi}{2}$ (i.e., perpendicular propagation), the exponential term reduces to unity and the thin-bed reflection coefficient reduces to zero. Therefore, for a planar fracture there is no contribution from dipole coupling. When fracture topography and/or multiple fractures are present, dipole coupling must be taken into account and this increases the computation time of our effective-dipole method. In this study, we consider only individual and planar fractures.

GPR response of a fracture with a heterogeneous conductivity distribution

In hydrogeophysical applications, GPR has been used to monitor electrically conductive tracer tests in fractured rock (e.g., Lane, Buursink, Haeni, and Versteeg, 2000; Tsoflias, Halihan, and Sharp, 2001; Talley, Baker, Becker, and Beyrle, 2005; Tsoflias and Becker, 2008; Dorn, Linde, Le Borgne, Bour, and Baron, 2011; Shakas, Linde, Baron, Bochet, Bour, and Le Borgne, 2016). Due to the non-linear nature of flow and transport in fractures, the resulting tracer distribution will be highly heterogeneous. On this basis, we create a test-case to ensure that the simulations based on our effective-dipole method are in agreement with FDTD simulations (gprMax3D, Warren, Giannopoulos, and Giannakis, 2015).

In a realistic fracture, an increase in aperture would directly (by an increase in the overall conductance) and indirectly (by governing the transport of the electrically conductive tracer) affect the GPR response. However, in order to adequately capture the effect of aperture variations, the discretization in FDTD simulations must be several times smaller than the smallest fracture aperture. This makes it difficult to accurately model aperture variations with FDTD and instead, we choose to keep the aperture constant and only vary the electrical conductivity.

We define a 10 m × 10 m × 10 m modeling domain with a discretization step of 1 cm. Within this domain, we define an 8 m × 8 m square fracture with an aperture of 10 cm, to allow for FDTD simulations with at least 10 nodes within the fracture. Along the fracture plane we

assign the electrical conductivity distribution using the autocorrelation function in eq. (3.4) with $\sigma_h = 0.025$, $l_c = 1$ and $H = 0.5$. The mean conductivity is $\sigma = 0.05$ S/m (schematic in Fig. 3.4(A) and the relative electric permittivity $\varepsilon_r = 21$, which results in a dominant wavelength of 65 cm within the fracture, thus making the fracture a thin-bed. As a source, we use a Ricker wavelet centered at 100 MHz that is emitted by a vertically-oriented infinitesimal dipole. To obtain a comparable source wavelet to the one in gprMax3D, we model the propagation to the first receiver (from S to R1) and run a local optimization search to find the best fitting source parameters.

We present the effective-dipole and gprMax3D simulation results in Fig. 3.4(B). Note that gprMax3D works in the time-domain and the effective-dipole method in the frequency domain. Therefore, Inverse Fourier-transformed traces are shown in the latter case. The excellent agreement between the two different approaches confirms that the heterogeneous fracture is modeled well with the effective-dipole method and it confirms that dipole coupling does not contribute to the response for planar and individual fractures.

3.4. Estimation of fracture aperture

Except for an unknown fracture aperture, we consider an idealized case for which all other fracture parameters are known, namely, the exact form of the source wavelet, the electric properties of both the rock matrix and the fracture filling as well as the orientation and position of the fracture. In this case it is straightforward to estimate an effective apparent aperture using GPR measurements for at least two source-receiver offsets.

3.4.1. Synthetic data creation

In both the homogeneous and heterogeneous fracture simulations that follow, the synthetic GPR data are created using the effective-dipole method. Since both the effective-dipole and thin-bed forward models are formulated in the frequency domain, we choose to treat the data, for inversion purposes, also in the frequency domain. For each fracture realization, the data consists of two traces that correspond to source-receiver offsets of $D = 0$ m and $D = 2$ m and with a constant separation between the fracture and antennas set to $S = 5$ m. The same vertically oriented source is used in all simulations. The source spectrum consists of a Ricker wavelet that is peaked at 100 MHz and we compute the reflected response in the range of $0 < f_n \leq 300$ MHz at a sampling rate of 1 MHz. Each resulting trace consists of 300 complex-valued numbers representing the returning electric field.

(A)

(B)
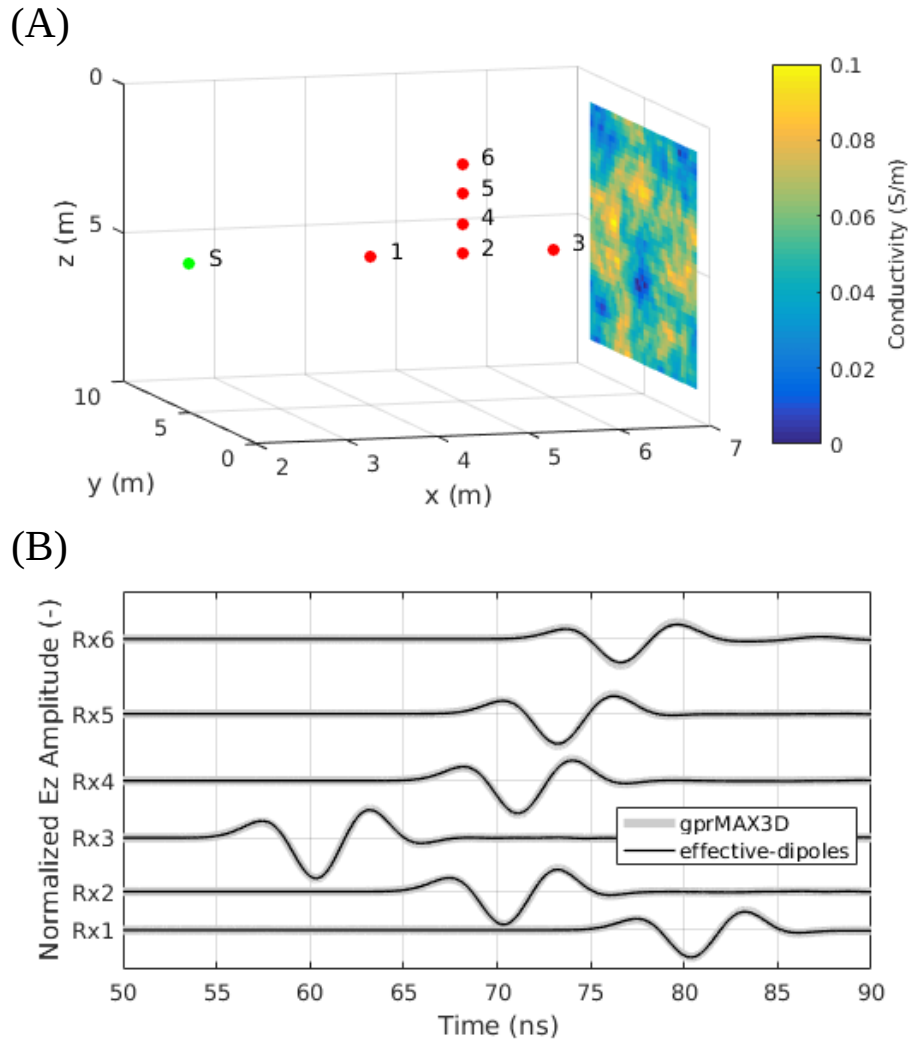
Figure 3.4 – (A) The model used to compare the effective-dipole modeling results with those obtained from 3D FDTD modeling for the case of a heterogeneous conductivity distribution. The source (S) is placed 5 m away from an 8 m × 8 m fracture with strong conductivity variations. The 6 receiver locations are also shown. (B) The simulation results from the model in (A) based on 3D FDTD (gprMax) and the effective-dipole method agree very well.

3.4.2. Amplitude scaling and noise-contamination

The thin-bed forward model computes the source-fracture-receiver interaction for a single path of the electromagnetic field, while the effective-dipole forward model computes it as an integral of many interactions on the finite fracture plane (compare Figs. 3.1 and 3.3). This leads to an amplitude discrepancy between the returning electric fields that are computed from the two methods. In practice, this limitation of the thin-bed approach can be avoided by taking GPR measurements with varying source-receiver offsets and considering the amplitude and phase variations as a function of offset. Therefore, with a minimum of two offsets we can compute relative amplitude-phase variations. In all the computations that follow, we

compute the largest (absolute value) amplitude of the $D = 0$ reflection, $max(|E_z(\omega)|)$, and use it to scale the response for each offset and each frequency component individually. This gives, for both the thin-bed and effective-dipole forward models, responses for which the $D = 2$ m response is scaled relative to the $D = 0$ m response. We then contaminate each frequency component using Gaussian noise with standard deviation of 0.035 (3.5%) that we add separately to the real and imaginary parts. This amounts to 5% noise in the time-domain data and is representative of the noise level in high-quality field data (e.g., Shakas, Linde, Baron, Bochet, Bour, and Le Borgne, 2016, fixed antenna experiment).

3.4.3. Data inversion

In deterministic geophysical inversion of GPR data, the aim is often to minimize a data misfit function in order to derive the best-fitting fracture parameters that reproduce the observed data using the forward model (e.g., Grégoire and Hollender, 2004; Bradford and Deeds, 2006; Deparis and Garambois, 2008; Sassen and Everett, 2009). The test case we are considering (i.e., all parameters known except the aperture) is idealized and serves as a best-case scenario. This implies that any problems that appear in this setting will certainly be present in actual field situations.

The misfit function space can be complex, especially when the forward model is non-linear. In order to invert the noise-contaminated data for the best-fitting aperture, we use the golden search algorithm (Kiefer, 1953) with the weighted root mean square error (WRMSE) as misfit function:

$$WRMSE(d_i^{sim}, d_i^{obs}, sd) = \sqrt{\frac{1}{2N} \sum_i^N \frac{\Re\{d_i^{sim} - d_i^{obs}\}^2 + \Im\{d_i^{sim} - d_i^{obs}\}^2}{sd^2}} \qquad (3.5)$$

where d_i^{sim} is the simulated data and d_i^{obs} is the observed data with added independent and identically distributed (*iid*) Gaussian noise of standard deviation sd. The WRMSE is 1 when the average misfit between simulated and observed data corresponds to the predefined noise level. Our convergence criteria for the inversion are that (1) the WRMSE ≤ 1 or (2) the forward model is run more than 1500 times.

3.4.4. Fractures with a constant aperture

We use the golden-section search algorithm to find the best-fitting aperture given noise-contaminated data generated from the GPR response of a homogeneous fracture. Using the effective-dipole code, we create 40 datasets for fractures with constant aperture that varies logarithmically in the range 0.1 mm ≤ a ≤ 10 mm. Then, using both the thin-bed and effective-dipole forward models we run the inversion algorithm until one of the two criteria is met. In Fig. 3.5 we show the best-fit aperture along with the WRMSE for both forward models.
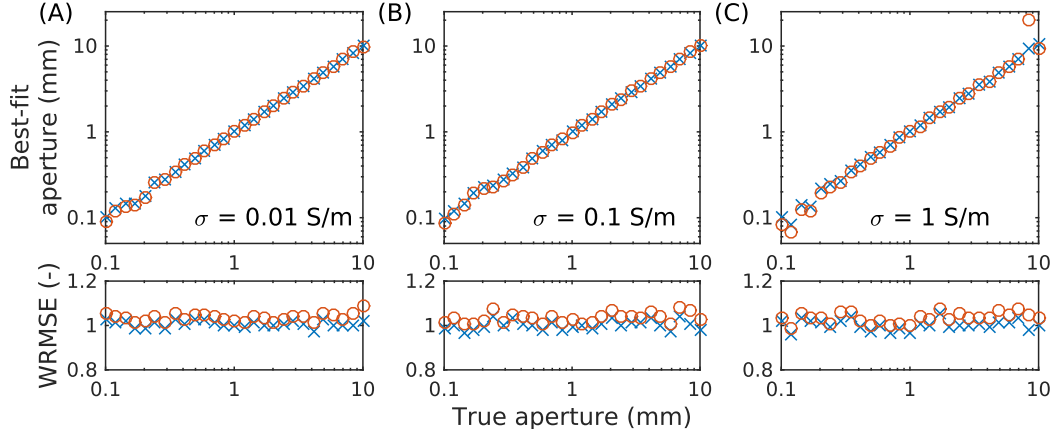
Figure 3.5 – Inversion results, along with corresponding WRMSE, for the best-fit aperture describing a homogeneous fracture. The inversions use noise-contaminated (observed) data generated using the effective-dipole model, and (simulated) forward responses from either the thin-bed (○) or the effective-dipole (×) models. Three fracture conductivities (σ) are considered for 40 fracture apertures in the logarithmically-spaced interval $0.1 \leq a \leq 10$ mm.

Considering three different fracture conductivities, we find that inversion results based on the thin-bed or effective-dipole forward models produce excellent aperture estimates, down to apertures of 0.3 mm.

3.4.5. Fractures with heterogeneous aperture variations

In nature, fractures exhibit variations in local aperture that will cause GPR reflections to differ from the theoretical thin-bed reflection of a homogeneous fracture. These apertures are often assumed to follow specific spatial patterns along the fracture plane. Here, we asses the impact of local aperture heterogeneity on the inferred thin-bed aperture.

Using the geostatistical algorithm by Adler and Thovert (1999), presented in section 3.3.3, we consider 16 classes of heterogeneity models describing local aperture. Each class is defined by a unique pair of the cutoff length and Hurst exponent, namely $H = \{0.25, 0.5, 0.75, 1\}$ and $l_c = \{0.5, 1, 2, 4\}$ m, and for each class we generate 1000 fracture realizations. Each fracture realization shares the same statistical properties, within each class, but is otherwise independent of other realizations within the class. We discretize the heterogeneous fractures using 10 elements per dominant wavelength, resulting in a spatial element discretization of 10 cm × 10 cm. All fractures share the same (arithmetic) mean aperture of 5 mm, variance of 1 mm and electrical conductivity $\sigma = 0.1$ S/m. One representative realization for each geostatistical class is shown in Fig. 3.6.

For each fracture realization we use the effective-dipole forward model to create noise-contaminated GPR (observed) data. Using the thin-bed forward model and the golden search inversion algorithm, we infer the best-fitting constant-aperture fracture that can reproduce the observed data. The histograms of the inferred apertures for each $\{H, l_c\}$ pair are plotted in Fig. 3.9 together with the marginal probability density function (pdf) of aperture for the

geostatistical models considered. The corresponding mean and variance of the WRMSE, for each geostatistical class, are shown in Table 3.1. For comparison purposes, we also tabulate the mean and variance of the WRMSE between the observed data and simulated data from a fracture with constant aperture of 5 mm (equivalent to the mean aperture of the 16 classes of geostatistical models).
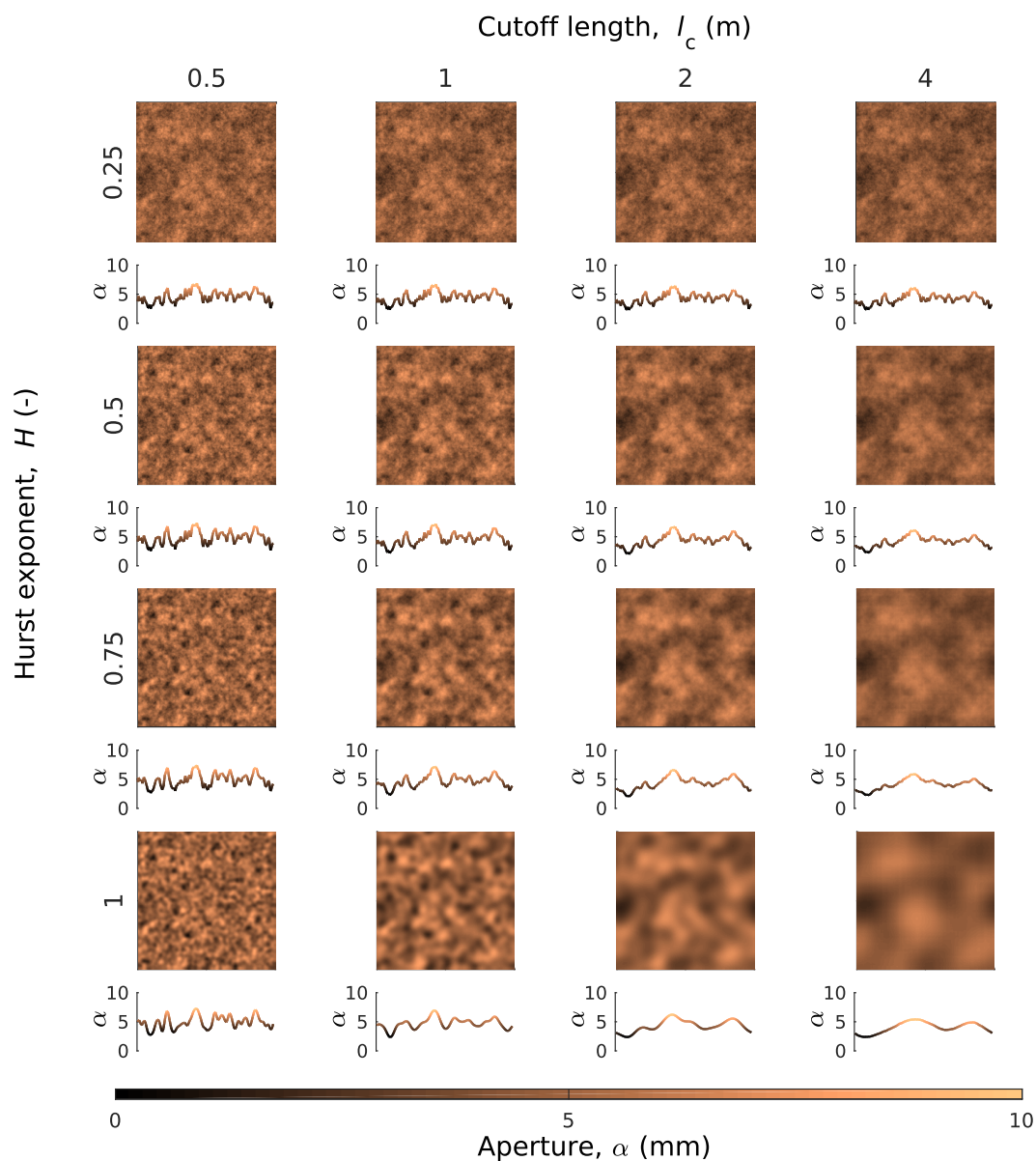
Figure 3.6 – Representative aperture (α) realizations for each of the 16 considered geostatistical heterogeneity classes. Each class is characterized by a different pair of Hurst exponent (H) and cutoff length (l_c). The mean aperture is 5 mm, the variance is 1 mm and the fracture size is 20 m × 20 m. Below each realization, the aperture profile along the horizontal line dissecting the middle of each fracture is shown.

Table 3.1 – {Mean, variance} of the WRMSE between simulated data, computed using the thin-bed forward model and assuming a homogeneous fracture with either (A) the best-fitting inferred aperture (see Fig. 3.9) or (B) a 5 mm aperture, and observed data computed using the effective-dipole forward model and considering a fracture with a heterogeneous aperture field (with arithmetic mean of 5 mm). In total, 16 classes of heterogeneity are generated by varying the Hurst exponent H and cutoff-length l_c.

	$l_c = 0.5$ m	$l_c = 1$ m	$l_c = 2$ m	$l_c = 4$ m
(A) Homogeneous fracture with best-fitting aperture				
$H = 0.25$	{1.103, 0.005}	{1.093, 0.004}	{1.080, 0.003}	{1.067, 0.003}
$H = 0.5$	{1.157, 0.010}	{1.109, 0.006}	{1.069, 0.003}	{1.045, 0.002}
$H = 0.75$	{1.189, 0.016}	{1.090, 0.005}	{1.043, 0.002}	{1.025, 0.001}
$H = 1$	{1.210, 0.024}	{1.064, 0.004}	{1.025, 0.001}	{1.016, 0.001}
(B) Homogeneous fracture with 5 mm aperture				
$H = 0.25$	{1.923, 0.123}	{1.917, 0.120}	{1.905, 0.108}	{1.893, 0.095}
$H = 0.5$	{1.981, 0.227}	{1.949, 0.210}	{1.912, 0.139}	{1.883, 0.084}
$H = 0.75$	{2.013, 0.285}	{1.958, 0.296}	{1.899, 0.120}	{1.865, 0.047}
$H = 1$	{2.033, 0.313}	{1.957, 0.370}	{1.889, 0.076}	{1.856, 0.018}

3.4.6. GPR resolution and weighted apertures

Considering the same source-receiver and fracture geometry as in Fig. 3.3, we can define (1) the radial resolution as the smallest aperture and (2) the lateral resolution as the smallest feature along the fracture plane that can be reliably inferred by the GPR data (e.g., Jol, 2008, sec. 1.3.4).

In a water-saturated fractured rock system it is possible to obtain very high radial resolution because of the strong contrast between electrical parameters in the rock matrix and fracture filling. For example, our inversion results for the homogeneous fracture (Fig. 3.5) suggest that we can reliably infer apertures down to roughly 0.3 mm with a signal whose dominant wavelength is 1 m.

Lateral resolution of GPR data is often discussed in terms of the Fresnel zone (Pearce and Mittleman, 2002) and it is used to approximate the smallest detectable target for a given acquisition geometry and signal bandwidth. The Fresnel zone is derived by considering a wave with normal incidence to a reflecting surface. Moving away from this point of incidence, the first Fresnel zone radius is constructed by computing the separation at which another incident wave (from the same source) is reflected with a phase shift $\Delta\phi \le \pi$. For the acquisition geometry we consider here, and a signal with dominant wavelength of 1 m in the background matrix, the resulting Fresnel zone radius is 1.6 m. However, this does not provide information about the relative contribution to the measured signal within this radius.

Instead of using the Fresnel zone, we describe here the lateral resolution by considering the individual response of each discretized element for a homogeneous fracture. Using the same source and acquisition geometry as above, we generate a fracture discretized by 10 cm × 10 cm elements with $\sigma = 0.1$ S/m and $a = 5$ mm. We then compute, for each of the two

source-receiver pairs, the returning (vertical) electric field from each element. This amounts to a complex-valued contribution, for each sampled frequency, that represents the amplitude and phase of the electric field from each element. Next, we sum the complex-valued response over all frequencies. We do this for each element and source-receiver offset separately. This provides two complex-valued numbers for each element (one for each source-receiver offset). We then take the absolute value of the pair above and sum the two values. The result is a real-valued number per element that provides us a distribution of weights along the fracture plane. Finally, we scale the weight distribution such that it integrates to 1. The final weights are shown in Fig. 3.10 along with the first Fresnel zone.

These weights allow us to compute a mean aperture for each fracture realization over a spatial scale that corresponds well to the first Fresnel zone. As an example, in Fig. 3.7 we show the application of the weights to the fracture realization presented in Fig. 3.6. However, this averaging is built on the assumption that the apertures influence the GPR data linearly and does not always correspond to the best-fitting inferred aperture. In Fig. 3.8 we show, for each $\{H, l_c\}$ combination, a scatter plot of the inferred versus weighted aperture pairs. In most cases, the agreement is very poor.

3.5. Discussion

The thin-bed forward model can serve as a reliable simulator of the GPR response from a homogeneous fracture that is large enough to be considered 'infinite'. The inversion results (Fig. 3.5) suggest that the thin-bed and effective-dipole forward models work equally well in retrieving the (constant) aperture. Reliable estimates are obtained over a wide aperture range, down to apertures that are more than three orders of magnitude smaller than the dominant wavelength of the GPR source.

Natural fractures result from complex processes and are (most probably) never homogeneous. The primary objective of this study was to understand the influence of small-scale aperture heterogeneity on the inferred thin-bed aperture. We accomplish this by defining 16 classes of geostatistical models, and creating 1000 fracture realizations within each class. We then use our effective-dipole forward model to create noise-contaminated datasets, and use the thin-bed forward model to infer a corresponding homogeneous fracture that best fits each dataset. If the GPR response would only be a linear average of the actual apertures over the Fresnel zone, then the inferred apertures should show significantly less variability than the marginal pdf of the geostatistical models. Our results suggest that this is not the case (see Fig. 3.9) and only when the cutoff length l_c is large (i.e., as aperture patterns become larger) does the histogram of inferred apertures approach the marginal pdf of the actual local apertures. This convergence is intuitive because as the size of patterns increase, the realizations approach the case of a homogeneous-aperture fracture. Furthermore, the Hurst exponent H also plays an important role. Small H suggests more fractal behavior, resulting in similar aperture patterns appearing at all spatial scales. The inferred aperture distributions for small H (first row in Fig. 3.9) show a very similar pattern, regardless of changes in l_c.
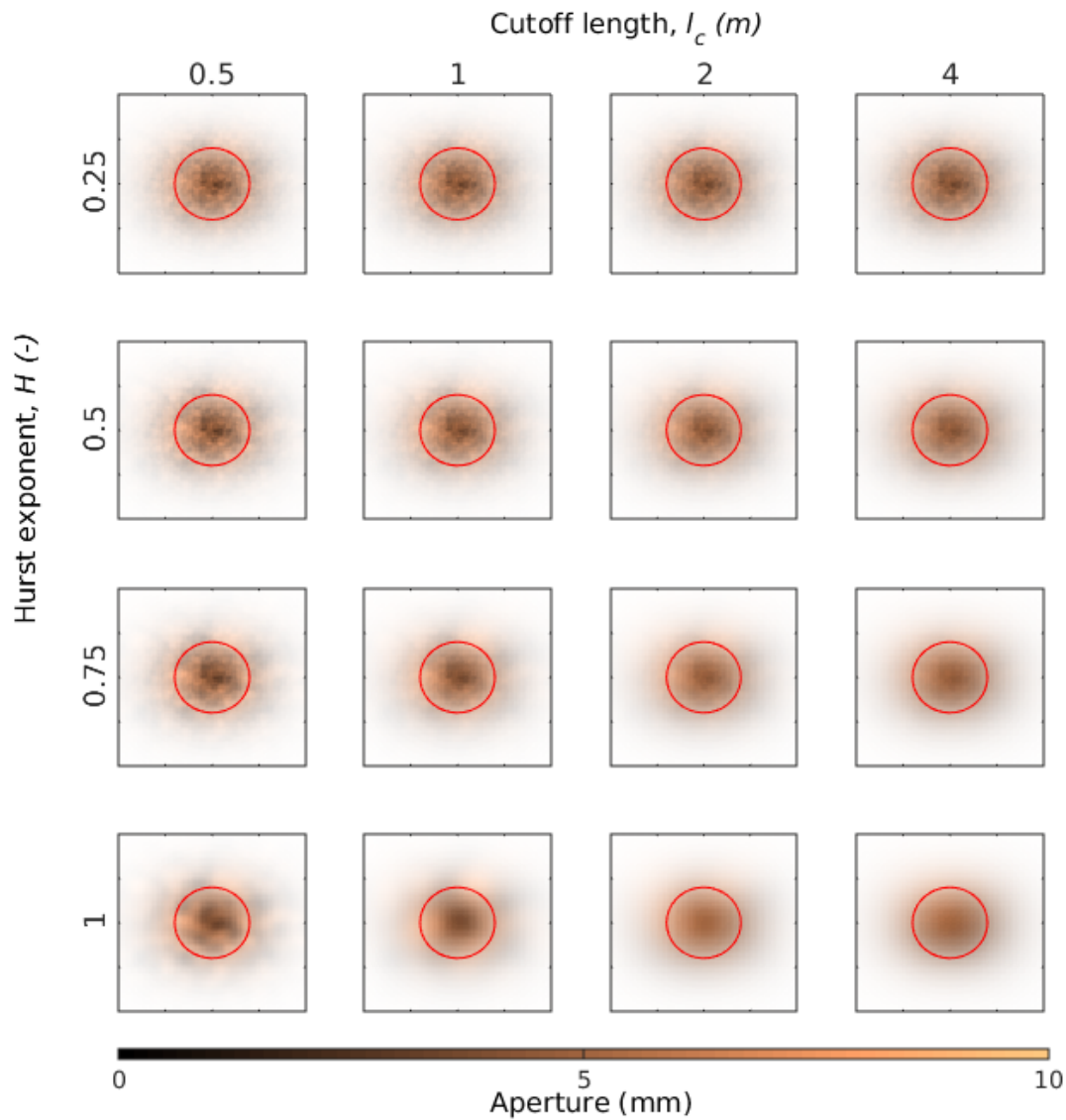
Figure 3.7 – The averaging process implied by the linear weights in Fig. 3.10 is illustrated for the same fracture realizations as in Fig. 3.6. The opacity is complete for elements with negligible weight and the opacity is decreased linearly to zero for the elements with the highest sensitivity. The first Fresnel zone is shown by a red solid line. For better visualization, only the central 8 m × 8 m section of the full 20 m × 20 m fractures is shown.

The fact that the inferred apertures are much wider than the marginal pdf of the actual (geometric) apertures for cases when l_c and/or H are small, suggests that the inferred GPR aperture is not a good proxy of the geometric aperture. In fact, the inferred GPR aperture should be considered as an apparent aperture. The situation is similar in other branches of geophysics. For example, in electrical resistivity tomography it is possible to obtain negative apparent resistivities, even if electrical resistivity can never be negative. These effects are manifestations of non-linearity and imply that apparent properties might be difficult to translate into actual properties. Table 1 also highlights that the derived apparent apertures
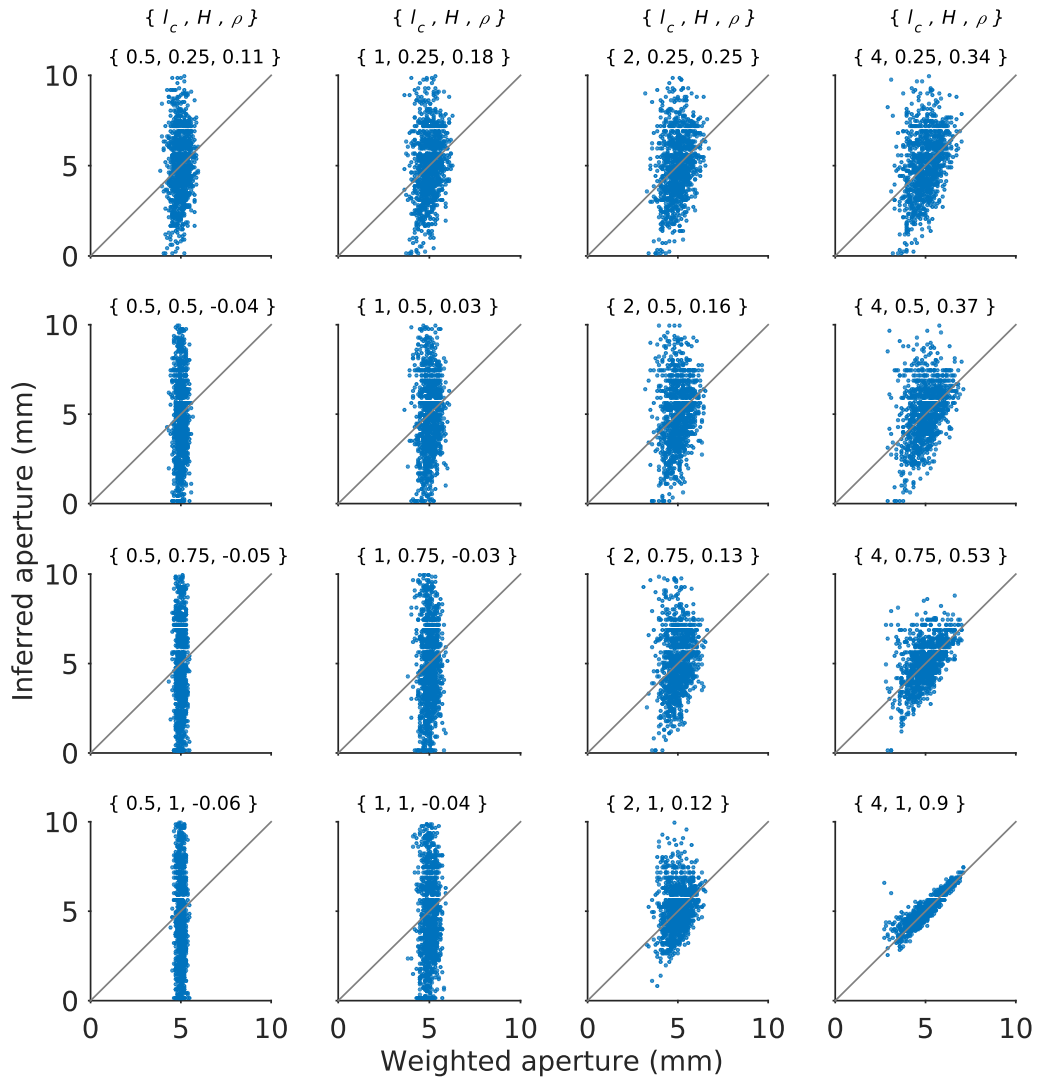
Figure 3.8 – For each of the 16 classes of geostatistical models, scatter plots of the inferred (apparent) versus the weighted (mean) aperture for 1000 fracture realizations. The linear trend is plotted with a diagonal line and the Hurst exponent H, cutoff-length l_c and correlation coefficient ρ is given for each plot.

explain the data well (WRMSE slightly higher than 1) while simulations based on the constant aperture of 5 mm fit the data poorly (WRMSE around 2).

To better understand to what extent the data can be seen as a linear spatial averaging process, we derive weights based on the complex-valued returning electric field from each fracture element (local aperture). This is done for a fracture with a constant aperture that equals the mean aperture of the geostatistical models. The resulting weights (see Fig. 3.10) are significant within the first Fresnel zone. We use these weights to compute a weighted aperture for each fracture realization (Fig. 3.7). In contrast, the apparent aperture is obtained from the homogeneous fracture that can best reproduce the data through the thin-bed forward model. The comparison between the derived weighted aperture and the apparent aperture (Fig. 3.8)
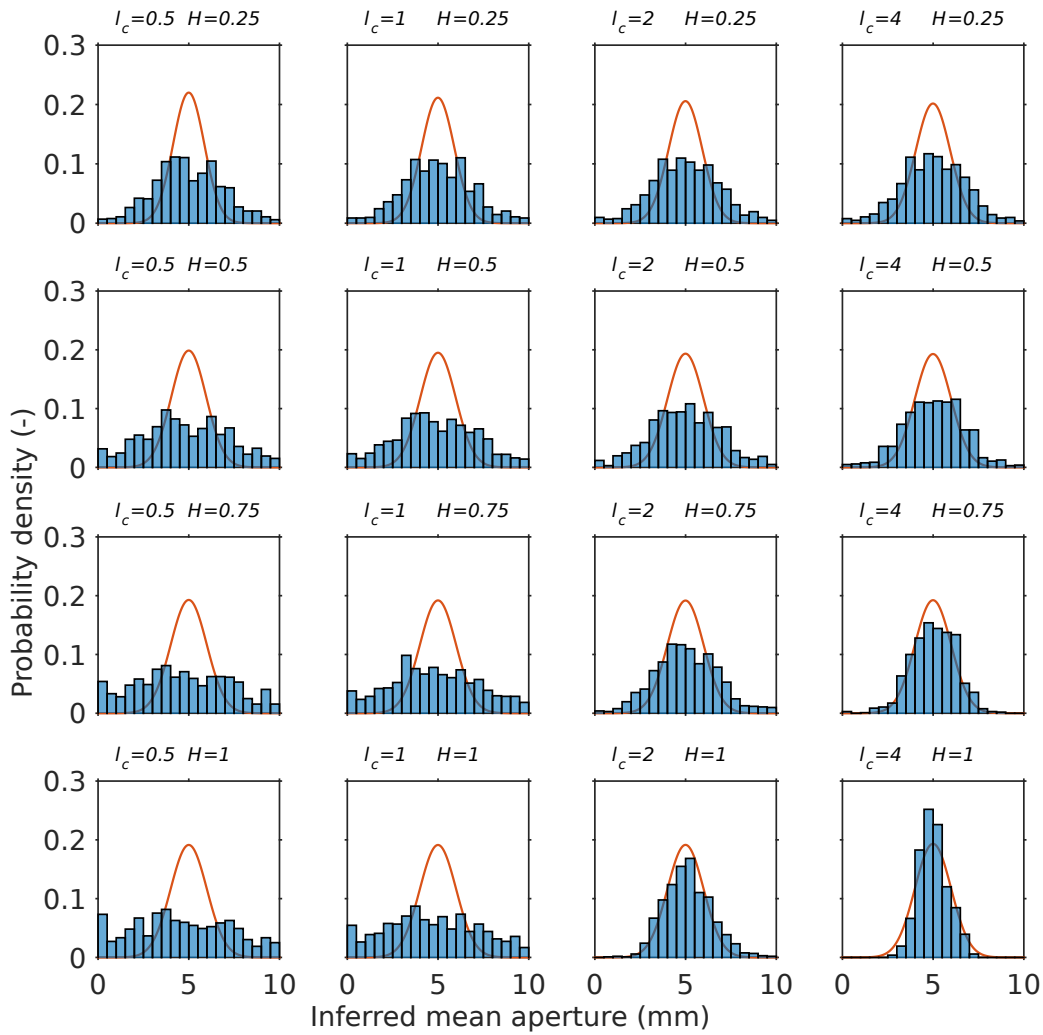
Figure 3.9 – Probability density histograms of the best-fitting homogeneous fracture aper-
tures (1000 realizations for each class). For each class of heterogeneity model, the marginal
probability density function of aperture is the same (solid red line). The corresponding mean
and standard deviation of the WRMSE, for each class, is shown in Table 3.1.

suggests that when the cutoff length is small, the apparent aperture does not correspond well
to the weighted aperture (first column). While the apparent aperture prediction approaches
the linear estimate as the cutoff length is increased, good correspondence of the two apertures
is only obtained when both l_c and H are large, as in the pair $\{H, l_c\} = \{1, 4 \text{ m}\}$.
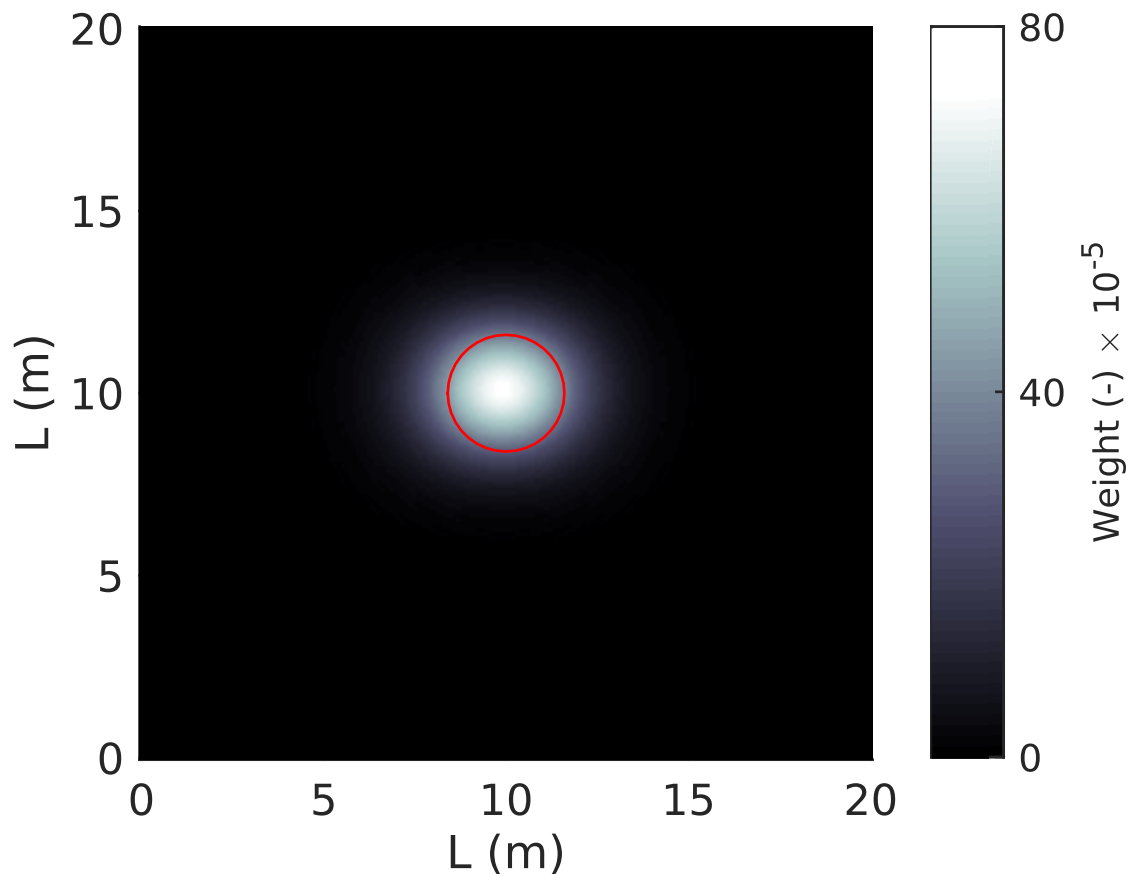
Figure 3.10 – Weights derived from the sensitivity of the effective-dipole forward model, for a homogeneous fracture. Fracture aperture is $a = 5$ mm and conductivity is $\sigma = 0.1$ S/m, respectively. Acquisition parameters are $S = 5$ m, $D = 0$ m and $D = 2$ m and $L = 20$ m (see Fig. 3.1). The first Fresnel zone is indicated by a red solid line.

3.6. Conclusions

For an idealized experimental set-up, we have used the GPR thin-bed forward model to infer an apparent fracture aperture. When data are generated from a homogeneous (constant-aperture) fracture model, the apparent aperture corresponds well with the actual fracture aperture, However, when aperture heterogeneities are present, the apparent aperture that is derived under the assumption of a homogeneous fracture does not always provide satisfying results. Namely, when a small cutoff length (aperture heterogeneity patterns are small) and Hurst exponent (heterogeneity present at all scales) is used to generate aperture fields, the apparent aperture can be very different from the mean aperture averaged over the first Fresnel zone. When aperture variations are non-fractal ($H = 1$) and the aperture patterns are large ($l_c = 4$ m) compared to the signal dominant wavelength (1 m), the apparent aperture can be a good estimate of the Fresnel-based linear average of fracture aperture.

Our results suggest that GPR-derived estimates of fracture aperture, that are based on the common assumption of constant aperture, should be treated with caution, especially when strong aperture heterogeneity is present. Under the homogeneous assumption, inferred apertures serve as an apparent estimate that has a complex and non-linear relation to the actual geometrical fracture aperture. To reliably interpret GPR data generated by a heterogeneous fracture, a more encompassing modeling framework must be considered, that explicitly accounts for aperture heterogeneity. In future work, we plan to use model selection tools to determine the geostatistical model that best corresponds to GPR reflection data from heterogeneous fractures.

Chapter 4

Hydrogeophysical characterization of transport processes in fractured rock by combining push-pull and single-hole ground penetrating radar experiments

Alexis Shakas, Niklas Linde, Ludovic Baron, Olivier Bochet, Olivier Bour and Tanguy Le Borgne.

4.1. Abstract

The in situ characterization of transport processes in fractured media is particularly challenging due to the considerable spatial uncertainty on tracer pathways and dominant controlling processes, such as dispersion, channeling, trapping, matrix diffusion, ambient and density driven flows. We attempted to reduce this uncertainty by coupling push-pull tracer experiments with single-hole ground penetrating radar (GPR) time-lapse imaging. The experiments involved different injection fractures, chaser volumes and resting times, and were performed at the fractured rock research site of Ploemeur in France (H^+) network, hplus.ore.fr/en). For the GPR acquisitions we used both fixed and moving antenna setups in a borehole that was isolated with a flexible liner. During the fixed-antenna experiment, time-varying GPR reflections allowed us to track the spatial and temporal dynamics of the tracer during the push-pull experiment. During the moving antenna experiments, we clearly imaged the dominant fractures in which tracer transport took place, fractures in which the tracer was trapped for longer time periods and the spatial extent of the tracer distribution (up to 8 meters) at different times. This demonstrated the existence of strongly channelized flow in the first few meters and radial flow at greater distances. By varying the resting time of a given experiment, we identified regions affected by density-driven and ambient flow. These experiments open up new perspectives for coupled hydrogeophysical inversion aimed at understanding transport phenomena in fractured rock formations.

4.2. Introduction

Characterization of flow and transport in fractured rock formations has been a central focus of hydrogeological research for several decades (e.g., NRC, 1996). The interest arises from a multitude of applications, ranging from environmental remediation (e.g., Andričević and Cvetković, 1996) to safe disposal of nuclear waste (e.g., Cvetković et al., 2004). Experimental studies over several scales is essential to constrain site-specific conceptual models (Le Borgne et al., 2006) that can be used for numerical simulations of flow and transport for purposes of predictions, risk-assessment and decision making (Berkowitz, 2002).

Fractured geological media are often assumed to be scale-invariant and power-law distributions have been successfully used to statistically describe scaling properties in terms of length or aperture (Bonnet et al., 2001). The resulting flow heterogeneity is characterized by strong channeling at both fracture and network scales, which implies that advection occurs mainly through preferential paths. This directly affects transport processes that display strongly non-Fickian dispersion behavior, including early tracer breakthrough and late time tailing, as observed in tracer test experiments (Haggerty et al., 2000; Becker and Shapiro, 2003; Berkowitz, 2002). The physical interpretation of these observations is often ambiguous as different physical processes, for example, diffusive trapping into a low velocity zone or advection into variable velocity channels, may cause similar tailing behavior in tracer breakthrough curves (Kang et al., 2015). This motivates the development of geophysical approaches that

enable observing the motion and spatial distribution of tracers in situ. This is the focus of the present study.

The complexity of tracer pathways in fractured systems implies that tracer recovery, in classical cross-borehole tests, decays fast as the distance between injection and observation wells is increased. On the other hand, push-pull experiments (Istok, 2012)—also called single-well injection withdrawal experiments—with their higher tracer retrieval offer a time and cost-effective method for obtaining information about transport properties of fractured rock formations (Nordqvist and Gustafsson, 2002). Push-pull experiments are carried out by packing-off a fractured section of the borehole using a dual-packer system and injecting (pushing) a tracer (or multiple tracers) into the fractured system through the packed-off interval (injection interval). After pushing the tracer into the system, a chaser fluid is used to clean the injection chamber and to push the tracer further out into the formation. The chaser fluid is usually water at ambient aquifer conditions and the volume of chaser injected varies depending on the scale of investigation. During the pulling period the flow is reversed to produce a tracer breakthrough curve.

The expected reversibility of advective transport in push-pull experiments implies that the recorded tracer breakthrough curve is only weakly sensitive to the transmissivity distribution of the fractured rock formation, and that the mean arrival time of the tracer breakthrough curve is uninformative (Becker and Shapiro, 2003). Indeed, push-pull experiments are mainly sensitive to irreversible time-dependent processes (Nordqvist and Gustafsson, 2002; Kang et al., 2015) such as sorption and diffusion. It is possible to increase the sensitivity of push-pull experiments to these processes by introducing a resting time between the pushing and pulling phases (Berkowitz, 2002). Multiple push-pull tests with varying pushing and/or chasing volumes make it possible to engage different volumes of the system and gain scale-dependent information (Gouze et al., 2008). The results can be compared to analytical or numerical solutions, thus allowing inference about flow and transport properties of the system (Becker and Shapiro, 2003; Le Borgne and Gouze, 2008).

Geophysics offers high resolution and high spatial coverage data that complement the information obtained by hydrological experiments (e.g., Hubbard and Linde, 2011, Ch.2.15). For instance, ground penetrating radar (GPR) reflection imaging makes it possible to image dynamic processes and associated length scales of hydrogeological experiments in fractured rock formations, particularly when tracers with sufficient contrast in electrical conductivity are used, such as saline tracers (Tsoflias and Becker, 2008). The unique ability of GPR reflection imaging to remotely detect fractures of millimeter-thin aperture has been rigorously investigated in both laboratory (e.g., Grégoire and Hollender, 2004) and field-based conditions (e.g., Dorn et al., 2012). Recently, surface (Becker and Tsoflias, 2010), cross-well (Day-Lewis et al., 2003) and single-well (Dorn et al., 2012) GPR have been used in conjunction with dipole saline tracer experiments, not only to dynamically image the migration of tracer movement between boreholes but also to condition discrete fracture network (DFN) models (Dorn et al., 2013).

DFN models are conceptual models used to describe fractured rock formations, where flow and transport only occurs inside fractures (e.g., de Dreuzy et al., 2012). This approximation is particularly suitable for crystalline rock formations (e.g., Nordqvist and Gustafsson, 2002). To

adequately condition DFN models it is necessary to describe the physical properties of the fractures at both the single fracture and the fracture network scales (de Dreuzy et al., 2012). For a single fracture this description can include the mean aperture, fracture orientation and fracture length. It is practically impossible to gain independent information on these properties through push-pull tests alone since the length scale over which the tracer is transported is unknown and fracture orientation is only known at the borehole location. Moreover, the effect of ambient flow and the buoyancy effect of tracers with a significant density contrast with respect to the formation water, are usually ignored when interpreting push-pull data.

To address the inherent ambiguity in interpreting push-pull tests alone, we conducted a series of combined push-pull and single-hole GPR experiments in a crystalline aquifer. We performed repeated push-pull experiments with varying resting times and chasing volumes and monitored the GPR response with both fixed and moving antenna configurations. In this contribution we investigate how GPR monitoring of push-pull experiments can provide constrains on flow and transport characteristics of the fractured system.

4.3. Field Site and Experimental Setup

The experiments were carried out between the 19th and 26th of June 2014 at the Ploemeur fracture rock experimental site in Brittany, France (H^+ network of experimental sites). Previously acquired data at this well-studied site, such as optical, acoustic and geological logs can be found in the H+ observatory database (http://hplus.ore.fr/en). The aquifer supplies drinking water to the town of Ploemeur (20,000 inhabitants) and it is mainly composed of granite and mica schists (Ruelleu et al., 2010). At the borehole scale, only a few fractures dominate the hydraulic behavior of this highly transmissive aquifer (the average transmissivity at site scale is around T = $10^{-3} m^2/s$ (Le Borgne et al., 2004, 2006). Borehole GPR data have been previously acquired at the experimental site named Stang-Er-Brune that is located 3 km west of the water supply wells (Le Borgne et al., 2007; Dorn et al., 2011, 2012; Kang et al., 2015). To the best of our knowledge, this is the first time that push-pull tests and single-hole GPR are combined in a field experiment.

A series of cross-borehole and push pull tracer tests were previously performed with fluorescent dyes on this site (Kang et al., 2015). Breakthrough curve tailing was found to be characterized by power law behaviors, c(t) $\sim t^{1-b}$ at late times, with b ranging from 0.75 to 1. The tailing exponents were systematically larger (which implies that tailing was less significant) under push pull conditions than under cross-borehole conditions. This implies that matrix diffusion is not expected to be significant in this low permeability granite and that the dispersion behavior measured from the fluorescent dye experiments was mostly controlled by dispersion in fracture planes, as observed in the similar geological setup at the Mirror Lake site (Becker and Shapiro, 2003).

The injection (B1) and monitoring (B2) boreholes are separated on average by 6 m. We conducted push-pull experiments in B1 while we performed single-hole GPR monitoring in

Table 4.1 – Experimental parameters for: (a) push-pull and (b) push-wait-pull with wethanalt, (c) push-pull and (d) push-wait-pull with a saline tracer and (e) the fluorescein-based push-pull experiment by Kang et al. (2015).

Experiment	I	II	III	IV	V
Injection depth [m]	78.7	78.7	50.9	78.7	78.7
Monitoring depth [m]	75.1	50-90	30-60	50-90	50-90
GPR Antennas	Fixed	Moving	Moving	Moving	Moving
Tracer density [$kg \cdot m^{-3}$]	1044	1044	1044	1042	1041
Salinity [$g \cdot kg^{-1}$]	44	44	44	42	41
Tracer volume [L]	100	100	100	100	100
Chaser volume [L]	90	90	100	90	710
Resting time [hh:mm]	00:00	00:00	04:45	03:47	00:00
Pumping rate[$L \cdot min^{-1}$]	3.2	3.2	3.3	3.3	3.3
Mass recovery (%)	55	51	79	40	27

B2. In contrast to previous single-hole GPR acquisitions (e.g., Dorn et al., 2012) we used a flexible liner (blank flexible liner by FLUTe) to seal-off the GPR monitoring borehole from the aquifer. The liner was filled with formation water, extended to the bottom of the borehole and allowed smooth movement of the GPR antennas while preventing conductive tracer from entering the borehole and thereby affecting the effective GPR antenna signal (see Dorn et al. (2011, 2012)). This also minimized the propagation of pressure variations arising from the antenna movement to the surroundings. A schematic description of the experimental setup is shown in 4.1.

We present five push-pull tests with injections at either 50.9 m or 78.7 m (see Table 4.1). We focus the analysis on experiments I, II and III; experiments IV and V are only used herein assess the repeatability of our results. Previous studies by Le Borgne et al. (2007) and Dorn et al. (2012, 2013) concluded that the fracture at 50.9 m in B1 connects to low-permeable, sub-horizontal fractures while the fracture at 78.7 m connects to transmissive, sub-vertically oriented fractures. These fractures were interpreted to be of the order of ~10 m in length and to have apertures in the millimeter to sub-millimeter range. We used a custom-made double-packer in B1 to seal off the injection interval during the push-pull experiments (Figure 4.1). The double-packer consisted of two inflatable packers separated by 0.6 m, which were inflated to firmly adhere on the borehole wall. We monitored and manually controlled the pumping rate with a flowmeter and pump (MP1 by Grundfos) installed above the double packer, while we measured the electrical conductivity, temperature and pressure in the injection interval using a CTD diver by Schlumberger. Halfway through each saline tracer injection we injected an additional fluorescent conservative tracer that had the same salinity as the formation water. In the present study we focus on the joint analysis of GPR and saline tracer breakthrough curve data.

For the GPR acquisitions we used the RAMAC 100 MHz system with slim-hole borehole antennas, manufactured by MALÅ. In all experiments we used a fixed separation of 4 m between the midpoints of the transmitter and receiver antennas. We centered the antennas in the borehole by using custom-made flexible centralizers that we attached to the top
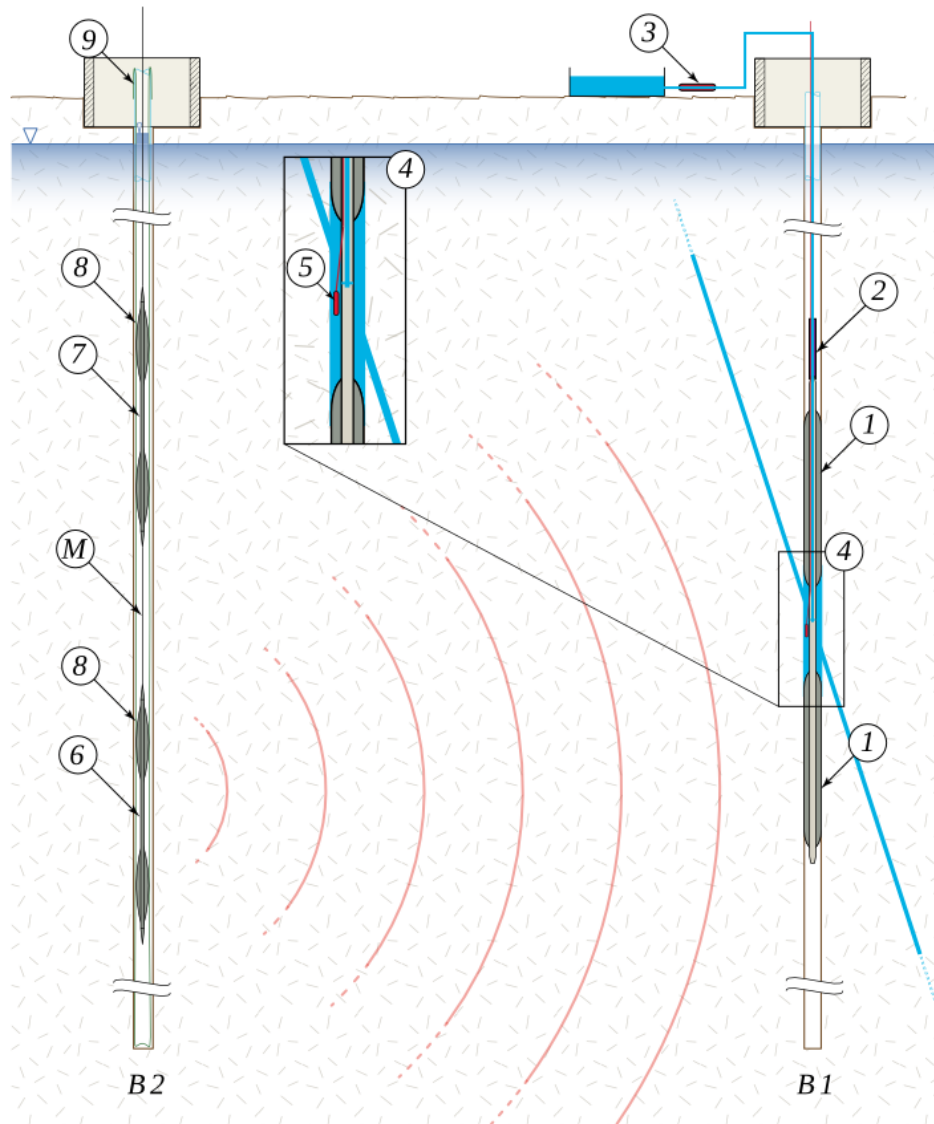
Figure 4.1 – Schematic description of the combined push-pull experiment in borehole B1 and single-hole GPR monitoring in borehole B2 (not to scale). In B1, a section of the borehole is isolated using two inflatable packers (1) while a pump (2) and a flowmeter (3) are used to control the pushing and pulling of saline tracer in the injection interval (4). A CTD diver (5) measures the electrical conductivity, temperature and hydraulic pressure in the chamber. In B2, GPR monitoring takes place with the transmitter (6) and receiver (7) antennas, which have a fixed separation with midpoint M and are centered in the borehole using custom-made centralizers (8). B2 is hydraulically isolated from the surroundings by a flexible borehole liner (9).

and bottom of each antenna (Figure 4.1). The use of centralizers and a flexible liner made the GPR acquisition very smooth and the estimated positioning errors during the moving antenna experiments were minor (standard deviation of 8 mm). During the moving antenna experiments we acquired data with a spatial sampling rate of 5 cm along the borehole. For the moving antenna experiment, we sampled at 1148 MHz for a time-window of 450 ns,

and used 64 stacks per trace to increase the signal-to-noise ratio. For the fixed antenna experiment, we used a sampling rate of 4278 MHz and 128 stacks per trace. While GPR reflections contain information about the fracture aperture at the mm scale (Dorn et al., 2011), the spatial resolution along the fracture plane (based on the Fresnel zone) is roughly 1 m for the 100 MHz antennas we used and the distances we investigate (e.g., Jol, 2008, sec. 1.3.4). After the processing of the moving antenna experiments, the resolution is refined to roughly a quarter of the wavelength (i.e., 0.25 mm). Both types of acquisition (fixed and moving antenna) resulted in data with very high signal-to-noise ratios that required minimal processing.

4.4. GPR Data Processing Steps

In this section, we describe the processing steps that were applied to the raw single-hole GPR data. We begin with the basic concept of single-hole GPR and continue to analyze each processing step (see Jol (2008) for a more detailed description of GPR theory and processing).

4.4.1. Basic concepts of borehole GPR

A dipole GPR transmitter antenna, as the one we used, generates an alternating high-frequency electric field. This field propagates symmetrically around the antenna axis but is the strongest in the plane that is perpendicular to the antenna and intersects the antenna midpoint (e.g., Jol, 2008, sec. 1.4).

The propagating field is attenuated and dispersed as it travels through the rock matrix and water-filled fractures. Reflections occur at rock-fracture interfaces due to the high contrast in electrical properties between the rock matrix and water. The strength of the reflections depends on fracture properties such as orientation, aperture and roughness. Within the water-filled fracture the electric field experiences strong attenuation and dispersion, which results in a decreased amplitude and a phase shift of the electric field. When the electrical properties of the fracture filling change, such as the change in electrical conductivity induced by the presence of a saline tracer, the magnitude and phase of the reflected electric field also change (Bradford and Deeds, 2006; Tsoflias and Becker, 2008).

The receiver antenna measures a voltage as a function of time (a GPR trace) that is proportional to the amplitude of the reflected electric field. If the GPR antennas are kept fixed at a specific depth along the borehole, changes in the reflected traces over time are indicative of salinity variations in the vicinity of the transmitter-receiver pair. These changes reflect the (averaged) temporal dynamics of the saline tracer in the region surrounding the transmitter-receiver midpoint. If the GPR antenna pair is moved along the borehole during a push-pull experiment—using saline or any other tracer with electrically contrasting properties to the ambient fluid—then the changes in the GPR traces recorded along the borehole can be directly linked to the spatio-temporal migration of the tracer.

4.4.2. Time corrections, filtering and normalization

The initiation time (time-zero) of the receiver and transmitter antennas varies slightly every time the system is turned on and it may drift over time. To account for this, we applied a time-zero correction following Peterson (2001). After the time-zero correction we applied a digital bandpass filter (a Kaiser Window with edges at 10-40-150-200 MHz) to concentrate on frequencies around the dominant frequency that is indicated by the antenna manufacturer as 100 MHz.

In single-hole GPR acquisition, part of the electric field is refracted at the GPR borehole wall Dorn et al. (e.g., 2011). These refractions (termed borehole refractions in the following) of high amplitude are measured earlier in time than the reflections from the tracer-filled fractures that are located further away. By sealing the GPR borehole with the flexible liner we ensured that the borehole conditions remained constant during acquisition, which implies that the amplitude and phase of the borehole refractions were constant over time at each depth along the borehole.

After the initial time-zero correction, subtle time shifts (with a mean of 0.4 ns and a standard deviation of 0.25 ns) were observed in the borehole refractions when repeating the measurements at the same locations in the borehole. We attribute these time shifts to small variations in the initiation time of each pulse and to cm-scale vertical and/or horizontal shifts in the location of the antennas within the borehole. To correct for these time shifts we compared collocated traces to a reference trace that was measured at each depth before the initiation of the push-pull experiment. Since these time shifts were smaller than the sampling rate, we upsampled each trace at 5 times the original sampling rate by performing a Fourier transform on the data and padding the Fourier spectrum with zeros. We then shifted the upsampled traces so that the borehole refractions coincided with the ones of the reference trace. We subsequently performed an inverse Fourier transform and downsampled the data to the original sampling rate to obtain the resulting phase-shifted traces.

4.4.3. Time-lapse changes and migration

Before each push-pull experiment, the measured GPR data were indicative of the ambient conditions (e.g., water-filled fractures with formation water, the presence of boreholes and double-packer system). After the initiation of the push-pull experiment, the saline tracer started filling the fractures that are connected to the injection interval. The electromagnetic field that is reflected by the tracer-filled fractures becomes amplitude and phase shifted. These changes are subtle and are best appreciated by subtracting the later traces from the reference trace. To minimize the errors in the subtraction process, it is important to precisely locate the traces along the borehole and to align the traces with the reference (see section 4.4.2).

Figure 4.2 displays the reference trace and a trace recorded during a push-pull experiment. We also show the difference of the later trace with respect to the reference trace (difference

trace). The difference trace has clear peaks that accentuate the changes that result from the presence of the saline tracer.
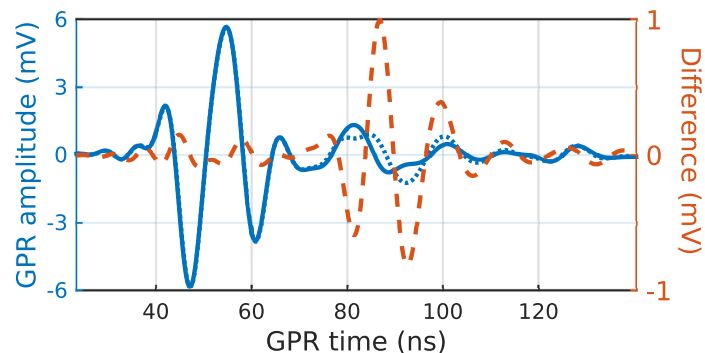
Figure 4.2 – GPR data from experiment I. The reference trace (solid blue line) and a trace measured after pushing (dotted blue line) are shown together with the difference of the two traces (dashed red line). The difference is plotted on a different scale to the right of the figure, that is 6 factors smaller than the initial traces.

To partly account for attenuation of the signal (e.g., Jol, 2008, sec. 1.6.2), we applied a gain to scale the later times in the difference traces with respect to the earlier times. We choose to linearly scale each GPR difference trace with time, with appropriate scaling so that the resulting amplitudes are normalized to 1.

As a final step, we performed migration that refers to the summation of energy along certain paths to account for spherical spreading. A collection of traces along the borehole forms a section. We refer to sections from which the reference is subtracted as difference sections. We migrate the difference sections using a Kirchoff-migration algorithm developed for seismic data from the CREWES Matlab toolbox (http://www.crewes.org/) under the assumption of a constant GPR velocity of $0.12 \text{ m} \cdot \text{ns}^{-1}$. Dorn et al. (2012) showed through extensive cross-hole travel time tomography that the radar velocity in the granite is practically constant and isotropic.

Figure 4.3a illustrates a synthetic 3D-model with the electric field at a given instant in time and the resulting saline tracer distribution (at the end of the injection period) within a rectangular, tilted fracture of uniform (0.5 mm) aperture. For this model, we calculate the GPR forward response using a newly developed algorithm (Shakas and Linde, 2015) to simulate the section prior to (Figure 4.3b) and at the end of the tracer injection (Figure 4.3c). The finite emission time (some 20 ns in this example) of the alternating source manifests itself as positive and negative signal amplitudes in the GPR traces. This effect is visible in the difference section (Figure 4.3d) and the migrated difference section (Figure 4.3e). The finite emission time also implies that the actual fracture location coincides with the shortest distance at which the absolute amplitude of the migrated difference section is above zero (see Figure 4.3e). Indeed, the fracture has an aperture of 0.5 mm, but the corresponding reflection in the migrated difference section shows an imprint of the source over a width of approximately 2 m.
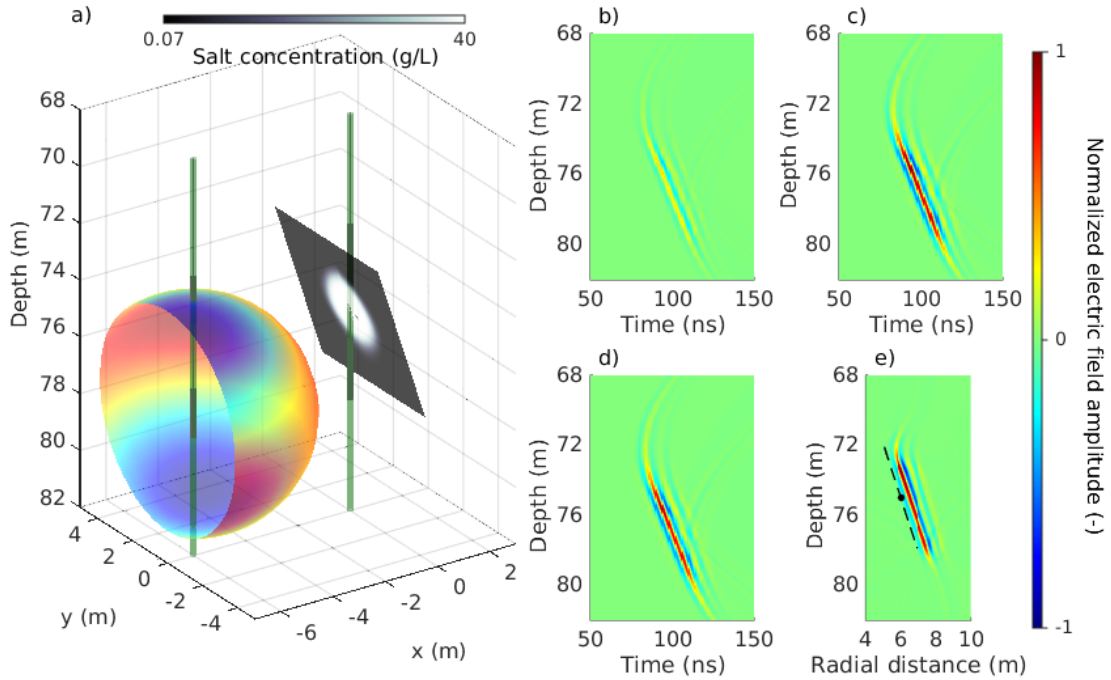
Figure 4.3 – (a) A synthetic 3D model with the electric field and the tracer concentration in a fracture at a given time. (b) The simulated GPR section with formation water, (c) the same section with the tracer distribution (shown in (a)), (d) their difference and the migrated difference section, along with the fracture location and injection point (e). The GPR simulations were performed with a newly developed algorithm (Shakas and Linde, 2015) and the flow-and-transport simulation was done with MaFloT 2D.

4.5. Results

4.5.1. Fixed antenna acquisition

For the fixed antenna acquisition (experiment I in Table 4.1) we kept the midpoint between the transmitter and receiver antennas at 75.1 mdepth while the injection depth was 78.7 m. We chose this location based on results from a previously acquired moving antenna experiment that suggested an upward tracer migration.

First, we computed the Root Mean Square (RMS) of each GPR difference trace and plotted the evolution of the RMS curve over time along with the measured electrical conductivity in the injection interval (Figure 4.4). This measure is representative of the change in the total (measured) reflected electric field and is, therefore, indicative of the volume and electrical conductivity of the saline tracer within the antenna range. In the following, we refer to this type of curve as the GPR breakthrough curve.

Before the push-pull experiment started (reference acquisition) the GPR breakthrough was close to zero and dominated by noise. The saline tracer reached the injection interval at t
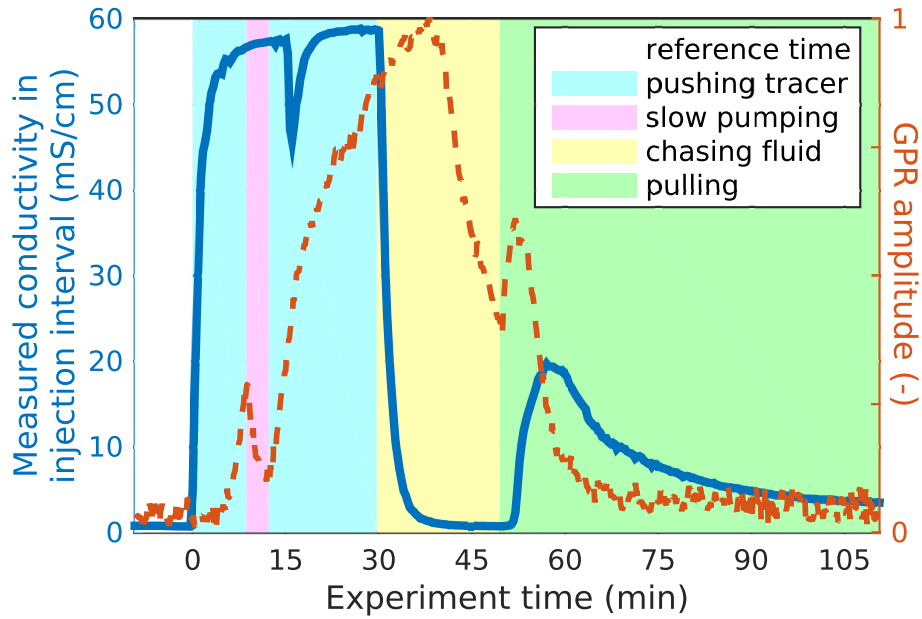
Figure 4.4 – GPR and push-pull data for experiment I (fixed-antenna). The measured conductivity in the injection interval is shown (solid blue line) along with the normalized GPR breakthrough curve (dashed red line).

= 0 min and the magnitude of the GPR breakthrough increased considerably about 5 min later. One reason for this delay is that the antenna system was located above the injection depth and the tracer needed to travel some distance upwards before it was detected. Also, a sufficient volume of tracer must be injected to allow measurable changes in the reflected GPR signal.

At t = 10 min after the saline tracer reached the injection interval, we temporarily paused the saline tracer injection and started to inject a second tracer of ambient conductivity during 3 minutes at 0.33 L·min^{-1}, that is, at a 10 times lower rate than during the saline tracer injection. This period is indicated in Figure 4.4 as 'slow pumping'. Note that the second tracer was injected at the surface and it took about 3 min to reach the injection interval (seen as a decrease in the measured conductivity at t = 15 min). The GPR breakthrough curve responded to the lower injection rate by a sharp decrease of its amplitude that only starts to increase after the previous flow rate and saline tracer injection was resumed.

The peak in the tracer breakthrough curve was reached at t = 25 min and the GPR breakthrough curve shows a clear maximum at t =38 min. After the peak was reached in the GPR breakthrough curve, the amplitudes start decreasing as the tracer was diluted by the addition of the chaser fluid and migrated away from the antenna location.

During the pulling phase, another peak was observed in the GPR breakthrough curve at t =52 min that is smaller in amplitude and duration. The peak in the pulling phase was reached later in the tracer breakthrough than in the GPR breakthrough because the tracer first passed by the static antenna setup before migrating further down towards the injection interval, at 78.7 m, before it reached the CTD diver in the injection interval. At times later than t =70

83

min, the GPR breakthrough curve showed noisy behavior at an amplitude that was more than twice the one measured before the tracer injection.

4.5.2. Moving antenna acquisition

During the moving antenna acquisitions – see experiments II to V in Table 4.1 – we monitored over a depth range that was wide enough to capture all expected changes induced by the saline tracer. Here we present experiment II that had the same experimental parameters as experiment I, apart from the moving antenna setup. The difference sections after migration are shown for this experiment, along with the acquisition times, in Figure 4.5. Note that we only present the part of the depth section where temporal changes are visible. The migration of the saline tracer from the injection location through an upward trajectory of roughly 8 m is clearly seen. The maximum extent of the tracer is found in Figure 4.5h, which corresponds to a difference section acquired at the end of the chaser injection. The sharp change in the distribution of tracer between pushing and pulling is most evident by comparing the difference sections obtained right before (Figure 4.5h) and right after (Figure 4.5i) the initiation of the pulling phase. There are little indications of significant amounts of remaining tracer at the end of the experiment (Figure 4.5j). Throughout the experiment, a fraction of the tracer remained close to the injection location.

In Figure 4.6 we plot the tracer breakthrough curve along with the GPR breakthrough curves at three depths that are indicated in Figure 4.5j. The three depths were chosen such that one is close to the injection depth, one is the same as the depth during the fixed antenna acquisition (see section 4.5.1) and one is close to the furthest extent of the tracer imaged by the GPR. In the moving antenna configuration, GPR measurements at a given depth were repeated every ~5 min. As expected, the noise levels in the GPR breakthrough curves were noticeably higher than for the fixed antenna acquisition—around 0.3 normalized units for the moving acquisition compared to 0.05 normalized units for the fixed acquisition—but a clear signal related to tracer transport was still evident.

Near the injection location at 76.8 m depth we measured strong difference signals towards the end of the saline tracer injection that decreased during the chasing period but prevailed until the end of the pulling period, suggesting that saline tracer was still present at this depth. The GPR breakthrough curve was considerably above the noise level from $t = 5$ min to $t = 68$ min. At the depth of 75.1 m (same as the fixed antenna experiment) we measured a peak with smaller amplitude that extended from $t = 15$ min to $t = 55$ min. Finally, the GPR breakthrough curve measured at 71.5 m reached a well-defined peak at $t = 56$ min. The saline tracer did not remain for a long time at this depth, but a considerable volume must have reached this depth interval to account for the strong changes in reflectivity (also seen in the surrounding traces in Figure 4.5h).
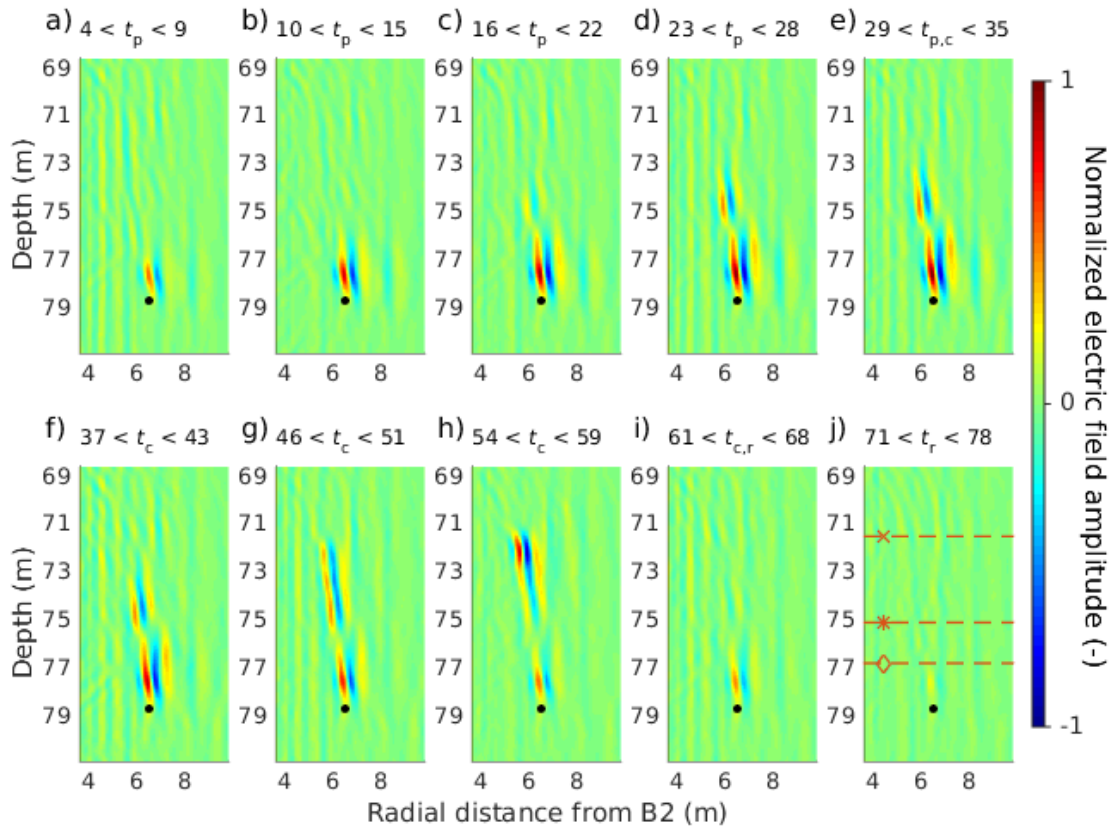
Figure 4.5 – Migrated difference sections from experiment II. The black dot indicates the injection location and the acquisition times for each section (in min) are shown at the top of the sub-figures along with the phase of the push-pull experiment indicated by the index (p:pushing, c:chasing, r:pulling). The dashed red lines in 4.5j are analyzed in Figure 4.6.

4.5.3. Imaging ambient transport processes during the resting time

We now present the results of experiment III that was performed with the saline injection at 50.9 m (see Table 4.1), a moving antenna acquisition and a resting time (4:35h) between pushing and pulling. This experiment highlights density related effects. As before, we only show the depth interval where strong temporal changes occurred. We have no GPR data between $t = 180$ min and $t = 270$ min as we charged the antenna batteries during this time period.

We present the difference sections from this experiment in Figure 4.7 and focus on two regions: an upper region found above the injection depth and a lower region found below the injection depth (shown in Figure 4.7a). The migrated difference sections show that changes during the pushing period arise mainly in the upper region and in the vicinity of the injection location (Figs. 4.7b and 4.7c). During the chasing period, from $t = 30$ min to $t = 50$ min, some of the tracer migrated to the upper region from 51 m to 47 m depth and some to the lower region from 52 m to 54 m depth (seen in Figs. 4.7d and 4.7e). At the beginning of the resting
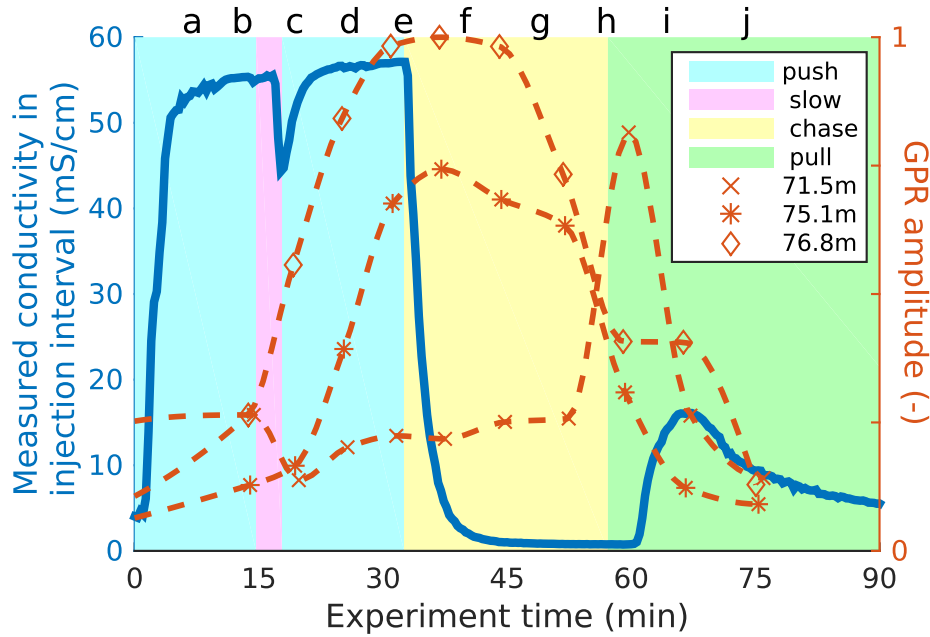
Figure 4.6 – Plot of the measured conductivity in the injection interval (solid blue line) along with the GPR breakthrough curves (dashed red lines) during experiment II. The GPR breakthrough curves are shown for three depths (see Figure 4.5j). The letters at the top of the figure refer to the times at which the GPR profiles were taken (see the difference sections in Figure 4.5).

period, some tracer remained in the vicinity of the injection location (3 m radial distance and 51 m depth in Figure 4.7f). During the pulling phase (Figure 4.7i), the tracer from the upper region is recovered very quickly while the tracer in the lower region takes more time to be recovered. The tracer breakthrough curve is shown in Figure 4.7k.

The two regions of interest showed considerably different responses. The upper region shows amplitude differences at early times that were strongly attenuated during the resting time, and almost disappeared once the pulling begun. The lower region showed considerable amplitude differences that arise at the end of the pushing period (Figs. 4.7d to 4.7i). The saline tracer that caused this change exhibits a strong downward migration during the resting time, from 55 m (Figure 4.7f) to 59 m (Figure 4.7h).

In Figure 4.8 we plot the GPR breakthrough curves for the complete depth range at which changes were visible during the experiment. The injection depth and the two areas of interest (upper and lower region) are indicated. As was evident in the migrated sections of Figure 4.7, we can see the upward and downward migration of the tracer from the injection depth. In this figure, the downward migration of the tracer during the resting time is evident from $t = 60$ min and $t = 330$ min. During the resting time and after we charged the batteries, we measured weaker GPR differences in the top than in the lower region (see Figure 4.8 between $t = 270$ min and $t = 330$ min). During the pulling phase, the GPR breakthrough curves in the upper region were quickly attenuated while the ones in the lower region showed considerably high values throughout the acquisition period.
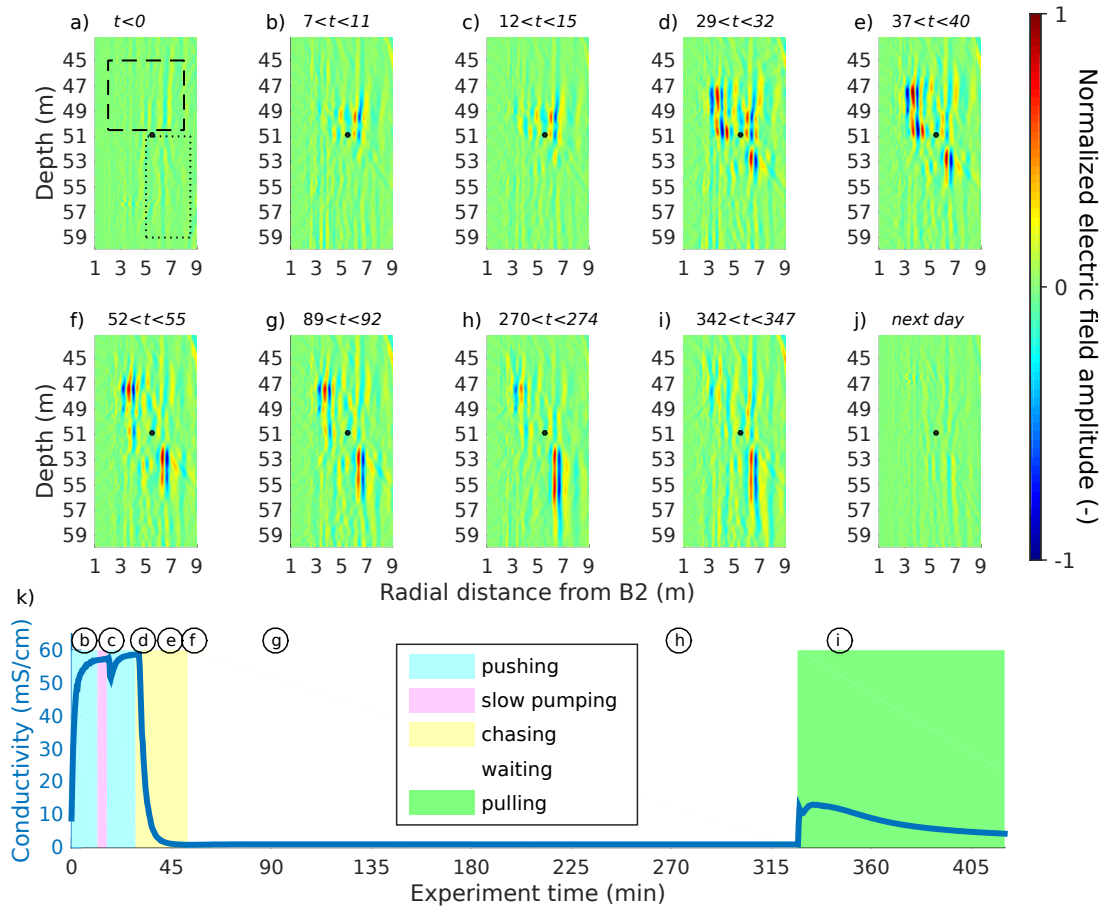
Figure 4.7 – Figures (a) to (j) show the migrated difference sections from experiment III. The black dot indicates the injection location and the acquisition times for each section (in min) are shown at the top of the sub-figures and also indicated along with the measured conductivity in the injection interval (k).

4.6. Interpretation

In this section, we discuss how the coupling of push-pull tracer tests and GPR imaging provides a means of estimating transport length scales, transport velocities, ambient flow and density effects.
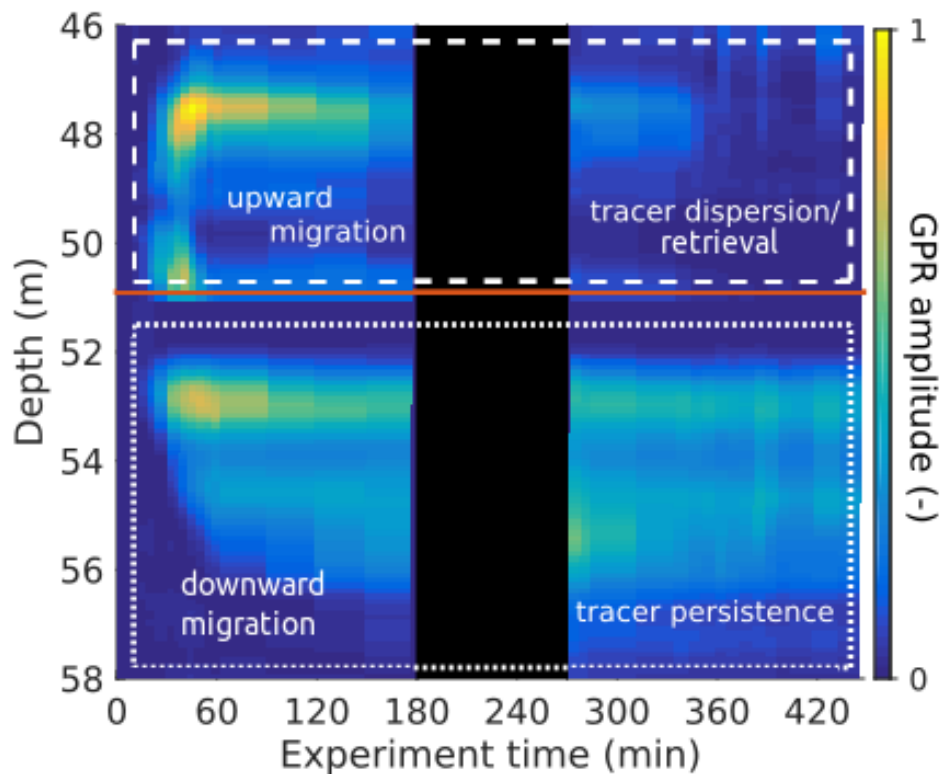
Figure 4.8 – Plot of the GPR breakthrough curves computed for experiment III. The injection depth at 50.9 m is shown with the solid (red) line. The dashed and dotted rectangles correspond to the regions shown in Figure 4.7a. The GPR antenna batteries were charged between $t = 175$ and $t = 270$ min.

4.6.1. Transport length scales

One major advantage of coupling push-pull experiments with GPR difference imaging is that the representative length scale of the experiment can be quantified, that is, how far did the saline tracer flow into the formation. For example, during the pushing and chasing phase of experiment II (Figure 4.5) with injection at 78.7 m, the saline tracer migrated approximately 8 m upwards from the injection location in a clearly defined trajectory. This is in contrast to the same phases of experiment III (Figure 4.7) with injection at 50.9 m, in which the saline tracer was seen to migrate less than 4 m from the injection location, but in several separate trajectories. Furthermore, different transport length scales are also highlighted within a single experiment when some of the tracer remains relatively close to the injection, while the rest of the tracer migrates further away. This information is crucial to assess the volume investigated by the tracer tests, as well as the characteristic fracture surface that is seen by the tracers, especially when considering reactive transport. It also helps to define the appropriate conceptual model for fracture flow and transport.

4.6.2. Transport velocities and associated scale effects

Another important advantage of single-hole GPR difference imaging is that inference about the tracer mean velocity can be made, since the tracer is mapped in both space and time. To demonstrate this, we consider the GPR breakthrough curves during the pushing and chasing period of experiments II, IV and V. These experiments were conducted at the same location and apart from minor changes in the experimental parameters (injection rate, tracer concentration and volume) they can be considered otherwise identical. We used the corresponding GPR breakthrough curves at each depth interval to compute a mean arrival time of the tracer that we defined as the time at which each curve crosses a noise threshold , set as 30% of the maximum value seen in the difference images. In Figure 4.9, we plot the travel distance as a function of the mean arrival time of the tracer along its complete trajectory after chasing (see Figure 4.5h for the complete trajectory), hence, the slope of this plot can be thought of as the mean velocity of the tracer. The overall agreement of the mean arrival times for the different experiments not only indicates that the push-pull experiments and the GPR monitoring results were repeatable, but also that calculating GPR breakthrough curves is a sound approach.
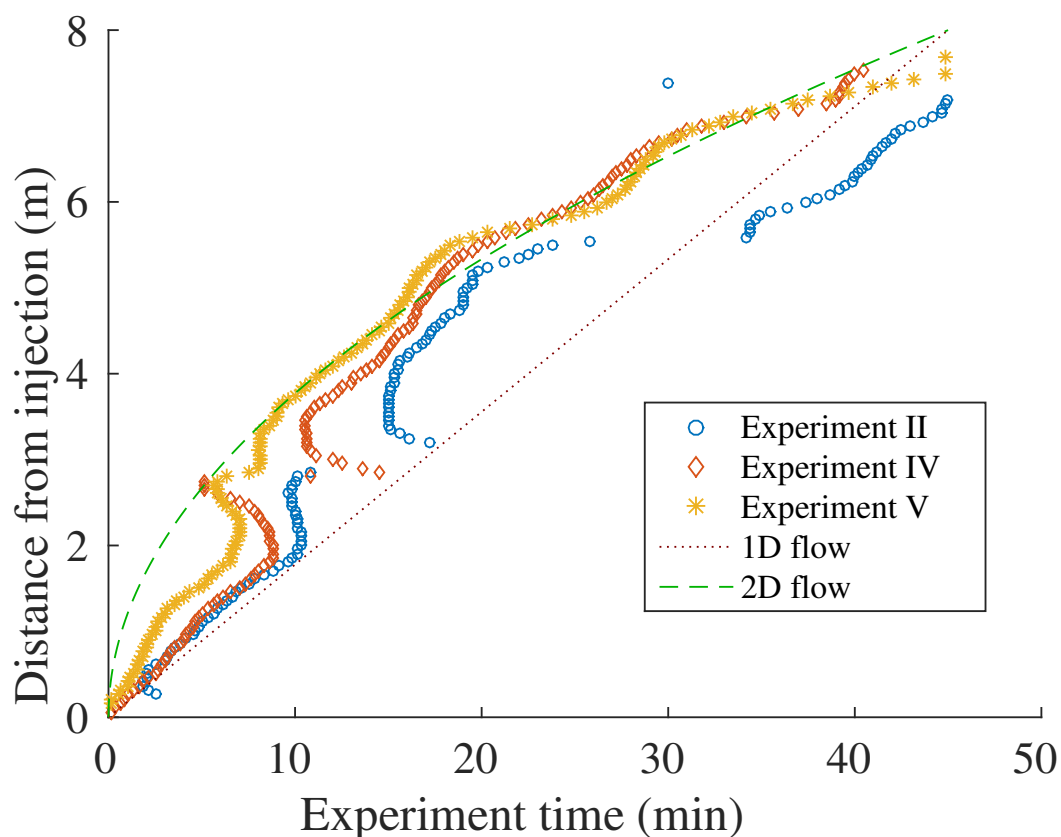
Figure 4.9 – Travel distance versus time of the saline tracer for experiments II, IV and V, computed using the GPR breakthrough curves. The analytic solutions for 1D (channelized) and 2D (planar) flow are also shown, assuming the saline tracer travels a total distance of 8 m in 45 min.

From this plot we can identify two flow regimes; for the first 3 meters the tracer velocity appears to be constant (at $0.18\,\text{m}\cdot\text{min}^{-1}$ min-1, expected for channelized flow) and for the next 4 meters the velocity is decreasing with a rate as expected for radial flow along a plane. For comparison, we plot the analytical solutions of advective transport within a 1D pipe and within a 2D fracture plane. We assume that the tracer reaches a distance of x = 8 m within t = 45 min and compute the curves $x = (\frac{8}{45})\,t$ for the 1D solution and $x = (\frac{8}{45}^{1/2}\,t^{1/2}$ for the 2D solution.

4.6.3. Geometric properties of transport flowpaths

Another type of information that is lacking in classical push-pull experiments is information about the complexity of the pathways that the tracer follows, such as the number of fractures involved as well as their orientations and sizes. For example, borehole optical logs of B1 (Belghoul, 2007) along with prior push-pull and flowmeter tests suggest the presence of an open fracture with a dip angle of 15° at 78.7 m and another with a dip angle of 37° at 50.9 m (Le Borgne et al., 2007). From the difference sections obtained in experiment II (Figure 4.5), we see changes that originate from the injection at 78.7 m and extend vertically upwards at an angle steeper than 70°. This suggests that the sub-horizontal fracture that intersects the borehole is connected to a major sub-vertical fracture that is dominating the flow behavior during the experiment. Similarly, the difference sections for experiment III (Figure 4.5) suggests that the flow originating from the injection location at 50.9 m is dominated by two sub-vertical fractures on either side of the injection location. Since these fractures do not intersect the injection interval, a sub-horizontal fracture (not clearly visible in the difference sections) may have provided the necessary pathway for the tracer. The presence of a sub-horizontal fracture in this injection interval is in agreement with Dorn et al. (2011, 2013).

4.6.4. Observation of density effects and ambient flow

It is important to assess the effect of density on the tracer distribution as we use a tracer with a high salinity contrast. In experiment I (Figure 4.4) we measured a decrease in the GPR breakthrough curve when the pumping rate is lowered (by a factor of 10) to inject the second tracer, and the curve only continued to increase when the previous pumping rate was resumed. Since the antennas were located 3.6 m above the injection interval, this decrease may have occurred because the lower pumping rate was not sufficient to push the tracer upwards, but instead a downward (density-driven) migration of the tracer occurred. Immediately after the previous pumping rate resumed, the tracer continued its upward migration and the GPR breakthrough curve peaks during the chasing period. A smaller peak is seen when the flow is reversed that results from the downward migration of the tracer towards the injection interval.

In experiment II (Figure 4.5) we saw an upward migration of the tracer during the pushing and chasing, followed by a sharp decrease in GPR difference amplitudes in the upper region (71 to 75 m) as soon as pulling begun (compare Figs. 4.5h and 4.5i). As already suggested in the

previous paragraph, the sharp decrease partly occurs due to the fast downward migration of the tracer. However, some of the visible tracer may have been dispersed into sub-horizontal fractures to which our GPR data are largely insensitive. Ambient flow in these fractures may have led to the low mass recovery for this experiment (Table 4.1).

In experiment III (Figs. 4.7 and 4.8) we see different behavior of the tracer in the upper (45 to 51 m depth) and lower (51 to 59 m depth) regions relative to the injection interval. While the upper region shows strong amplitude changes early on, the amplitudes are quickly diminished during the resting time, possibly due to ambient flow in this location that causes the tracer to be quickly dispersed. As soon as pulling started, the GPR breakthrough curves from this region are quickly attenuated to the background level. On the contrary, the lower region exhibits persistent amplitude differences with respect to the reference throughout the whole experiment, indicating that this fracture is perhaps not strongly affected by ambient flow. The same analysis performed on experiment IV showed that the tracer persists during the resting time in the bottom part of the fracture (from the injection depth to 76 m depth in Figure 4.5) while in the top part (from 76 m to 71 m in Figure 4.5) the tracer is quickly dispersed.

Another effect that is visible in both the difference sections (Figure 4.7) and in the GPR breakthrough curves (Figure 4.8) is the vertical spreading of the saline tracer, mainly during the resting time, in the fracture found in the lower region. This is most likely due to density effects since the saline tracers used have strong density contrasts to the surrounding fluid. Note that saline tracers are needed to image tracer transport with GPR difference methods but the salinity could be reduced to minimize density effects, while still conserving sufficient contrasts in the GPR images.

4.6.5. Physical meaning of early tracer breakthrough

To investigate the effect of density on the push-pull results we simulated experiment II, using the measured flow rates and converted the electrical conductivity into salinity (Sen and Goode, 1992) using the reference temperature of 25°C used by the CTD diver. For the simulation, we modified a finite volume solver for flow-and-transport in 2D porous media (Künze and Lunati, 2012b). The solver allows for density effects by incorporating the force of gravity into the solution of the flow velocity. We adjusted the permeability to account for the transmissivity of a parallel plate fracture through the cubic law (e.g., Lunati et al., 2003) and scaled the porosity by the aperture to account for the volume occupied by the tracer. To allow for inclinations of the fracture we multiply the gravity term by a component that is equal to the sine of the dip angle. Flow in a fracture with zero dip angle is therefore not affected by gravity. Guided by the changes shown in the GPR sections of experiment II (Figure 4.5), we defined as a modeling domain a fracture with no-flow boundaries on the bottom and sides and with an open boundary on the top so that tracer movement would be primarily upwards. To avoid any tracer reaching the open boundary we kept the total volume of the fracture two times larger than the volume of injected fluid in the domain. We then performed a local optimization search (using the golden search algorithm) to match the peak arrival in the data with a uniform aperture. Note that this simplified model that ignores dispersion,

fracture heterogeneity, and ambient flow only serves to highlight the impact of density and fracture dip on the peak arrival time, and that no emphasis has been placed on fitting the tail of the tracer breakthrough curve and honoring the recovered mass.
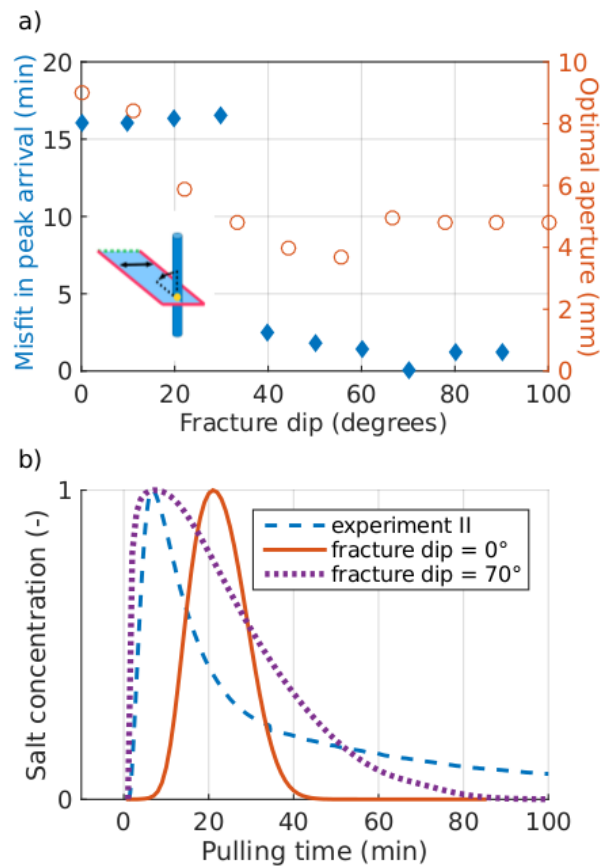
Figure 4.10 – (a)Plot of the misfit (left axis) between the simulated and measured peak arrival time of the saline tracer in experiment II (see subfigure for the modeling setup). Injection was performed at the bottom of a uniform fracture (yellow circle) with no-flow boundaries (red solid lines) on the bottom and two sides. The distance between the two sides (double arrow) was adjusted so that the tracer would reach a length of 8 m at the end of the chasing period while the open boundary at the top (dashed green line) was kept far from the tracer. The simulations were performed for 10 dip angles (inclined arrow), between 0° and 90°, and each simulation was optimized to obtain the best fitting mean aperture (right axis). The (normalized) best fitting simulation for 0° and 70°, along with the measured concentration for experiment II are shown in (b).

Using this simplified model we attempted to reproduce the early arrival of the tracer seen in the tracer breakthrough curve (Figure 4.6). We allowed the fracture dip to vary between 0° (no density effect) and 90° (maximum density effect) in increments of 10°. The width of the fracture, for a given aperture, was chosen such that the volume of tracer at the end of the chasing phase would occupy a length of 8 m along the fracture. This constraint was motivated by the GPR difference sections (Figure 4.5h). In Figure 4.10a, we plot the optimal aperture for

each dip angle along with the misfit in peak arrival time between the simulations and the experiment. It is evident that high dip angles are required to fit the early arrival times obtained in the experiment, with an optimal effective aperture of roughly 5 mm. The simulations not only indicate that the effect of density should be modeled when using highly saline tracers, but more importantly that the constraints on the tracer trajectory obtained from the GPR difference images are necessary to obtain realistic estimates. We also plot (Figure 4.10b) the measured and (optimal) simulated curves for fractures with 0 and 70 degrees dip angle. Note that we use a normalized concentration for comparison purposes, since our modeling does not account for processes that would reproduce the lower mass recovery seen in the field data.

4.6.6. Breakthrough curve tailing

As discussed in section 4.3, previous fluorescent dye experiments measured power law breakthrough curve tailing, such as c(t) $\sim t^{1-b}$ at late time, with b ranging from 0.75 to 1, and concluded to a limited role of matrix diffusion in this low porosity granite (Kang et al., 2015). The tailing behavior measured here is more pronounced, showing a behavior close to c(t) $\sim t^{-1}$. This strong tailing is thus likely induced by density effects affecting the transport of the saline tracer used in these experiments.
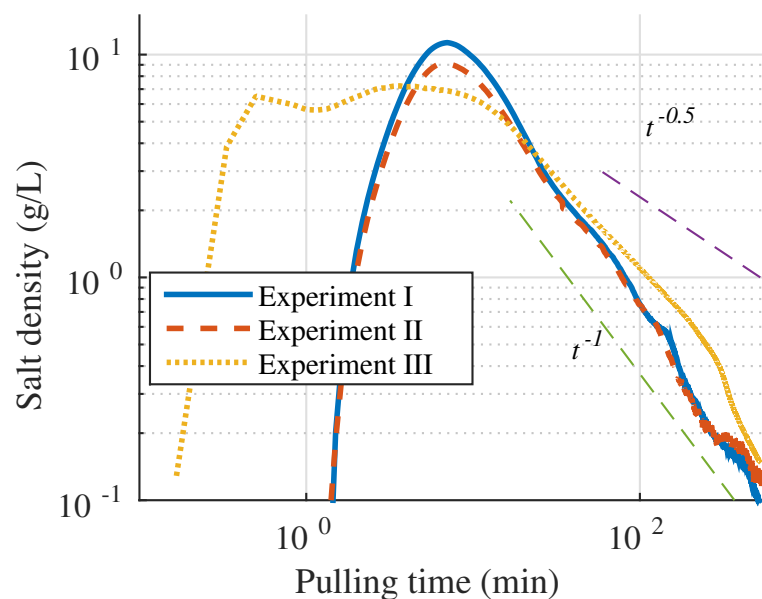
Figure 4.11 – Measured tracer breakthrough curves for experiments I, II and III presented in Table 4.1 along with plots for arrival times with exponents -1 and -0.5.

Our results (Figs 4.4, 4.6 and 4.8) suggest a strong link between the tracer and GPR breakthrough curves. In Figure 4.11 we plot the tracer breakthrough curves for experiments I, II and III. The repeatability of the push-pull experiments is evident in the tracer breakthrough curves for experiments I and II (same experimental parameters), while the tracer break-

through curve for experiment III (a different injection location) indicates an early arrival time and a longer tail compared to the other two experiments. During the later part of the pulling period (between $t = 100$ and $t = 200$ min) the concentration of recovered tracer is higher in experiment III than in the other two experiments. This agrees well with the GPR difference sections (Figure 4.7) and the GPR breakthrough curves (Figure 4.8), which show persistent reflections arising from the lower region. The tailing in the tracer breakthrough curve, in light of the GPR results, can thus be attributed to tracer that has migrated downwards during the resting time.

4.7. Conclusions and Outlook

Combined push-pull tracer tests and single-hole GPR monitoring experiments with a saline tracer provides important insights into a range of transport phenomena that can be observed in situ in fractured rocks. This includes characteristic length scales of transport, scale effects in transport velocities, ambient flow and density driven migration, and trapping effects. The information contained in the single-hole GPR reflections helps to gain physical understanding of the processes that are responsible for the observed tracer breakthrough curves.

During a fixed antenna experiment we measured a GPR breakthrough curve that was consistent with the tracer breakthrough curve and provided a means to investigate the rise and decay of tracer concentrations at different distances along the main fracture flow paths. This relationship was used to deduce a mean velocity of the saline tracer during the moving antenna experiments. During the push phase we observed a scale effect in tracer displacement, with a transition from linear to radial flows. This suggests that a significant flow channeling controls transport until a characteristic scale of about 3 meters, above which it follows a radial behavior. Our results demonstrate that GPR monitoring combined with push-pull saline tracer tests is useful to image flow channeling in fractured rocks, at least in the near field around boreholes.

We used a 2D flow and transport solver, modified to simulate flow in a parallel plate fracture, to show that, when density effects are significant, the peak tracer breakthrough time is highly sensitive to the fracture dip. Our modeling results suggest that a large dip is necessary to reproduce the early tracer arrival measured in the field and this is in agreement with the large dip seen in the GPR difference sections.

These experimental results offer new perspectives for combined hydrogeophysical modeling of fractured rock formations. In particular, the new insights obtained may be very useful for interpreting reactive tracer tests, often performed in push-pull configuration (Istok, 2012) since reaction rates are expected to depend on the spatial tracer distribution and its surface of exposure to the rock. To obtain quantitative information on tracer mass distribution in situ, we plan to couple flow-and-transport modeling with a recently developed approach to simulate GPR reflections from saline-occupied fractures of arbitrary orientation and aperture (Shakas and Linde, 2015).

Chapter 5

Neutrally-buoyant tracers in hydrogeophysics: Field demonstration in fractured rock

Alexis Shakas, Niklas Linde, Ludovic Baron, John Selker, Marie-Françoise Gerard, Nicolas Lavenant, Olivier Bour and Tanguy Le Borgne.

Published[1] in *Geophysical Research Letters* and herein slightly adapted for this thesis.

5.1. Abstract

Electrical and electromagnetic methods are extensively used to map electrically conductive tracers within hydrogeologic systems. Often, the tracers used consist of dissolved salt in water, leading to a denser mixture than the ambient formation water. Density effects are often ignored and rarely modeled, but can dramatically affect transport behavior and introduce dynamics that are unrepresentative of the response obtained with classical tracers (e.g., uranine). We introduce a neutrally-buoyant tracer consisting of a mixture of salt, water and ethanol, and monitor its movement during push-pull experiments in a fractured rock aquifer using ground penetrating radar. Our results indicate a largely reversible transport process and agree with uranine-based push-pull experiments at the site, which is in contrast to results obtained using dense saline tracers. We argue that a shift towards neutrally-buoyant tracers in both porous and fractured media would advance hydrogeophysical research and enhance its utility in hydrogeology.

5.2. Introduction

Geophysics enables remote monitoring and imaging of subsurface mass transfer at scales ranging from decimeters (e.g., Garré et al., 2011; Beff et al., 2013), meters (e.g., Slater and Sandberg, 2000; Singha and Gorelick, 2005), kilometers (e.g., Falgàs et al., 2009; Rosas-Carbajal et al., 2015) and beyond (e.g., Zhdanov et al., 2011). The need for methodological developments that ensure appropriate integration of geophysical data in subsurface hydrology have given rise to the research field of hydrogeophysics (Hubbard and Linde, 2011; Binley et al., 2015), which has had an impact on hydrology over the last decade (NRC, 1996). In hydrogeophysics, geophysical experiments are made to support hydrological research and applications. This implies that geophysical data should not only be informative of the processes being studied, but also that its acquisition should not perturb hydrological data or significantly affect the design of hydrological experiments.

In order to image tracer (or contaminant plumes) with geophysics, there must exist a naturally occurring or imposed contrast in physical properties between the tracer (contaminant) and the surrounding formation water. When such a contrast is present, geophysical imaging can provide insight into the transport processes that take place in the hydrogeological system. In situ imaging of transport processes with geophysics may thus help to unravel complex processes, such as anomalous transport, dual-domain mass transfer or reversible/irreversible dispersion, that are often difficult to infer from breakthrough curve analysis alone (Swanson et al., 2012, 2015). In groundwater geophysics, the contrast agent for tracer tests is often dissolved table-salt (NaCl) (Day-Lewis et al., 2003; Singha and Gorelick, 2005; Doetsch et al., 2012; Shakas et al., 2016).

Salt increases the electrical conductivity and enables tracking of tracer plumes using electrical (Kemna et al., 2002; Singha and Gorelick, 2005), induction-based electromagnetic (e.g., Falgàs et al., 2009; Rosas-Carbajal et al., 2015) or high-frequency electromagnetic (Day-Lewis

et al., 2003; Tsoflias and Becker, 2008) methods. Note that the studies mentioned above have been conducted in both fractured and porous-media systems. The salinity contrast needed for reliable geophysical imaging implies that the saline solution is significantly denser than the surrounding water, which results in buoyancy-induced tracer movement; this has been verified in both laboratory experiments (e.g., Istok and Humphrey, 1995) and numerical tests (e.g., Beinhorn et al., 2005; Kemna et al., 2002). Doetsch et al. (2012) provide a field demonstration of density effects using time-lapse electrical resistivity tomography. In accordance with numerical modeling, they found that a tracer injected in a gravel aquifer rapidly plunged to the underlying clay aquitard. Previous field experiments with lower salinity contrasts (and less density effects) at the site did not enable reliable time-lapse inversion results.

In the hydrogeophysics literature, it is rare to find field-based studies in which density effects are assessed or accounted for (e.g., Doetsch et al., 2012; Shakas et al., 2016; Haaken et al., 2017). Even if density effects are considered in the modeling and associated inversion, the ubiquitous use of dense saline tracers in hydrogeophysics is problematic as they change the system dynamics (Tenchine and Gouze, 2005). That is, the use of geophysics imposes constraints on experimental design that might be unacceptable for field hydrogeologists. This implies that (1) hydrogeologists might be reluctant to consider geophysics in their work if they feel that hydrological experiments will be compromised by using dense tracers, (2) that comparisons between hydrogeophysical results and hydrogeological experiments using non-salt tracers are difficult and (3) that the inferred system properties and hydrological processes might have low predictive capacity in describing natural flow dynamics.

In this work, we introduce a neutrally-buoyant tracer based on a water-salt-ethanol mixture that we refer to as wethanalt. Ethanol is fully miscible and has a similar viscosity as water. It is less dense than water and can be used to ensure that the resulting tracer solution is neutrally buoyant, while it maintains a high electrical conductivity with respect to the formation water. Furthermore, ethanol has the distinct advantage of being non-toxic (Thakker, 1998) and biodegradable (Schaefer et al., 2010).

We present two field experiments in which we demonstrate the value of using neutrally buoyant and electrically conductive tracers for imaging transport processes. We consider push-pull experiments at a well-characterized fractured rock site with geophysical monitoring using single-hole ground penetrating radar (Dorn et al., 2011, 2012). Our results are compared with previous experiments at the site that were carried out using dense saline solutions (Shakas et al., 2016) and a traditional push-pull experiment using a fluorescein tracer, without geophysical monitoring (Kang et al., 2015).

5.3. Methodology

The properties of ethanol-water and salt-water mixtures have been tabulated (Hammond, 2016). To the best of our knowledge, such a laboratory study does not exist for wethanalt (ethanol-water-salt mixtures). Here, we present a practical method for obtaining a neutrally buoyant wethanalt mixture by utilizing the existing tables as a guide and further fine-tuning the density in the field. In the following section, where not otherwise noted, the material properties of ethanol, water and salt are taken from Hammond (2016).

5.3.1. Wethanalt Properties

Ethanol (C_2H_6O) has a density of 0.789 g·cm^{-3}, relative electrical permittivity of 25.3 (zero-frequency limit) and dynamic viscosity of 1.203 mPa·s at 20°C. At the same temperature, demineralized water (H_2O) has a density of 1 g·cm^{-3}, relative electrical permittivity of 81 and dynamic viscosity of 1.004 mPa·s. Both liquids are electrically resistive and it is the addition of salt to the mixture that will determine the electrical conductivity. The most common choice of salt in hydrogeophysical applications is sodium chloride (NaCl), that dissociates into Na^+ and Cl^- ions when dissolved in water.

Ethanol and water are miscible in all proportions and their mixing results in an exothermic reaction (Peeters and Huyskens, 1993) which leads to an increase in temperature when the mixture is prepared. Another property of ethanol-water mixtures is that the dynamic viscosity of the mixture is increased compared with the constituents. The maximum viscosity of the mixture is 2.85 mPa·s (20°C) when the mass proportion of ethanol to water is 0.42:0.58. Ethanol does not pose any health risks when diluted with water (Thakker, 1998) and is bio-degradable (Schaefer et al., 2010), which implies that it may increase microbial activity when used as a tracer.

5.3.2. Wethanalt Preparation

The preparation of a neutrally-buoyant wethanalt solution is complicated by the facts that (1) the density of an ethanol-water mixture does not average arithmetically when adding salt and (2) that the necessary precision in density needs to be sufficiently low (for instance, Istok and Humphrey (1995) perform a laboratory study and report density effects for density variations ($\Delta\rho$) in the range 0.0075% $\leq \Delta\rho \leq$ 0.15%). To achieve this, our preferred field procedure is to first rely on tabulated values in Hammond (2016) to obtain a desired density of an initial ethanol-water mixture and then assume arithmetic averaging to predict the necessary amount of salt to add, in order for the density to be equal to that of the formation water. We then prepare a wethanalt mixture with 5% less salt than predicted with this simple model. For our experiments we first mixed 85 L of demineralized water with 25 L of (99.98%) ethanol; this resulted in an increase in temperature of 8°C. The viscosity of the mixture was 2.26 mPa·s according to Hammond (2016). We then pumped formation water through a plastic tube that was coiled in the ethanol-water container, in order to reduce the temperature of the

mixture to the ambient water temperature. Using this approach, we successfully reduced the temperature of the tracer mixture in all wethanalt experiments from ~ 24 °C to ~ 18 °C, while the ambient water temperature is 16 °C.

To achieve a neutrally buoyant solution, we relied on Archimedes' principle, namely, that "Any object, wholly or partially immersed in a fluid, is buoyed up by a force equal to the weight of the fluid displaced by the object" (Archimedes, 1987). To do so, we used two containers; the first filled with the wethanalt mixture and the second containing formation water. In the second container, we submerged a balloon that we carefully filled with formation water and allowed for any air bubbles to escape. The balloon weighted 3.5 kg and was slightly positively buoyant, so we further adjusted its weight with plastic O-rings (3 g each with a density of 1.1 $g \cdot cm^{-3}$, resulting in a net submerged-weight of 0.3 g per O-ring) until we reached neutral buoyancy (i.e., not observing any vertical movement of the balloon when suspended in the middle of the water-filled container). The weight adjustments were made to a precision below 0.1 $g \cdot kg^{-1}$. We then transferred the balloon with the attached O-rings to the wethanalt container, in which we had mixed an initial amount (4 kg) of salt in the ethanol-water mixture, well below the amount (4.22 kg) predicted from arithmetic averaging. We then proceeded to add salt in increments between 20-80 g, until the balloon was neutrally buoyant in the wethanalt mixture. In the final stage, a total of 4.44 kg of salt was added and the mixture was stirred with a mixing propeller to ensure well mixed conditions. This procedure allows us to obtain a wethanalt solution that is at most 0.01 % different in density than the formation water. While ethanol is biodegradable (Schaefer et al., 2010), it also does not pose any substantial health risks after sufficient dilution (Thakker, 1998).

5.3.3. Setup of the Field Experiment

We performed the wethanalt push-pull experiments in a well-characterized fractured granitic aquifer located in Brittany, France (http://hplus.ore.fr/en). Previous studies indicate that flow at the site is dominated by a few, highly transmissive fractures (Le Borgne et al., 2007; Dorn et al., 2011). All the experiments were performed in two adjacent boreholes, B1 and B2, that are separated by ~ 6 m. A double packer system isolated a fracture intersecting the B1 borehole at 77.8 m, in which we injected the tracer followed by an almost equal volume of formation water (chaser). We then reversed the flow in order to retrieve the tracer, either immediately (push-pull) or after a waiting period (push-wait-pull) during which the pumps were off.

GPR monitoring took place at 5 cm intervals between 60 m and 85 m depth along borehole B2, that was isolated with a borehole liner (Shakas et al., 2016). In an effort to further separate the direct wave from the reflections of interest, we reduced the transmitter-receiver offset from 4 m by Shakas et al. (2016) to 3.2 m. The final images account for this offset during migration.

5.3.4. Data Processing

Tracer Breakthrough Curves

We transformed electrical conductivity values, measured using a conductivity-temperature-depth (CTD) diver located at the outlet of the pump used for pulling, into salt concentration (Sen and Goode, 1992). We then removed the background concentration and normalized the data to the injected tracer concentration, also with the background concentration removed. We also shifted the breakthrough data to account for the time it takes for the water to flow through the tubing from the packer to the outflow location. The experiments using the dense saline tracer published by Shakas et al. (2016) were performed in 2014 and the wethanalt experiments in 2016. For both field campaigns, we performed a series of tracer experiments. This implies that any unrecovered salt may lead to an increasing background concentration over time. To account for this, we present the uncertainty in the breakthrough curves (BTCs) with a thickness (see Figures 5.1i, 5.2i, 5.3) obtained by varying the considered background concentration between a minimum (ambient concentration at the beginning of the field campaign) and a maximum (initial concentration at the beginning of each experiment). In order to compare experiments with different tracer/chaser volumes and flow-rates, we normalize the time of each experiment with the theoretical peak arrival time. In an ideal push-pull experiment (Neretnieks, 2007), the theoretical peak arrival time (t_{peak}) measured from the onset of pulling depends on the duration of both injection ($t_{\text{injection}}$) and chasing (t_{chasing}) and is given by $t_{\text{peak}} = t_{\text{injection}}/2 + t_{\text{chasing}}$. The same formula applies to push-wait-pull experiments in the absence of ambient flow.

Migrated GPR Difference Sections

The processing of the GPR data is described in Shakas et al. (2016). To each GPR trace, we apply a bandpass filter with a frequency window between 20 and 200 MHz (the emitted signal is centered at 100 MHz) followed by minor time shifts to align collocated traces. Compared with Shakas et al. (2016), the only difference in the processing was the use of Singular Value Decomposition (SVD) to remove the direct wave. We accomplish this by decomposing each GPR section that we then reconstruct without the first singular value, which corresponds mainly to the direct wave. We then take the difference of each section and the reference (taken before the initiation of the push-pull experiment), apply a time gain and finally use a Kirchhoff migration algorithm with a constant velocity model of $v = 0.12 \frac{m}{ns}$. This results in migrated GPR difference sections where the presence of the conductive tracer manifests itself as alternating (green-orange) stripes, whose horizontal extent is caused by the finite size of the source wavelet (Shakas et al., 2016). For visualization purposes, we suppress any reflections that are below the estimated noise level of our GPR dataset (computed as 15% of the maximum amplitude).

Figure 5.1 – Results from two separate push-pull experiments using either wethanalt or a dense saline tracer (experiments a and c in Table 5.1, respectively). The migrated GPR difference sections for (a-d) wethanalt and (e-h) dense saline tracers are presented at similar normalized acquisition times (τ), where the black circle corresponds to the tracer-injection location. The corresponding breakthrough curves are plotted in logarithmic scale (i) as a function of normalized time and normalized concentration (c). The resulting uncertainty due to the background salt concentration is indicated by the thickness of each curve.

5.4. Results

We now compare the BTCs and the migrated GPR difference sections obtained from the combined experiments with a saline tracer and wethanalt. Here, we consider both push-pull

Table 5.1 – Experimental parameters for: (a) push-pull and (b) push-wait-pull with wethanalt, (c) push-pull and (d) push-wait-pull with a saline tracer and (e) the fluorescein-based push-pull experiment by Kang et al. (2015).

ID	Tracer volume [L]	Tracer salinity [g kg^{-1}]	Ethanol [%]	Tracer density [kg m^{-3}]
a	106	40	22.73	1000
b	106	40	22.73	1000
c	100	44	0	1044
d	100	42	0	1042
e	1	0	0	1000
ID	Chaser volume [L]	Waiting time [min]	Pumping rate [L min^{-1}]	Mass recovery [%]
a	113	0	2.9	92 ± 3
b	108	120	2.9	78 ± 3
c	90	0	3.3	71 ± 9
d	90	227	3.3	50 ± 10
e	400	0	5	87

and push-wait-pull setups. For the BTCs, we use a normalized time, $\tau = t/t_{peak}$, where t corresponds to the time after the onset of pulling and t_{peak} is the theoretical peak arrival time. We also use a normalized concentration, $c = C/C_0$ that corresponds to the measured concentration (C) divided by the initial tracer concentration (C_0), after removing the background concentration from both. It takes about 3 minutes to acquire GPR data over the considered depth range, so each GPR section is indicated by an approximate time. The main experimental parameters are listed in Table 5.1.

A comparison between the push-pull experiments is made in Figure 5.1, where all time references are made (in normalized time) to the onset of the pulling phase. Figure 5.1 displays representative migrated GPR difference sections for the wethanalt (Figures 5.1a to 5.1d) and saline (Figures 5.1e to 5.1h) push-pull experiments, and the BTCs are plotted in Figure 5.1i. At the onset of pulling, the wethanalt tracer (Figure 5.1a) is localized within a depth range of 67 m to 72 m, while the saline tracer (Figure 5.1e) is found within 69 m to 76 m. At τ close to 0.25, the wethanalt tracer (Figure 5.1b) is found over the same depth range while the dense saline tracer (Figure 5.1f) has quickly migrated down towards the injection location. These results are in accordance with the peaks of the BTCs that occur with $\tau = 0.9$ and $c = 0.45$ for wethanalt, while $\tau = 0.27$ and $c = 0.23$ for the dense saline tracer. This indicates that the measured peak arrival is close to the theoretical peak when using wethanalt, while it is much smaller when using a dense saline tracer. Shakas et al. (2016) demonstrated through modeling that this early peak arrival of the dense saline tracer was a consequence of density effects and the geometry of the fracture network. Reflections from the wethanalt tracer remain visible, from 67 m to 77 m, at much later times (Figure 5.1d) than the peak arrival measured in the borehole.

The push-wait-pull experiments are presented in Figure 5.2. All migrated GPR difference sections shown were acquired during the waiting time, so their acquisition times are referenced
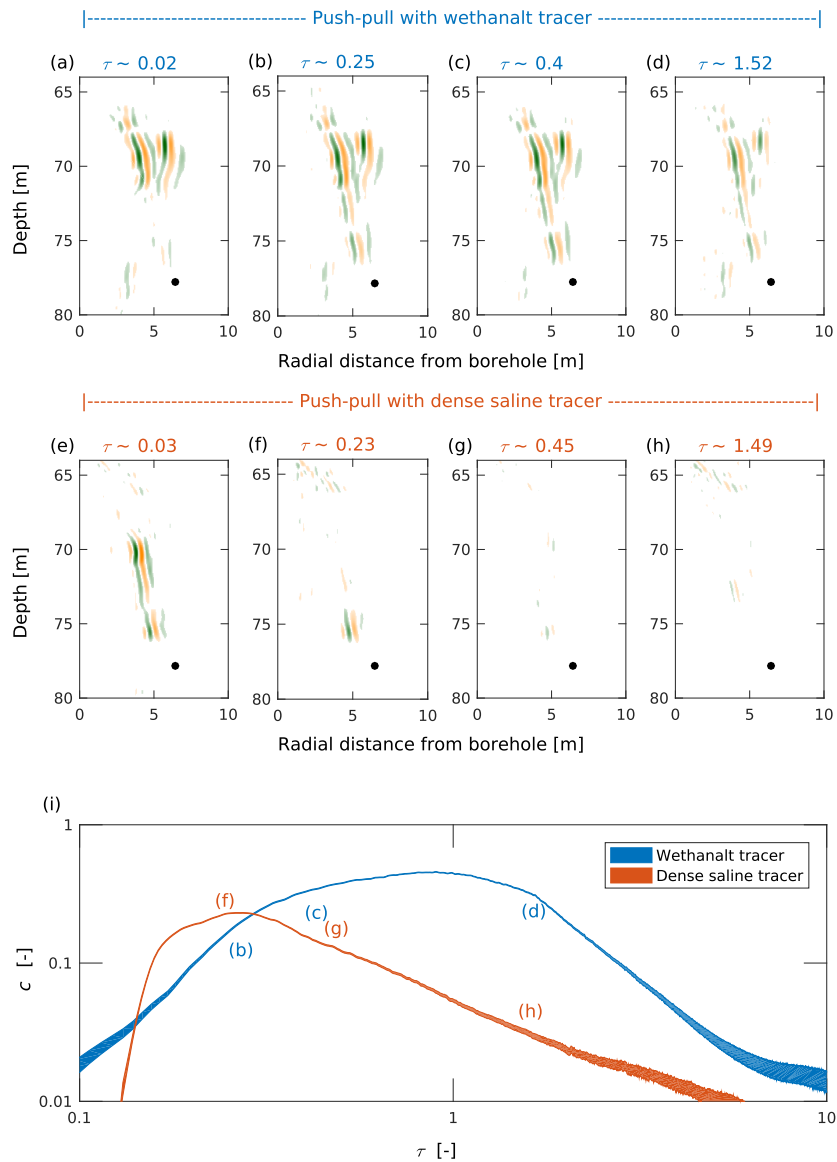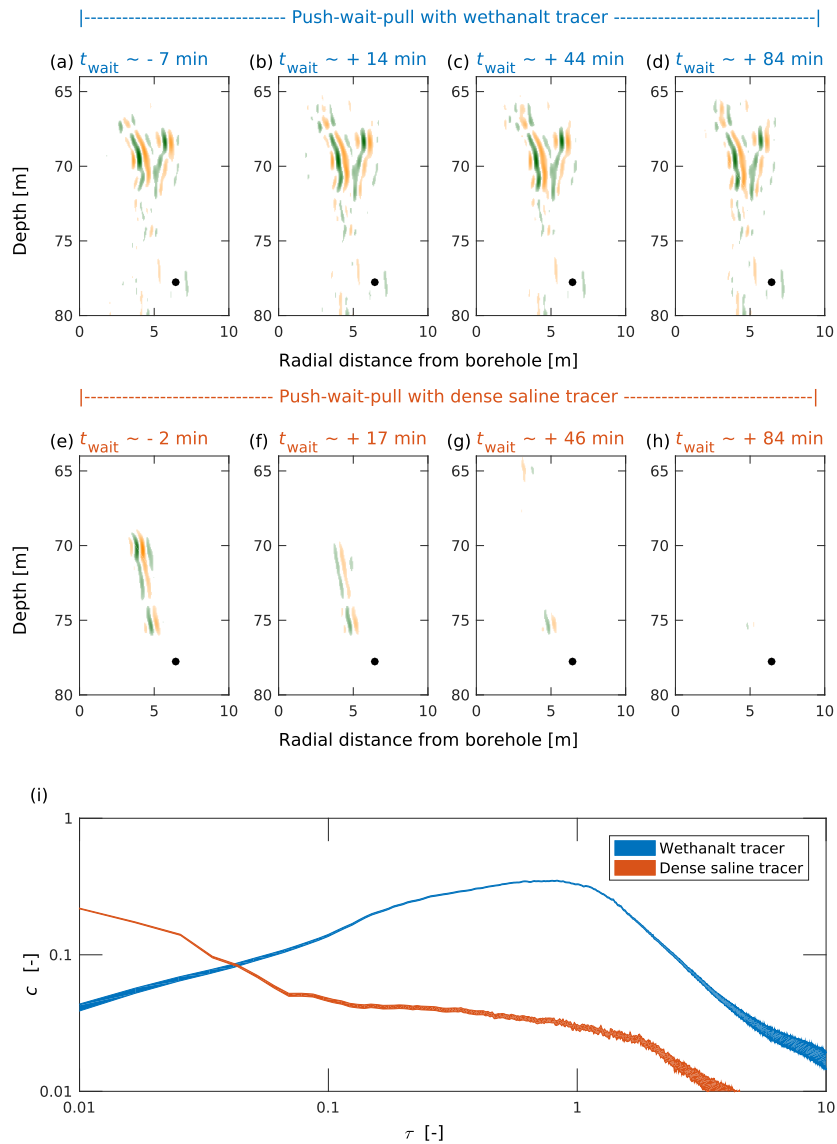
Figure 5.2 – Results from two separate push-wait-pull experiments using either wethanalt or a dense saline tracer (experiments b and d in Table 5.1, respectively). The migrated GPR difference sections for (a-d) wethanalt and (e-h) dense saline tracers are presented at similar acquisition times referenced from the waiting phase (t_{wait}), where the black circle corresponds to the tracer-injection location. The corresponding breakthrough curves are plotted in logarithmic scale (i) as a function of normalized concentration (c) and normalized time (τ) since the initiation of pulling. The resulting uncertainty due to the background salt concentration is indicated by the thickness of each curve.

in minutes from the onset of waiting (t_{wait}). After the pushing phase (Figures 5.2a and 5.2e), the distribution of both tracers is similar to the push-pull experiment (c.f., Figures 5.1a and 5.1e), thereby indicating a strong reproducibility of the experiments. After 17 minutes, the

saline tracer has sunk considerably (Figure 5.2f) due to its high density and is thereafter hardly detectable (Figures 5.2g and 5.2h). On the contrary, the migrated GPR difference sections for the wethanalt tracer remain almost identical during the whole waiting time (Figures 5.2a to 5.2d). Once more, the peak arrivals of the BTCs support these observations with $\tau = 0.83$ and $c = 0.35$ for wethanalt, while $\tau = 0.008$ and $c = 0.05$ for the dense saline tracer. Again, the peak arrival of the dense tracer occurs much earlier than predicted from the theoretical peak arrival time. Later GPR difference sections (not shown) confirm that the wethanalt tracer is still visible in the migrated GPR difference sections at times twice as long as the theoretical peak arrival.

5.5. Discussion

The migrated GPR difference sections of the two push-pull experiments (Figure 5.1) suggest that different spatial regions of the fractured system are probed when using a neutrally buoyant or a dense saline tracer. The saline tracer remains closer to the injection location and is not pushed much further by chasing. This is expected since we are trying to displace a dense tracer with lighter formation water. Moreover, it is also in accordance with flow and transport simulations (Shakas et al., 2016; Haaken et al., 2017). When wethanalt is used as a tracer, the chaser effectively pushes the tracer away from the injection location (Figure 5.1a) and into upper regions of the fractured system. By doing so, the migrated GPR difference sections from the wethanalt tracer probe an additional fracture that appears above 70 m depth and beyond 5 m radius (Figures 5.1a to 5.1d). This fracture is not present in the migrated GPR difference sections acquired with the dense saline tracer (Figures 5.1e to 5.1h).

In the push-wait-pull experiments (Figure 5.2), the impact of density is even more evident. While the tracer distribution after pushing is similar to their push-pull counterparts (compare Figures 5.1a with 5.2a and 5.1e with 5.2e), the dense saline tracer quickly migrates towards the injection location during the waiting period (Figures 5.2f to 5.2h). On the contrary, the wethanalt tracer provides consistent, high-amplitude reflections throughout the waiting period (Figures 5.2a to 5.2d), suggesting that the tracer distribution remains the same during this time. This indicates that the sinking observed when using a dense saline tracer is primarily due to density effects and not to ambient flow, as the ambient flow should also affect the wethanalt tracer. This finding is further supported by the similar peak arrival times of the wethanalt tracer in the push-pull and push-wait-pull configurations ($\tau = 0.9$ and $\tau = 0.83$ respectively). Nevertheless, the waiting period allows for more diffusion of the wethanalt tracer and possibly some ambient flow effects, that manifest as a decrease of the peak concentration in the BTC between the push-pull ($c = 0.45$) and push-wait-pull ($c = 0.35$) configurations.

To further assess the suitability of wethanalt as a neutrally-buoyant tracer, we compare our BTCs with the push-pull BTC by Kang et al. (2015), performed at the same fracture location but with an almost instantaneous injection of a neutrally-buoyant fluorescein tracer (see Table 5.1 for parameters). To remove the imprint of the injection period from the wethanalt BTCs, we model the push-pull experiment as the convolution of a linear, time-invariant
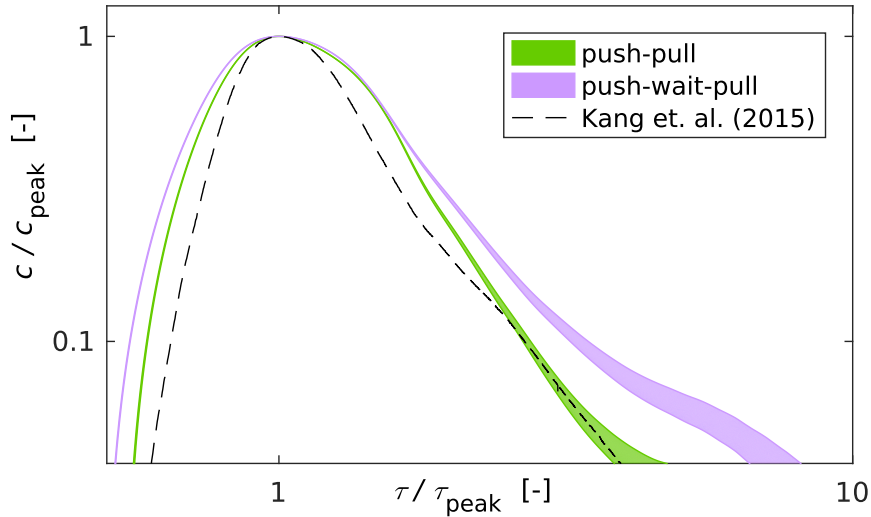
Figure 5.3 – Inferred impulse-response breakthrough curves for the wethanalt experiments (experiments a and b in Table 5.1) obtained by deconvolution. The uncertainty associated with the unknown background salinity is represented by the thickening of the lines at late times. For comparison purposes, we also plot the breakthrough curve from the push-pull experiment by Kang et al. (2015) described in Table 5.1.

source operator with the impulse response of the system. We infer the impulse-response using an iterative least-squares inversion (Menke, 2012) with smoothness and positivity constraints (Cirpka et al., 2007). Convergence is reached when the positivity constraints stop changing. In order to compare the late-time slope of the BTCs, we normalize concentration to the peak concentration and time to the peak arrival time, and plot the BTCs in Figure 5.3. The push-pull experiment shows a late-time tailing comparable to the BTC from Kang et al. (2015), while the push-wait-pull experiment indicates a smaller slope. This indicates that the wethanalt BTCs are consistent with the fluorescein BTCs, in particular regarding the late time concentration decay, which is important for investigating anomalous transport and dual domain mass transfer processes.

5.6. Conclusions

Our results suggest that wethanalt, a mixture of saline water and ethanol, is a suitable tracer for conducting geophysical monitoring using electrical or electromagnetic methods, when density effects are undesirable. Tracer test experiments conducted in push-pull and push-wait-pull configurations, in conjunction with single-hole GPR monitoring, confirm that wethanalt provides a strong GPR signal and does not exhibit the density-driven downward flow observed in our past experiments with dense saline tracers (Shakas et al., 2016). Therefore, wethanalt may significantly improve our ability to monitor flow and transport processes in-situ with hydrogeophysical methods, without the complications of density-driven flow and instabilities. Indeed, our results suggest that if a dense saline tracer is used, it is possible that

observations (and inferences) made about the hydrogeological system are unrepresentative of the ambient conditions and may differ significantly if a neutrally buoyant tracer is used instead. We also propose a practical way to prepare a wethanalt mixture with a high electrical conductivity at ambient density for any freshwater hydrogeological application. Additionally, wethanalt is bio-degradable, comparatively cheap to produce and does not pose any health risks. We anticipate that wethanalt or other neutrally-buoyant saline tracers will play an important role in advancing hydrogeophysics and in-situ monitoring of transport processes. Moreover, since the buoyancy of wethanalt can be adjusted, wethanalt mixtures open a new window on the use of buoyant and non-buoyant tracers for studying density effects.

Chapter 6

Conclusions

Characterizing rock fractures is a challenging, yet important task to assess and even predict subsurface processes in fractured media. The aperture heterogeneity of a fracture will largely determine its ability to act as a conduit for fluid flow and transport; still, measuring aperture heterogeneity in the field is an issue that is largely unresolved. Ground penetrating radar (GPR) is a geophysical tool that can be used to remotely image fractures at high resolution. However, the majority of GPR modeling studies do not address aperture heterogeneity mainly due to the inability of existing forward models to adequately simulate realistic fractures with varying aperture. Hydrological tracer tests are common in fractured media but provide spatially sparse data with limited information away from borehole wells. Combined hydro-geophysical experiments where a saline tracer test is imaged with GPR, or other electrical or electromagnetic (EM) methods offer a promising alternative. Nevertheless, the density effect associated with using a saline tracer for hydrogeophysics is rarely addressed. In this thesis we presented theoretical advances pertinent to modeling GPR in fractured rock where fractures have heterogeneous properties. We also presented experimental advances on the use of GPR to monitor push-pull tests and introduced a methodology for creating an electrically conductive but neutrally buoyant tracer. The latter is applicable for any hydrogeophysical application that uses EM and electric techniques to image a saline tracer.

6.1. Limitations and outlook

In Chapter 2 we introduced a forward model that can simulate the propagation of high-frequency EM waves in homogeneous media and their scattering from heterogeneous thin layers (e.g., fractures). The model, that we call effective-dipoles, utilizes analytic solutions for propagation and scattering but allows for arbitrary heterogeneous fracture properties by discretizing along the fracture plane. We reproduce results from a 3D numerical model and also laboratory GPR data from Grégoire and Hollender (2004) using the effective-dipoles models and a parametrized GPR source. Three current limitations of the effective-dipoles method are that (1) the rock matrix is homogeneous, (2) the fracture is fluid filled and (3) the fractures are planar (i.e., have no topography). The first limitation can be partly overcome if the rock matrix is mildly heterogeneous but isotropic, since the electric properties can be in this case taken as averages. Moreover, it can be argued that rock matrix heterogeneity plays

a limited role in time-lapse difference imaging since its effects are party suppressed during the differencing process. Alternatively, in the case of strong heterogeneity, EM time-reversal offers an alternative for target (i.e., fracture) detection (e.g., Liu et al., 2005). In the case where matrix diffusion is not negligible a trivial extension of the effective-dipoles model is to assume thin-bed properties where the volume of the rock matrix affected by diffusion together with the fracture filling are considered as an effective homogeneous medium. Another option is to use the (analytic) multi-layer equations to model the fracture as a three layer entity in a homogeneous matrix, where the two external layers correspond to the volume of the rock matrix affected by diffusion. The third limitation can be resolved by using an unstructured mesh for the fracture plane; in this case, the effective-dipoles formulation must be extended to account for the irregular geometry (e.g., the changing area of each cell). For an unstructured mesh to be theoretically valid with the current formulation, the discretization must be small enough so that constant fracture properties and an incoming plane wave can be assumed for each cell. Additionally, if fracture topography is modeled or if multiple fractures are considered, the importance of secondary reflections must be assessed by dipole coupling. Dipole coupling increases computation time but since the model is formulated in the frequency domain, it can be easily solved in parallel on multiple processors.

In Chapter 3 we used the analytic thin-bed model to infer the mean aperture of a fracture from synthetic GPR reflection data. The latter were computed with the effective-dipoles model and noise-contaminated while the fracture was characterized by a heterogeneous aperture distribution of varying Hurst exponent and cutoff-length. Using inverse modeling we showed that the thin-bed model, which assumes homogeneous fracture properties, will give meaningless results for the mean fracture aperture when aperture heterogeneity is fractal-like or occurs at small integral scales. Thin-bed inferred apertures are meaningful when the Hurst exponent is close to 1 and aperture changes occur over distances comparable to the Fresnel zone of the GPR signal. Laboratory and field evidence however suggests that fracture aperture is best described by small Hurst exponents and small scale heterogeneity. Aperture estimates inferred through inverse modeling with the thin-bed model must be therefore treated with caution and more robust estimates can be obtained by modeling fracture heterogeneity explicitly. Moreover, this study triggered interesting questions about the lower limit of GPR resolution, defined here as the smallest scatterer that can be accurately detected from reflection data. Resolution can be separated in the direction perpendicular (lateral) and parallel (range) to the propagating wave. GPR textbooks use wave interference principles to derive the lateral and range resolutions as fractions of the GPR signal dominant wavelength. However, fractures with apertures that are several orders of magnitude smaller than the dominant signal wavelength can still be visible in GPR data, as long as the contrast in electrical properties is strong enough to create a considerable reflection. In the latter case reflections from the two fracture surfaces may visually overlap but they are still informative of the aperture. Inferred aperture estimates can be quite reliable as long as a physical model, such as the thin bed model, can offer a valid approximation. As for the lateral resolution, the Fresnel zone does not account for the fact that GPR reflection data may contain higher-resolution information about lateral heterogeneities such as aperture channeling along the fracture plane. This happens because the analysis of lateral resolution using the Fresnel zone assumes a fracture as a homogeneous reflector. GPR reflection data resulting from a heterogeneous fracture may thus allow for lateral resolution below the Fresnel zone.

In Chapter 4 we presented the first-time imaging of a push-pull test with geophysical methods, namely time-lapse GPR difference imaging. In hydrology, push-pull tests are sometimes preferred because they offer insight on time-dependent processes such as matrix diffusion. Push-pull data are limited because they do not provide direct information about the spatial dynamics of the tracer, the scale of the experiment and ambient flow away from the borehole. Using a static GPR antenna setup we established a clear link between the push-pull BTC and the reflected electrical energy measured by the GPR system. With a moving antenna setup we successfully imaged the plume's position (hence the length scale of the experiment) and computed a mean plume velocity. We also showed, through experiments at different fractures and with different push-push setups, that the GPR reflections inform us about the number and orientation of the fractures occupied by the tracer, as well as density effects resulting from using a saline tracer. Conventional GPR systems are not sensitive to the angle of incidence of the reflected wave and only map fractures in two dimensions: the depth along the borehole and the travel distance of the emitted signal. When imaging a tracer test the tracer injection location is usually known and azimuthal ambiguity is reduced. Directional borehole GPR antenna systems offer a promising technological advancement but are not commercially available. Alternatively, if multiple boreholes are available and positioned favorably, single-hole measurements in several boreholes can increase the accuracy in resolving fracture orientation.

In Chapter 5 we presented a methodology for preparing a neutrally buoyant and electrically conductive tracer that we call wethanalt. Wethanalt is a mixture of saline water and ethanol which are fully miscible together, easy to prepare and calibrate in the field, relatively cheap, bio-degradable and non-toxic. Wethanalt can be used for any hydrogeophysical application that uses electrical and EM imaging techniques. We compared similar experiments performed with wethanalt and with (classical) saline tracers and showed that density effects are not negligible. In the former case, the BTC for wethanalt showed a later peak, different tailing behavior and resulted in larger mass recovery. GPR reflection data revealed very different dynamics between the saline tracer and wethanalt. With the latter we gained further insights into the strength of ambient flow and the presence of fractures that were not seen with the saline tracer experiments even though the push-pull test parameters were almost identical. However, the additional Ca molecules present in ethanol suggest that biological activity may be stimulated when wethanalt is used. Additionally, ethanol increases the viscosity of the tracer – in our experiments the viscosity approximately doubled when a tracer with 22.7% of ethanol was prepared. An increase in viscosity (and decrease in pumping rate) can lead to instabilities in the mixing front between wethanalt and water. The instabilities stabilize with time through molecular diffusion. When designing a wethanalt experiment an equilibrium between tracer viscosity and the experiment flow rates will ensure stable mixing. On the contrary, the enhanced biological activity and viscosity contrast may be desired in some cases. For example, bio-stimulation is a technique where nutrients are supplied to bacteria in the vadose zone in order to enhance their activity, and further enhance the bio-degradation of a contaminant (Höhener and Ponsin, 2014). Here, the increased viscosity is favorable because it will cause instabilities that enhance mixing and therefore speed up the bio-degradation process. Geophysical imaging can provide invaluable information about the spatial and temporal dynamics of such a process (McGlashan et al., 2012).

6.2. Perspectives

In this last short section, I deviate shortly from the use of 'we' and briefly state a few personal perspectives that I consider important for the continuing advancement of hydrogeophysics.

1. **Survey design:** The design of hydrogeophysical surveys is often based on expert knowledge and experience. However, fast and reliable models can be used to define optimal surveys in a deterministic (Maurer et al., 2010) or probabilistic (Chaloner and Verdinelli, 1995) manner. Currently, optimal survey design in geophysics is rarely applied and even when it is applied, the purpose is to increase the benefit (e.g., model parameter resolution) over the cost (e.g., number of measurements) of a survey. Another underutilized technique in geophysics is model selection; that is, using a dataset to discriminate between multiple conceptual models of the subsurface. Survey design can be used to complement model selection by defining the optimal survey that favors one conceptual model over another, and vice versa. Thus, experiments can be performed not in a generally optimal manner, but geared towards model selection.

2. **Decision making:** The majority of hydrogeophysical case studies are aimed for the scientific community, usually as proof-of-concept; for example to show that forward or inverse modeling provide sound results (Binley et al., 2015). The specialized and technical nature of published work makes it uninteresting or even impossible for the general public to comprehend. For example, the importance and impact of hydrogeophysics can be made more accessible to the general public through visual simulations. This will enable a wider application of hydrogeophysics for decision making, such as drilling groundwater wells by small scale water providers or on-site remediation of hazardous waste, the latter usually performed by government divisions. Moreover, approaches to decision making must account for uncertainty, as for example through the information gap decision theory (e.g., O'Malley and Vesselinov, 2014).

3. **Multiple scales:** Recent advances in multi-scale physics models (e.g., Jenny et al., 2003; Künze and Lunati, 2012a) enable simulations that simultaneously take into account varying properties and processes across several scales. Geophysical techniques are ideal to inform multi-scale physics models as different techniques can resolve properties at different scales (Rubin and Hubbard, 2005). For example, fracture properties can be inferred from borehole rock samples using X-ray tomography and from single-hole GPR imaging in the field. Natural properties often vary inherently across several scales and therefore fractal geometry can be used to establish the link between geophysical measurements and pave the way towards multi-scale geophysical modeling.

Bibliography

Adler, P. M. and J.-F. Thovert (1999). *Fractures and fracture networks*, Volume 15. Springer Science & Business Media.

Adler, P. M., J.-F. Thovert, and V. V. Mourzenko (2012). *Fractured porous media*. Oxford University Press.

Andričević, R. and V. Cvetković (1996). Evaluation of risk from contaminants migrating by groundwater. *Water Resources Research 32*(3), 611–621.

Archimedes (1987). *On floating bodies*. Cambridge University Press. Translation by H. T. Little, original text 250 BC.

Babcock, E. and J. H. Bradford (2015). Reflection waveform inversion of ground-penetrating radar data for characterizing thin and ultrathin layers of nonaqueous phase liquid contaminants in stratified media. *Geophysics 80*(2), H1–H11.

Ballenegger, V. C. and T. Weber (1999). The Ewald-Oseen extinction theorem and extinction lengths. *American Journal of Physics 67*(7), 599–605.

Bear, J. (1972). *Dynamics of fluids in porous media*. Dover Publications Inc.

Becker, M. W. and A. M. Shapiro (2000). Tracer transport in fractured crystalline rock: Evidence of nondiffusive breakthrough tailing. *Water Resources Research 36*(7), 1677–1686.

Becker, M. W. and A. M. Shapiro (2003). Interpreting tracer breakthrough tailing from different forced-gradient tracer experiment configurations in fractured bedrock. *Water Resources Research 39*(1).

Becker, M. W. and G. P. Tsoflias (2010). Comparing flux-averaged and resident concentration in a fractured bedrock using ground penetrating radar. *Water Resources Research 46*(9).

Beff, L., T. Günther, B. Vandoorne, V. Couvreur, and M. Javaux (2013). Three-dimensional monitoring of soil water content in a maize field using Electrical Resistivity Tomography. *Hydrology and Earth System Sciences 17*(2), 595–609.

Beinhorn, M., P. Dietrich, and O. Kolditz (2005). 3-D numerical evaluation of density effects on tracer tests. *Journal of Contaminant Hydrology 81*(1), 89–105.

Belfield, W. C. (1994). Multifractal characteristics of natural fracture apertures. *Geophysical Research Letters 21*(24), 2641–2644.

Belghoul, A. (2007). *Caractérisation pétrophysique et hydrodynamique du socle cristallin.* Ph. D. thesis, Université Montpellier II-Sciences et Techniques du Languedoc.

Bergmann, T., J. O. Robertsson, and K. Holliger (1998). Finite-difference modeling of electromagnetic wave propagation in dispersive and attenuating media. *Geophysics 63*(3), 856–867.

Berkowitz, B. (2002). Characterizing flow and transport in fractured geological media: A review. *Advances in Water Resources 25*(8), 861–884.

Binley, A., S. S. Hubbard, J. A. Huisman, A. Revil, D. A. Robinson, K. Singha, and L. D. Slater (2015). The emergence of hydrogeophysics for improved understanding of subsurface processes over multiple scales. *Water Resources Research 51*(6), 3837–3866.

Birken, R. and R. Versteeg (2000). Use of four-dimensional ground penetrating radar and advanced visualization methods to determine subsurface fluid migration. *Journal of Applied Geophysics 43*(2), 215–226.

Bodin, J., F. Delay, and G. De Marsily (2003). Solute transport in a single fracture with negligible matrix permeability: 1. fundamental mechanisms. *Hydrogeology Journal 11*(4), 418–433.

Boisson, A., P. De Anna, O. Bour, T. Le Borgne, T. Labasque, and L. Aquilina (2013). Reaction chain modeling of denitrification reactions during a push-pull test. *Journal of Contaminant Hydrology 148*, 1–11.

Bonnet, E., O. Bour, N. E. Odling, P. Davy, I. Main, P. Cowie, and B. Berkowitz (2001). Scaling of fracture systems in geological media. *Reviews of Geophysics 39*(3), 347–383.

Born, M. and E. Wolf (1999). *Principles of optics: Electromagnetic theory of propagation, interference and diffraction of light*, Volume 7. Cambridge University Press.

Bour, O., P. Davy, C. Darcel, and N. Odling (2002). A statistical scaling model for fracture network geometry, with validation on a multiscale mapping of a joint network (Hornelen Basin, Norway). *Journal of Geophysical Research: Solid Earth 107*(B6).

Boy, J.-P., L. Longuevergne, F. Boudin, T. Jacob, F. Lyard, M. Llubes, N. Florsch, and M.-F. Esnoult (2009). Modelling atmospheric and induced non-tidal oceanic loading contributions to surface gravity and tilt measurements. *Journal of Geodynamics 48*(3), 182–188.

Brace, W. F. (1984). Permeability of crystalline rocks: New in situ measurements. *Journal of Geophysical Research: Solid Earth 89*(B6), 4327–4330.

Bradford, J. H. and J. C. Deeds (2006). Ground-penetrating radar theory and application of thin-bed offset-dependent reflectivity. *Geophysics 71*(3), K47–K57.

Broadbent, S. R. and J. M. Hammersley (1957). Percolation processes: I. crystals and mazes. *Mathematical Proceedings of the Cambridge Philosophical Society 53*(3), 629–641.

Brown, S. R. (1987). Fluid flow through rock joints: The effect of surface roughness. *Journal of Geophysical Research: Solid Earth 92*(B2), 1337–1347.

Brown, S. R., R. L. Kranz, and B. P. Bonner (1986). Correlation between the surfaces of natural rock joints. *Geophysical Research Letters 13*(13), 1430–1433.

Brunetti, C., N. Linde, and J. A. Vrugt (2017). Bayesian model selection in hydrogeophysics: Application to conceptual subsurface models of the South Oyster Bacterial Transport Site, Virginia, USA. *Advances in Water Resources 102*, 127–141.

Brush, D. J. and N. R. Thomson (2003). Fluid flow in synthetic rough-walled fractures: Navier-Stokes, Stokes, and local cubic law simulations. *Water Resources Research 39*(4). 1085.

Cacas, M., E. Ledoux, G. de Marsily, A. Barbreau, P. Calmels, B. Gaillard, and R. Margritta (1990). Modeling fracture flow with a stochastic discrete fracture network: Calibration and validation: 2. the transport model. *Water Resources Research 26*(3), 491–500.

Cacas, M., E. Ledoux, G. d. Marsily, B. Tillie, A. Barbreau, E. Durand, B. Feuga, and P. Peaude-cerf (1990). Modeling fracture flow with a stochastic discrete fracture network: Calibration and validation: 1. the flow model. *Water Resources Research 26*(3), 479–489.

Chaloner, K. and I. Verdinelli (1995). Bayesian experimental design: A review. *Statistical Science*, 273–304.

Chui, J. Y., P. de Anna, and R. Juanes (2015). Interface evolution during radial miscible viscous fingering. *Physical Review E 92*(4), 041003.

Cirpka, O. A., M. N. Fienen, M. Hofer, E. Hoehn, A. Tessarini, R. Kipfer, and P. K. Kitanidis (2007). Analyzing bank filtration by deconvoluting time series of electric conductivity. *Ground Water 45*(3), 318–328.

Cvetković, V. and A. Frampton (2012). Solute transport and retention in three-dimensional fracture networks. *Water Resources Research 48*(2).

Cvetković, V., S. Painter, N. Outters, and J. Selroos (2004). Stochastic simulation of radionu-clide migration in discretely fractured rock near the Äspö Hard Rock Laboratory. *Water Resources Research 40*(2).

Day-Lewis, F. D., J. W. Lane, J. M. Harris, and S. M. Gorelick (2003). Time-lapse imaging of saline-tracer transport in fractured rock using difference-attenuation radar tomography. *Water Resources Research 39*(10).

de Dreuzy, J.-R., P. Davy, and O. Bour (2001a). Hydraulic properties of two-dimensional random fracture networks following a power law length distribution: 1. effective connectivity. *Water Resources Research 37*(8), 2065–2078.

de Dreuzy, J.-R., P. Davy, and O. Bour (2001b). Hydraulic properties of two-dimensional random fracture networks following a power law length distribution 2. permeability of networks based on lognormal distribution of apertures. *Water Resources Research 37*(8), 2079–2095.

de Dreuzy, J.-R., P. Davy, and O. Bour (2002). Hydraulic properties of two-dimensional random fracture networks following power law distributions of length and aperture. *Water Resources Research 38*(12).

de Dreuzy, J.-R., Y. Méheust, and G. Pichot (2012). Influence of fracture scale heterogeneity on the flow properties of three-dimensional discrete fracture networks (DFN). *Journal of Geophysical Research: Solid Earth 117*(B11).

Deparis, J. and S. Garambois (2008). On the use of dispersive APVO GPR curves for thin-bed properties estimation: Theory and application to fracture characterization. *Geophysics 74*(1), J1–J12.

Diamanti, N. and A. Giannopoulos (2009). Implementation of ADI-FDTD subgrids in ground penetrating radar FDTD models. *Journal of Applied Geophysics 67*(4), 309–317.

Doetsch, J., N. Linde, T. Vogt, A. Binley, and A. G. Green (2012). Imaging and quantifying salt-tracer transport in a riparian groundwater system by means of 3D ERT monitoring. *Geophysics 77*(5), B207–B218.

Dorn, C., N. Linde, J. Doetsch, T. Le Borgne, and O. Bour (2012). Fracture imaging within a granitic rock aquifer using multiple-offset single-hole and cross-hole GPR reflection data. *Journal of Applied Geophysics 78*, 123–132.

Dorn, C., N. Linde, T. Le Borgne, O. Bour, and L. Baron (2011). Single-hole GPR reflection imaging of solute transport in a granitic aquifer. *Geophysical Research Letters 38*(8).

Dorn, C., N. Linde, T. Le Borgne, O. Bour, and J.-R. de Dreuzy (2013). Conditioning of stochastic 3-D fracture networks to hydrological and geophysical data. *Advances in Water Resources 62*, 79–89.

Dorn, C., N. Linde, T. Le Borgne, O. Bour, and M. Klepikova (2012). Inferring transport characteristics in a fractured rock aquifer by combining single-hole ground-penetrating radar reflection monitoring and tracer test data. *Water Resources Research 48*(11).

Dverstorp, B. and J. Andersson (1989). Application of the discrete fracture network concept with field data: Possibilities of model calibration and validation. *Water Resources Research 25*(3), 540–550.

Dverstorp, B., J. Andersson, and W. Nordqvist (1992). Discrete fracture network interpretation of field tracer migration in sparsely fractured rock. *Water Resources Research 28*(9), 2327–2343.

Erhel, J., J.-R. de Dreuzy, A. Beaudoin, E. Bresciani, and D. Tromeur-Dervout (2009). A parallel scientific software for heterogeneous hydrogeoloy. *Parallel Computational Fluid Dynamics*, 39–48.

Ernst, J. R., A. G. Green, H. Maurer, and K. Holliger (2007). Application of a new 2D time-domain full-waveform inversion scheme to crosshole radar data. *Geophysics 72*(5), J53–J64.

Ernst, J. R., K. Holliger, H. Maurer, and A. G. Green (2006). Realistic fdtd modelling of borehole georadar antenna radiation: methodolgy and application. *Near Surface Geophysics 4*(1), 19–30.

Falgàs, E., J. Ledo, A. Marcuello, and P. Queralt (2009). Monitoring freshwater-seawater interface dynamics with audiomagnetotelluric data. *Near Surface Geophysics 7*(5-6), 391–399.

Faybishenko, B., P. A. Witherspoon, and J. E. Gale (2005). Dynamics of fluids and transport in fractured rock.

Fearn, H., D. F. James, and P. W. Milonni (1996). Microscopic approach to reflection, transmission, and the Ewald-Oseen extinction theorem. *American Journal of Physics 64*(8), 986–995.

Ferré, T., L. Bentley, A. Binley, N. Linde, A. Kemna, K. Singha, K. Holliger, J. A. Huisman, and B. Minsley (2009). Critical steps for the continuing advancement of hydrogeophysics. *Eos, Transactions American Geophysical Union 90*(23), 200–200.

Feynman, R. P., R. B. Leighton, and M. Sands (1964). *The Feynman lectures on physics: Mainly electromagnetism and matter.* Addison-Wesley.

Fiori, A. and M. W. Becker (2015). Power law breakthrough curve tailing in a fracture: The role of advection. *Journal of Hydrology 525*, 706–710.

Fisher, Y., M. McGuire, R. F. Voss, M. F. Barnsley, R. L. Devaney, and B. B. Mandelbrot (2012). *The science of fractal images.* Springer Science & Business Media.

FOEN (2009). Sustainable protection of groundwater. Technical Report UD-1003-E.

Garré, S., M. Javaux, J. Vanderborght, H. Vereecken, et al. (2011). Three-dimensional electrical resistivity tomography to monitor root zone water dynamics. *Vadose Zone Journal 10*(1), 412–424.

Ge, S. (1997). A governing equation for fluid flow in rough fractures. *Water Resources Research 33*(1), 53–61.

Giannopoulos, A. (2005). Modelling ground penetrating radar by GprMax. *Construction and building materials 19*(10), 755–762.

Gouze, P., T. Le Borgne, R. Leprovost, G. Lods, T. Poidras, and P. Pezard (2008). Non-Fickian dispersion in porous media: 1. Multiscale measurements using single-well injection withdrawal tracer tests. *Water Resources Research 44*(6).

Grandjean, G. and J.-C. Gourry (1996). GPR data processing for 3D fracture mapping in a marble quarry (Thassos, Greece). *Journal of Applied Geophysics 36*(1), 19–30.

Grasmueck, M. (1996). 3-D ground-penetrating radar applied to fracture imaging in gneiss. *Geophysics 61*(4), 1050–1064.

Grégoire, C. and F. Hollender (2004). Discontinuity characterization by the inversion of the spectral content of ground penetrating radar (GPR) reflections-Application of the Jonscher model. *Geophysics 69*(6), 1414–1424.

Grobbe, N. and E. Slob (2016). Seismo-electromagnetic thin-bed responses: Natural signal enhancements? *Journal of Geophysical Research: Solid Earth 121*(4), 2460–2479.

Haaken, K., G. P. Deidda, G. Cassiani, R. Deiana, M. Putti, C. Paniconi, C. Scudeler, and A. Kemna (2017). Flow dynamics in hyper-saline aquifers: hydro-geophysical monitoring and modeling. *Hydrology and Earth System Sciences 21*(3), 1439.

Haggerty, R., S. A. McKenna, and L. C. Meigs (2000). On the late-time behavior of tracer test breakthrough curves. *Water Resources Research 36*(12), 3467–3479.

Hammond, C. (2016). CRC handbook of Chemistry and Physics, 2015-2016.

Hansen, S. K., B. Berkowitz, V. V. Vesselinov, D. O'Malley, and S. Karra (2016). Push-pull tracer tests: Their information content and use for characterizing non-Fickian, mobile-immobile behavior. *Water Resources Research 52*(12), 9565–9585.

Höhener, P. and V. Ponsin (2014). In situ vadose zone bioremediation. *Current opinion in biotechnology 27*, 1–7.

Hollender, F. and S. Tillard (1998). Modeling ground-penetrating radar wave propagation and reflection with the Jonscher parameterization. *Geophysics 63*(6), 1933–1942.

Hubbard, S. S. and N. Linde (2011). *Hydrogeophysics, in S. Uhlenbrook (Ed.) Treatise on Water*, Volume 2. Elsevier.

Hubbert, M. K. (1940). The theory of ground-water motion. *The Journal of Geology 48*(8, Part 1), 785–944.

Hurst, H. E. (1951). Long-term storage capacity of reservoirs. *Transactions of the American Society of Civil Engineering 116*, 770–808.

Hyman, J. D., S. Karra, N. Makedonska, C. W. Gable, S. L. Painter, and H. S. Viswanathan (2015). dfnworks: A discrete fracture network framework for modeling subsurface flow and transport. *Computers & Geosciences 84*, 10–19.

Ishibashi, T., N. Watanabe, N. Hirano, A. Okamoto, and N. Tsuchiya (2012). Geoflow: A novel model simulator for prediction of the 3-d channeling flow in a rock fracture network. *Water Resources Research 48*(7).

Ishibashi, T., N. Watanabe, N. Hirano, A. Okamoto, and N. Tsuchiya (2015). Beyond-laboratory-scale prediction for channeling flows through subsurface rock fractures with heterogeneous aperture distributions revealed by laboratory evaluation. *Journal of Geophysical Research: Solid Earth 120*(1), 106–124.

Istok, J. D. (2012). *Push-pull tests for site characterization.* Springer-Verlag Berlin Heidelberg.

Istok, J. D. and M. D. Humphrey (1995). Laboratory investigation of buoyancy-induced flow (plume sinking) during two-well tracer tests. *Ground Water 33*(4), 597–604.

Jackson, J. D. and R. F. Fox (1999). Classical electrodynamics. *American Journal of Physics 67*(9), 841–842.

Jeannin, M., S. Garambois, C. Grégoire, and D. Jongmans (2006). Multiconfiguration GPR measurements for geometric fracture characterization in limestone cliffs (Alps). *Geophysics 71*(3), B85–B92.

Jenny, P., S. Lee, and H. Tchelepi (2003). Multi-scale finite-volume method for elliptic problems in subsurface flow simulation. *Journal of Computational Physics 187*(1), 47–67.

Jol, H. M. (2008). *Ground penetrating radar theory and applications.* Elsevier.

Jonscher, A. K. (1999). Dielectric relaxation in solids. *Journal of Physics D: Applied Physics 32*(14), R57.

Kahnert, F. M. (2003). Numerical methods in electromagnetic scattering theory. *Journal of Quantitative Spectroscopy and Radiative Transfer 79*, 775–824.

Kang, P. K., T. Le Borgne, M. Dentz, O. Bour, and R. Juanes (2015). Impact of velocity correlation and distribution on transport in fractured media: Field evidence and theoretical model. *Water Resources Research 51*(2), 940–959.

Keller, A. A., P. V. Roberts, and M. J. Blunt (1999). Effect of fracture aperture variations on the dispersion of contaminants. *Water Resources Research 35*(1), 55–63.

Kemna, A., J. Vanderborght, B. Kulessa, and H. Vereecken (2002). Imaging and characterisation of subsurface solute transport using electrical resistivity tomography (ERT) and equivalent transport models. *Journal of Hydrology 267*(3), 125–146.

Kiefer, J. (1953). Sequential minimax search for a maximum. *Proceedings of the American mathematical society 4*(3), 502–506.

Kilburn, C. R. and B. Voight (1998). Slow rock fracture as eruption precursor at Soufriere Hills volcano, Montserrat. *Geophysical Research Letters 25*(19), 3665–3668.

Klepikova, M. V., T. Le Borgne, O. Bour, K. Gallagher, R. Hochreutener, and N. Lavenant (2014). Passive temperature tomography experiments to characterize transmissivity and connectivity of preferential flow paths in fractured media. *Journal of Hydrology 512*, 549–562.

Klotzsche, A., J. van der Kruk, N. Linde, J. Doetsch, and H. Vereecken (2013). 3-D characterization of high-permeability zones in a gravel aquifer using 2-D crosshole GPR full-waveform inversion and waveguide detection. *Geophysical Journal International 195*(2), 932–944.

Konzuk, J. S. and B. H. Kueper (2004). Evaluation of cubic law based models describing single-phase flow through a rough-walled fracture. *Water Resources Research 40*(2).

Künze, R. and I. Lunati (2012a). An adaptive multiscale method for density-driven instabilities. *Journal of Computational Physics 231*(17), 5557–5570.

Künze, R. and I. Lunati (2012b). MaFloT-matlab flow and transport. *Published under the GNU licence agreement on www.maflot.com.*

Lai, H., Y. Lau, and W. Wong (2002). Understanding wave characteristics via linear superposition of retarded fields. *American Journal of Physics 70*(2), 173–179.

Lanaro, F. (2000). A random field model for surface roughness and aperture of rock fractures. *International Journal of Rock Mechanics and Mining Sciences 37*(8), 1195–1210.

Lane, J., M. L. Buursink, F. Haeni, and R. Versteeg (2000). Evaluation of ground-penetrating radar to detect free-phase hydrocarbons in fractured rocks—results of numerical modeling and physical experiments. *Ground Water 38*(6), 929–938.

Lane, J. W., R. Knight, and B. Minsley (2016). Introduction to this special section: Hydrogeophysics. *The Leading Edge 35*(9), 750–751.

Le Borgne, T., O. Bour, J. De Dreuzy, P. Davy, and F. Touchard (2004). Equivalent mean flow models for fractured aquifers: Insights from a pumping tests scaling interpretation. *Water Resources Research 40*(3).

Le Borgne, T., O. Bour, F. Paillet, and J.-P. Caudal (2006). Assessment of preferential flow path connectivity and hydraulic properties at single-borehole and cross-borehole scales in a fractured aquifer. *Journal of Hydrology 328*(1), 347–359.

Le Borgne, T., O. Bour, M. Riley, P. Gouze, P. Pezard, A. Belghoul, G. Lods, R. Le Provost, R. Greswell, P. Ellis, et al. (2007). Comparison of alternative methodologies for identifying and characterizing preferential flow paths in heterogeneous aquifers. *Journal of Hydrology 345*(3), 134–148.

Le Borgne, T. and P. Gouze (2008). Non-Fickian dispersion in porous media: 2. Model validation from measurements at different scales. *Water Resources Research 44*(6).

Leary, P. (1991). Deep borehole log evidence for fractal distribution of fractures in crystalline rock. *Geophysical Journal International 107*(3), 615–627.

Lee, C.-H. and I. W. Farmer (1993). *Fluid flow in discontinuous rocks.* Chapman & Hall.

Lee, S. H., K.-K. Lee, and I. W. Yeo (2014). Assessment of the validity of stokes and reynolds equations for fluid flow through a rough-walled fracture with flow imaging. *Geophysical Research Letters 41*(13), 4578–4585.

Leibundgut, C., P. Maloszewski, and C. Külls (2011). *Tracers in hydrology.* John Wiley & Sons.

Lessoff, S. C. and L. F. Konikow (1997). Ambiguity in measuring matrix diffusion with single-well injection/recovery tracer tests. *Groundwater 35*(1), 166–176.

Leucci, G., R. Persico, and F. Soldovieri (2007). Detection of fractures from GPR data: the case history of the Cathedral of Otranto. *Journal of Geophysics and Engineering 4*(4), 452.

Linde, N. (2014). Falsification and corroboration of conceptual hydrological models using geophysical data. *Wiley Interdisciplinary Reviews: Water 1*(2), 151–171.

Liu, D., G. Kang, L. Li, Y. Chen, S. Vasudevan, W. Joines, Q. H. Liu, J. Krolik, and L. Carin (2005). Electromagnetic time-reversal imaging of a target in a cluttered environment. *IEEE transactions on antennas and propagation 53*(9), 3058–3066.

Liu, L. (2006). Fracture characterization using borehole radar: Numerical modeling. *Water, Air, & Soil Pollution: Focus 6*(1-2), 17.

Long, J. C. S., J. S. Remer, C. R. Wilson, and P. A. Witherspoon (1982). Porous media equivalents for networks of discontinuous fractures. *Water Resources Research 18*(3), 645–658.

Lorentz, H. A. (1909). *The theory of electrons and its applications to the phenomena of light and radiant heat*, Volume 29. Columbia University Press.

Lunati, I., W. Kinzelbach, and I. Sørensen (2003). Effects of pore volume-transmissivity correlation on transport phenomena. *Journal of Contaminant Hydrology 67*(1), 195–217.

Mandelbrot, B. B. (1975). Stochastic models for the Earth's relief, the shape and the fractal dimension of the coastlines, and the number-area rule for islands. *Proceedings of the National Academy of Sciences 72*(10), 3825–3828.

Mandelbrot, B. B. (1982). *The Fractal geometry of Nature*. WH Freedman and Co.

Mandelbrot, B. B. (1985). Self-affine fractals and fractal dimension. *Physica scripta 32*(4), 257.

Mandelbrot, B. B. (1989). Multifractal measures, especially for the geophysicist. *Pure and Applied Geophysics 131*(1-2), 5–42.

Marçais, J., J.-R. De Dreuzy, T. Ginn, P. Rousseau-Gueutin, and S. Leray (2015). Inferring transit time distributions from atmospheric tracer data: Assessment of the predictive capacities of Lumped Parameter Models on a 3D crystalline aquifer model. *Journal of Hydrology 525*, 619–631.

Maurer, H., A. Curtis, and D. E. Boerner (2010). Recent advances in optimized geophysical survey design. *Geophysics 75*(5), 75A177–75A194.

McGlashan, M., G. Tsoflias, P. Schillig, J. Devlin, and J. Roberts (2012). Field gpr monitoring of biostimulation in saturated porous media. *Journal of Applied Geophysics 78*, 102–112.

Menke, W. (2012). *Geophysical data analysis: Discrete inverse theory*, Volume 45. Academic Press.

Michalski, K. A. and D. Zheng (1990). Electromagnetic scattering and radiation by surfaces of arbitrary shape in layered media. i. Theory. *IEEE Transactions on Antennas and propagation 38*(3), 335–344.

Moorkamp, M., P. G. Lelièvre, N. Linde, and A. Khan (2016). *Integrated imaging of the earth: Theory and applications*, Volume 218. John Wiley & Sons.

Moreno, L., C.-F. Tsang, Y. Tsang, and I. Neretnieks (1990). Some anomalous features of flow and solute transport arising from fracture aperture variability. *Water Resources Research 26*(10), 2377–2391.

Moreno, L., Y. Tsang, C. Tsang, F. Hale, and I. Neretnieks (1988). Flow and tracer transport in a single fracture: A stochastic model and its relation to some field observations. *Water Resources Research 24*(12), 2033–2048.

Mukherjee, S. and M. E. Everett (2011). 3D controlled-source electromagnetic edge-based finite element modeling of conductive and permeable heterogeneities. *Geophysics 76*(4), F215–F226.

Nabighian, M. N. (1991). *Electromagnetic methods in applied geophysics*, Volume 2. Society of Exploration Geophysicists.

Neretnieks, I. (2007). Single well injection withdrawal tests (SWIW) in fractured rock: Some aspects on interpretation.

Neuman, S. P. (2005). Trends, prospects and challenges in quantifying flow and transport through fractured rocks. *Hydrogeology Journal 13*(1), 124–147.

Nordqvist, A. W., Y. Tsang, C. Tsang, B. Dverstorp, and J. Andersson (1992). A variable aperture fracture network model for flow and transport in fractured rocks. *Water Resources Research 28*(6), 1703–1713.

Nordqvist, R. and E. Gustafsson (2002). Single-well injection-withdrawal tests (SWIW). Literature review and scoping calculations for homogeneous crystalline bedrock conditions. Technical report, Swedish Nuclear Fuel and Waste Management Co.

Novakowski, K. S., G. V. Evans, D. A. Lever, and K. G. Raven (1985). A field example of measuring hydrodynamic dispersion in a single fracture. *Water Resources Research 21*(8), 1165–1174.

NRC (1996). *Rock fractures and fluid flow: Contemporary understanding and applications*. National Academies Press.

Odling, N. (1994). Natural fracture profiles, fractal dimension and joint roughness coefficients. *Rock Mechanics and Rock Engineering 27*(3), 135–153.

Odling, N. E. (1997). Scaling and connectivity of joint systems in sandstones from western Norway. *Journal of Structural Geology 19*(10), 1257–1271.

Olsson, O., L. Falk, O. Forslund, L. Lundmark, and E. Sandberg (1992). Borehole radar applied to the characterization of hydraulically conductive fracture zones in crystalline rock. *Geophysical Prospecting 40*(2), 109–142.

Orfanidis, S. J. (2002). *Electromagnetic waves and antennas*. Rutgers University New Brunswick, NJ.

Oron, A. P. and B. Berkowitz (1998). Flow in rock fractures: The local cubic law assumption reexamined. *Water Resources Research 34*(11), 2811–2825.

O'Malley, D. and V. V. Vesselinov (2014). Groundwater remediation using the information gap decision theory. *Water Resources Research 50*, 246–256.

Parkhomenko, E. I. (2012). *Electrical properties of rocks*. Springer Science & Business Media.

Pasquet, S., L. Bodet, L. Longuevergne, A. Dhemaied, C. Camerlynck, F. Rejiba, and R. Guérin (2015). 2D characterization of near-surface VP/VS: surface-wave dispersion inversion versus refraction tomography. *Near Surface Geophysics 13*(4), 315–331.

Patriarca, C., S. Lambot, M. Mahmoudzadeh, J. Minet, and E. Slob (2011). Reconstruction of sub-wavelength fractures and physical properties of masonry media using full-waveform inversion of proximal penetrating radar. *Journal of Applied Geophysics 74*(1), 26–37.

Pearce, J. and D. Mittleman (2002). Defining the Fresnel zone for broadband radiation. *Physical Review E 66*(5).

Peeters, D. and P. Huyskens (1993). Endothermicity or exothermicity of water/alcohol mixtures. *Journal of Molecular Structure 300*, 539–550.

Peterson, Jr, J. E. (2001). Pre-inversion corrections and analysis of radar tomographic data. *Journal of Environmental & Engineering Geophysics 6*(1), 1–18.

Poon, C., R. Sayles, and T. Jones (1992). Surface measurement and fractal characterization of naturally fractured rocks. *Journal of Physics D: Applied Physics 25*(8), 1269.

Porsani, J. L., W. A. Sauck, and A. O. Júnior (2006). Gpr for mapping fractures and as a guide for the extraction of ornamental granite from a quarry: A case study from southern Brazil. *Journal of Applied Geophysics 58*(3), 177–187.

Purcell, E. M. (2011). *Electricity and magnetism.* Cambridge University Press.

Purcell, E. M. and C. R. Pennypacker (1973). Scattering and absorption of light by nonspherical dielectric grains. *The Astrophysical Journal 186*, 705–714.

Pyrak-Nolte, L. J., N. G. W. Cook, and D. D. Nolte (1988). Fluid percolation through single fractures. *Geophysical Research Letters 15*(11), 1247–1250.

Qian, J., Z. Chen, H. Zhan, and H. Guan (2011). Experimental study of the effect of roughness and Reynolds number on fluid flow in rough-walled single fractures: A check of local cubic law. *Hydrological Processes 25*(4), 614–622.

Ramirez, A. and R. Lytle (1986). Investigation of fracture flow paths using alterant geophysical tomography. In *International Journal of Rock Mechanics and Mining Sciences & Geomechanics Abstracts*, Volume 23, pp. 165–169. Elsevier.

Read, T., O. Bour, V. Bense, T. Le Borgne, P. Goderniaux, M. Klepikova, R. Hochreutener, N. Lavenant, and V. Boschero (2013). Characterizing groundwater flow and heat transport in fractured rock using fiber-optic distributed temperature sensing. *Geophysical Research Letters 40*(10), 2055–2059.

Read, T., O. Bour, J. S. Selker, V. F. Bense, T. L. Borgne, R. Hochreutener, and N. Lavenant (2014). Active-distributed temperature sensing to continuously quantify vertical flow in boreholes. *Water Resources Research 50*(5), 3706–3713.

Renshaw, C. E. (1995). On the relationship between mechanical and hydraulic apertures in rough-walled fractures. *Journal of Geophysical Research: Solid Earth 100*(B12), 24629–24636.

Rosas-Carbajal, M., N. Linde, J. Peacock, F. Zyserman, T. Kalscheuer, and S. Thiel (2015). Probabilistic 3-D time-lapse inversion of magnetotelluric data: Application to an enhanced geothermal system. *Geophysical Journal International 203*(3), 1946–1960.

Rubin, Y. and S. S. Hubbard (2005). *Hydrogeophysics*, Volume 50. Springer Science & Business Media.

Ruelleu, S., F. Moreau, O. Bour, D. Gapais, and G. Martelet (2010). Impact of gently dipping discontinuities on basement aquifer recharge: An example from Ploemeur (Brittany, France). *Journal of Applied Geophysics 70*(2), 161–168.

Russakoff, G. (1970). A derivation of the macroscopic Maxwell equations. *American Journal of Physics 38*(10), 1188–1195.

Sambuelli, L. and C. Calzoni (2010). Estimation of thin fracture aperture in a marble block by GPR sounding. *Bollettino di Geofisica Teorica ed Applicata 51*(2-3), 239–252.

Sassen, D. S. and M. E. Everett (2009). 3D polarimetric GPR coherency attributes and full-waveform inversion of transmission data for characterizing fractured rock. *Geophysics 74*(3), J23–J34.

Schaefer, C. E., X. Yang, O. Pelz, D. T. Tsao, S. H. Streger, and R. J. Steffan (2010). Anaerobic biodegradation of iso-butanol and ethanol and their relative effects on BTEX biodegradation in aquifer materials. *Chemosphere 81*(9), 1111–1117.

Schmittbuhl, J., F. Schmitt, and C. Scholz (1995). Scaling invariance of crack surfaces. *Journal of Geophysical Research: Solid Earth 100*(B4), 5953–5973.

Schmoll, O. (2006). *Protecting groundwater for health: Managing the quality of drinking-water sources.* World Health Organization.

Sen, P. N. and P. A. Goode (1992). Influence of temperature on electrical conductivity on shaly sands. *Geophysics 57*(1), 89–96.

Shakas, A. and N. Linde (2015). Effective modeling of ground penetrating radar in fractured media using analytic solutions for propagation, thin-bed interaction and dipolar scattering. *Journal of Applied Geophysics 116*, 206–214.

Shakas, A. and N. Linde (2017). Apparent apertures from ground penetrating radar data and their relation to heterogeneous aperture fields. *Geophysical Journal International 209*(3), 1418–1430.

Shakas, A., N. Linde, L. Baron, O. Bochet, O. Bour, and T. Le Borgne (2016). Hydrogeophysical characterization of transport processes in fractured rock by combining push-pull and single-hole ground penetrating radar experiments. *Water Resources Research 52*, 938–953.

Shakas, A., N. Linde, L. Baron, J. Selker, M.-F. Gerard, N. Lavenant, O. Bour, and T. Le Borgne (2017). Neutrally buoyant tracers in hydrogeophysics: Field demonstration in fractured rock. *Geophysical Research Letters 44*(8), 3663–3671.

Shepard, M. K., R. A. Brackett, and R. E. Arvidson (1995). Self-affine (fractal) topography: Surface parameterization and radar scattering. *Journal of Geophysical Research: Planets 100*(E6), 11709–11718.

Shubitidze, F., K. O'Neill, S. A. Haider, K. Sun, and K. D. Paulsen (2002). Application of the method of auxiliary sources to the wide-band electromagnetic induction problem. *IEEE Transactions on Geoscience and Remote Sensing 40*(4), 928–942.

Singha, K. and S. M. Gorelick (2005). Saline tracer visualized with three-dimensional electrical resistivity tomography: Field-scale spatial moment analysis. *Water Resources Research 41*(5).

Singhal, B. B. S. and R. P. Gupta (2010). *Applied hydrogeology of fractured rocks.* Springer Science & Business Media.

Slater, L. D. and S. K. Sandberg (2000). Resistivity and induced polarization monitoring of salt transport under natural hydraulic gradients. *Geophysics 65*(2), 408–420.

Slob, E., M. Sato, and G. Olhoeft (2010). Surface and borehole ground-penetrating-radar developments. *Geophysics 75*(5), 75A103–75A120.

Snow, D. T. (1969). Anisotropie permeability of fractured media. *Water Resources Research 5*(6), 1273–1289.

Stacy, E. W. (1962). A generalization of the gamma distribution. *The Annals of mathematical statistics*, 1187–1192.

Stauffer, F., P. Bayer, P. Blum, N. M. Giraldo, and W. Kinzelbach (2013). *Thermal use of shallow groundwater.* CRC Press.

Swanson, R. D., A. Binley, K. Keating, S. France, G. Osterman, F. D. Day-Lewis, and K. Singha (2015). Anomalous solute transport in saturated porous media: Relating transport model parameters to electrical and nuclear magnetic resonance properties. *Water Resources Research 51*(2), 1264–1283.

Swanson, R. D., K. Singha, F. D. Day-Lewis, A. Binley, K. Keating, and R. Haggerty (2012). Direct geoelectrical evidence of mass transfer at the laboratory scale. *Water Resources Research 48*(10).

Taflove, A. and S. C. Hagness (2005). *Computational electrodynamics.* Artech house.

Talley, J., G. S. Baker, M. W. Becker, and N. Beyrle (2005). Four dimensional mapping of tracer channelization in subhorizontal bedrock fractures using surface ground penetrating radar. *Geophysical Research Letters 32*(4).

Tang, D. H., E. O. Frind, and E. A. Sudicky (1981). Contaminant transport in fractured porous media: Analytical solution for a single fracture. *Water Resources Research 17*(3), 555–564.

Tarantola, A. (2005). *Inverse problem theory and methods for model parameter estimation.* SIAM.

Tenchine, S. and P. Gouze (2005). Density contrast effects on tracer dispersion in variable aperture fractures. *Advances in Water Resources 28*(3), 273–289.

Thakker, K. D. (1998). An overview of health risks and benefits of alcohol consumption. *Alcoholism: Clinical and Experimental Research 22*(S7), 285s–298s.

Thompson, M. E. and S. R. Brown (1991). The effect of anisotropic surface roughness on flow and transport in fractures. *Journal of Geophysical Research: Solid Earth 96*(B13), 21923–21932.

Tilman, D. and M. Clark (2014). Global diets link environmental sustainability and human health. *Nature 515*(7528), 518–522.

Tsang, C. and I. Neretnieks (1998). Flow channeling in heterogeneous fractured rocks. *Reviews of Geophysics 36*(2), 275–298.

Tsang, C., I. Neretnieks, and Y. Tsang (2015). Hydrologic issues associated with nuclear waste repositories. *Water Resources Research 51*(9), 6923–6972.

Tsang, Y. (1992). Usage of "equivalent apertures" for rock fractures as derived from hydraulic and tracer tests. *Water Resources Research 28*(5), 1451–1455.

Tsang, Y. and C. Tsang (1987). Channel model of flow through fractured media. *Water Resources Research 23*(3), 467–479.

Tsang, Y. and C. Tsang (1989). Flow channeling in a single fracture as a two-dimensional strongly heterogeneous permeable medium. *Water Resources Research 25*(9), 2076–2080.

Tsang, Y., C. Tsang, I. Neretnieks, and L. Moreno (1988). Flow and tracer transport in fractured media: A variable aperture channel model and its properties. *Water Resources Research 24*(12), 2049–2060.

Tsoflias, G. P. and M. W. Becker (2008). Ground-penetrating-radar response to fracture-fluid salinity: Why lower frequencies are favorable for resolving salinity changes. *Geophysics 73*(5), J25–J30.

Tsoflias, G. P., T. Halihan, and J. M. Sharp (2001). Monitoring pumping test response in a fractured aquifer using ground-penetrating radar. *Water Resources Research 37*(5), 1221–1229.

Tsoflias, G. P. and A. Hoch (2006). Investigating multi-polarization gpr wave transmission through thin layers: Implications for vertical fracture characterization. *Geophysical Research Letters 33*(20).

Tsoflias, G. P., C. Perll, M. Baker, and M. W. Becker (2015). Cross-polarized GPR imaging of fracture flow channeling. *Journal of Earth Science 26*(6), 776–784.

Tsoflias, G. P., J.-P. Van Gestel, P. L. Stoffa, D. D. Blankenship, and M. Sen (2004). Vertical fracture detection by exploiting the polarization properties of ground-penetrating radar signals. *Geophysics 69*(3), 803–810.

UN (2017). World population prospects: The 2017 revision, key findings and advance tables. Technical Report ESA/P/WP/248, United Nations, Department of Economic and Social Affairs, Population Division.

USDoE (2016). International energy outlook 2016 with projections to 2040. Technical Report DOE/EIA-0484(2016), United States Energy Information Administration, Department of Energy.

Velde, B., J. Dubois, D. Moore, and G. Touchard (1991). Fractal patterns of fractures in granites. *Earth and Planetary Science Letters 104*(1), 25–35.

Wang, J., T. Narasimhan, and C. Scholz (1988). Aperture correlation of a fractal fracture. *Journal of Geophysical Research: Solid Earth 93*(B3), 2216–2224.

Wang, L. and M. B. Cardenas (2014). Non-fickian transport through two-dimensional rough fractures: Assessment and prediction. *Water Resources Research 50*(2), 871–884.

Wang, L., M. B. Cardenas, D. T. Slottke, R. A. Ketcham, and J. M. Sharp (2015). Modification of the local cubic law of fracture flow for weak inertia, tortuosity, and roughness. *Water Resources Research 51*(4), 2064–2080.

Warren, C., A. Giannopoulos, and I. Giannakis (2015). An advanced GPR modelling framework: The next generation of gprMax. In *Advanced Ground Penetrating Radar (IWAGPR), 2015 8th International Workshop on*, pp. 1–4. IEEE.

Watanabe, K. and H. Takahashi (1995). Fractal geometry characterization of geothermal reservoir fracture networks. *Journal of Geophysical Research: Solid Earth 100*(B1), 521–528.

WHO (2017). Global status report on water safety plans: A review of proactive risk assessment and risk management practises to ensure the safety of drinking-water. Technical Report CC BY-NC-SA 3.0 IGO, Geneva.

Widess, M. (1973). How thin is a thin bed? *Geophysics 38*(6), 1176–1180.

Witherspoon, P. A., J. S. Wang, K. Iwai, and J. E. Gale (1980). Validity of cubic law for fluid flow in a deformable rock fracture. *Water Resources Research 16*(6), 1016–1024.

Yurkin, M. A. and A. G. Hoekstra (2007). The discrete dipole approximation: An overview and recent developments. *Journal of Quantitative Spectroscopy and Radiative Transfer 106*(1), 558–589.

Zhdanov, M. S., R. B. Smith, A. Gribenko, M. Cuma, and M. Green (2011). Three-dimensional inversion of large-scale EarthScope magnetotelluric data based on the integral equation method: Geoelectrical imaging of the Yellowstone conductive mantle plume. *Geophysical Research Letters 38*(8).

Zimmerman, R. W. and G. S. Bodvarsson (1996). Hydraulic conductivity of rock fractures. *Transport in Porous Media 23*(1), 1–30.

Zimmerman, R. W. and I.-W. Yeo (2000). Fluid flow in rock fractures: from the Navier-Stokes equations to the cubic law. *Dynamics of Fluids in Fractured Rock*, 213–224.

Appendix A

Appendix A: The Effective-Dipoles MATLAB code

In this appendix, we include a MATLAB code which implements the effective-dipoles modeling framework for a planar and rectangular fracture with homogeneous properties. The procedure to assign heterogeneous properties to the fracture is also explained but no code is included to create heterogeneity. When using this code, please cite Shakas and Linde (2015).

The effective-dipoles code can be implemented in three simple steps:

1. Create a dipole grid using the function Dipole_Grid.m
2. Create a source signature using the function Source.m
3. Run the forward model using the function Effective_Dipoles.m

The Dipole_Grid(1,2,3,4,5,6,7,8,9,10) takes the following 10 arguments:

1. Horizontal displacement of the fracture midpoint from the origin (cm)
2. Vertical displacement of the fracture midpoint from the origin (cm)
3. Fracture length (cm)
4. Fracture width (cm)
5. Fracture dip (rad)
6. Fracture azimuth (rad)
7. Fracture thickness (cm)
8. Relative electrical permittivity of fracture filling (-)
9. Electrical conductivity of fracture filling (S·m^{-1})
10. the side length of each dipole element (cm)

All arguments are real-valued positive (single) numbers. The 10th argument denotes the discretization density, and it is suggested (see sec. 2.4.4) to use at least 4 dipoles per signal dominant wavelength in the rock matrix (e.g., for a 100 MHz antenna, the wavelength in granite is ~ 100 cm (with $\varepsilon_r = 9$) so a discretization of 25 cm per dipole element should be used. The output of this function is an $m \times 9$ matrix, where m is the number of dipole elements that constitute the fracture. A fracture with dip = 0° and azimuth = 0° is oriented along the $\hat{y} - \hat{z}$ plane, and increments in the horizontal displacement move the fracture

127

along the positive $\hat{x}$-axis, while vertical displacements move the fracture midpoint along the positive $\hat{z}$-axis.

The Source(1,2,3,4,5) takes the following 5 arguments:

1. α parameter of the gamma distribution
2. β parameter of the gamma distribution
3. γ parameter of the gamma distribution
4. ϕ parameter of the gamma distribution
5. vector consisting of frequency values (GHz) at which the response is computed

The first four arguments are real-valued positive (single) numbers while the fifth argument is an n-valued vector, consisting of the frequencies at which the response is computed. The output of this function is also an n-complex valued vector, consisting of the source phase and amplitude at each frequency. For a description of how the source is computed, see sec. 2.4.2.

The Effective_Dipoles(1,2,3,4,5,6,7,8,9) takes the following 9 arguments:

1. vector consisting of frequency values (GHz) at which the response is computed
2. Relative electrical permittivity of rock matrix (-)
3. Electrical conductivity of rock matrix (S·m^{-1})
4. source vector computed by Source.m
5. source (x, y, z) location (cm)
6. source $(\hat{x}, \hat{y}, \hat{z})$ orientation (unitless, relative values from 0 to 1)
7. receiver (x, y, z) location (cm)
8. receiver $(\hat{x}, \hat{y}, \hat{z})$ orientation (unitless, relative values from 0 to 1)
9. matrix with element properties computed from Dipole_Grid.m

In the last page of this appendix we include an example that simulates the GPR reflection along an $5\,\text{m} \times 5\,\text{m}$ fracture, with dip $= 0°$, azimuth $= 0°$, aperture $= 1$ mm, that is water filled with electrical properties $\varepsilon_r = 81$ and $\sigma = 0.1\,\text{S·m}^{-1}$. In this example, a GPR source with a dominant wavelenth of 100 MHz is created and oriented along the $\hat{z}$ axis. The source-receiver separation is set to 1 m and the rock matrix properties are chosen to represent a low-loss granitic formation ($\varepsilon_r = 9$ and $\sigma = 0.001\,\text{S·m}^{-1}$). The response is computed at 500 linearly-spaced frequencies, from 0 to 300 MHz, and at 50 linearly-spaced heights along the z-axis ($-5\text{m} \leq z \leq 5\text{m}$). Finally, the frequency response is zero-padded (upsampling) and the Fourier Transform is computed to give the response in the time domain, that is then normalized and plotted as a GPR setion. Fig. A.1 shows the (a) modeling domain, (b) the GPR reflection data along all transmitter-receiver pairs and (c) the middle trace from (b). The code to create these figures is also included.

```matlab
%% Dipole grid creation
function [d_grid] = Dipole_Grid(r,h,L,W,dip,azimuth,thck,perm,sigma,dL)
    % Compute the bounds ot the dipole grid, grid spacing and element area
    Lb = (L/2)*(1-dL/L);
    Wb = (W/2)*(1-dL/W);
    dW = dL;
    A = dL*dW; % element area
    % Create initial midpoints for each element
    z_locations = -Lb:dL:Lb;
    y_locations = -Wb:dW:Wb;
    x = zeros(numel(z_locations),numel(y_locations));
    y = repmat(y_locations,[numel(z_locations), 1]);
    z = repmat(z_locations,[1, numel(y_locations)]);
    % Create a rotation matrix
    CM = Rotation(dip, azimuth);
    % Find new locations of dipoles
    d_loc = CM*[ x(:) y(:) z(:) ]';
    % Translate the rotated dipoles along x (radius) and z (height)
    d_trans = d_loc' + repmat([r 0 h],[numel(x) 1]);
    % Create the final dipole matrix
    % Each row corresponds to one dipole element,
    % and each column to the following element properties (9 columns)
    % d_grid [(1) X [cm], (2) Y [cm], (3) Z [cm], (4) Dip [rad],
    % (5) Azimuth [rad], (6) Area[cm^2], (7) Aperture [cm],
    % (8) El. Permittivity [-], (9) El. Conductivity] S/m]
    d_grid = [d_trans, repmat([dip azimuth A thck perm sigma],[size(d_trans,1),1])];
end

%% Source creation
function [source] = Source(a, b, g, ph, f)
    % This function generates a dipole moment that is used for the antenna
    % source. The dipole moment is a generalized gamma distribution that is
    % generated using three shape parameters (a, b, g) and a complex phase
    % (ph). Generate the spectrum based on eq. 11 of the referenced paper
    c = 29.9792458; % cm/ns
    source_spectrum = (f.^(a*g-1)).*exp(-(f/b).^g)*exp(1i*ph);
    C = (10^12)/(4*pi*c^2);
    source = source_spectrum*C;
    source(isnan(source)) = 0;
    source(isinf(source)) = 0;
end

%% Run the effective-dipoles code
function [F] = Effective_Dipoles(f, beps, bsig,...
                                 source, s_loc, s_or, r_loc, r_or, dipoles)
    % Multiply the source vector (nx1) with the source orientation (1x3)
    source = bsxfun(@times, source(:), s_or(:)');
    Ndipoles = size(dipoles,1); % Number of dipoles
    d_rsp = nan(length(f), 3, Ndipoles); % Initialize matrix
```

```matlab
    % Compute the dipole response of the source
    parfor d = 1 : Ndipoles
        d_rsp(:,:,d) = Dipole_Response(f, beps, bsig, source,...
                                       s_loc, dipoles(d,:));
    end
    % Initialize coupled dipole and receiver matrices to save responses
    cd_rsp = d_rsp;
    receiver = nan(length(f), 3, Ndipoles);
    parfor d = 1 : Ndipoles
    % Propagation back to the receiver
    receiver(:,:,d) = Propagation(cd_rsp(:,:,d),...
                        dipoles(d,1:3), r_loc, f, beps, bsig);
    end
    % Remove potential nans before summation
    receiver(isnan(receiver)) = 0;
    % Sum up the contributions from all the dipoles
    Fv = squeeze(sum(receiver,3));
    % Calculate component along receiver axis
    F = r_or*Fv';
end

%% Dipolar scattering
function [F] = Dipole_Response(f, epsilon, sigma, source, s_loc, dipole)
    % Rotation(dip, azimuth) for each dipole
    d_c = Rotation(dipole(4), dipole(5));
    % propagation from source to dipole
    p_d = Propagation(source, s_loc, dipole(1:3), f, epsilon, sigma);
    % Polarization response of each dipole element
    d_p = Polarization(f, epsilon, sigma, dipole(6), dipole(7), ...
            dipole(8), dipole(9));
    % Component of source on dipole and polarization effect
    F = d_p.*(d_c*p_d')';
end

%% Dipole polarization
function [pol] = Polarization(f,eps,sig,e_area,e_thck,e_perm,e_cond)
    % Wavenumer in rock matrix and in dipole element
    k1 = Wavenumber(f, eps, sig);
    k2 = Wavenumber(f, e_perm, e_cond);
    % Fresnel reflection coefficients with zero incident angle
    rcTE = (k1-k2)./(k1+k2);
    rcTM = (k1./k2).*rcTE;
    % exponential term within thin-bed
    exponential = exp(-2i*e_thck*k2);
    % Thin bed reflection coefficients
    tbrTE = rcTE.*(1 - exponential)./(1-(rcTE.^2).*exponential);
    tbrTM = rcTM.*(1 - exponential)./(1-(rcTM.^2).*exponential);
    % Polarization vector
    pol = bsxfun(@rdivide,1i*e_area*[tbrTM(:) tbrTE(:) tbrTE(:)],pi*f(:));
```

```matlab
end

%% Propagation in the background dielectric (dipole radiation pattern)
function [F] = Propagation(source, source_location, ...
    observation_location, f, epsilon, sig)
    r = (observation_location-source_location);% source to receiver vector
    nr = sqrt(sum(r.^2)); % distance
    rh = r/nr; % direction
    k = Wavenumber(f, epsilon, sig);
    k2 = k.^2; % squared wavenumber
    dot_prod = bsxfun(@times,rh,source*rh(:)); % dot product in equation
    F = bsxfun(@times,(bsxfun(@times,1i*k + 1/nr, ...
        3*dot_prod - source)/nr^2 + ...
        bsxfun(@times, k2, (rh*rh')*source - dot_prod)/nr), exp(-1i*k*nr));

end

%% Dipole component on fracture plane
function [CM] = Rotation(dip, azi)
    cd = cos(dip);
    sd = sin(dip);
    ca = cos(azi);
    sa = sin(azi);
    % component matrix => A*D
    CM = [  ca*cd    sa      -ca*sd;
           -sa*cd    ca       sd*sa;
            sd       0        cd  ];
end

%% Complex wavenumber computation
function [F] = Wavenumber(f, eps, sig)
    % variables are frequency (fr - GHz) relative permittivity (unitless)
    % and conductivity (sig - S m^-1). Speed of light c = 29.9792458 cm/ns
    F = sqrt(eps)*2*pi*f(:).*(sqrt(sqrt(0.25 +...
        (9*sig./(f(:)*eps)).^2) + 0.5) -...
        1i*sqrt(sqrt(0.25 + (9*sig./(f(:)*eps)).^2) - 0.5))/29.9792458;
end
```

```matlab
%% Example simulation
%% Create frequency vector (GHz) and source
f = linspace(0,0.3,500);
GPR_source = Source(3, 0.05, 2, 0, f);
%% Create source and receiver positions and orientations
midpoint = -500 : 50 : 500; traces = numel(midpoint);
Tx_pos = [zeros(traces,2), (midpoint(:)-50)]; % source position, 50 cm below midpoint
Rx_pos = [zeros(traces,2), (midpoint(:)+50)]; % receiver position, 50 cm above midpoint
Tx_or = repmat([0 0 1], [traces,1]);
Rx_or = repmat([0 0 1], [traces,1]);
%% Create the dipole grid
[d_grid] = Dipole_Grid(600, 0, 500, 500, 0, 0, 0.1, 81, 0.1, 25);
%% Run the forward simulation for every midpoint location (can run in parallel)
data = zeros(numel(f),traces); % allocate memory
for k = 1:traces
    data(:,k) = Effective_Dipoles(f, 9, 0.001, GPR_source,...
        Tx_pos(k,:), Tx_or(k,:), Rx_pos(k,:), Rx_or(k,:), d_grid);
end
%% Upsample and normalize data in the time domain
dtime = real(fft(padarray(data,5*numel(f),'post')));
dtime = dtime/max(dtime(:));
time_axis = linspace(0,1/min(abs(diff(f))),size(dtime,1));
%% Plotting
% The first figure shows the modeling setup. The center of each element
% is plotted with an asterisk, the transmitter locations with a square
% and the receiver locations with a solid circle.
figure()
scatter3(d_grid(:,1),d_grid(:,2),d_grid(:,3),30,[1,0,0],'*')
hold on
axis equal
set(gca,'XLim',[0,1000],'YLim',[-500,500],'ZLim',[-500,500])
scatter3(Tx_pos(:,1),Tx_pos(:,2),Tx_pos(:,3),60,[0,0,1],'s')
scatter3(Rx_pos(:,1),Rx_pos(:,2),Rx_pos(:,3),20,[0,0,0],'filled')
xlabel('x (cm)'); ylabel('y (cm)'); zlabel('z (cm)')
view([1,1,0.6])
hold off
% Here we plot the GPR section computed from the model above
figure()
hold on
set(gcf,'Position',[0,0,600,600])
imagesc(time_axis,midpoint/100,dtime')
axis tight
set(gca,'XLim',[80,180])
caxis(max(abs(dtime(:)))*[-1,1])
colormap('jet')
ylabel('Midpoint height (m)')
xlabel('Time (ns)')
% This figure is the middle trace from the section above
figure()
```

```
set(gcf,'Position',[0,0,600,300])
hold on
plot(time_axis,dtime(:,round(traces/2)))
set(gca,'XLim',[80,180])
ylabel('Norm. Electric Field (-)')
xlabel('Time (ns)')
```

(a)
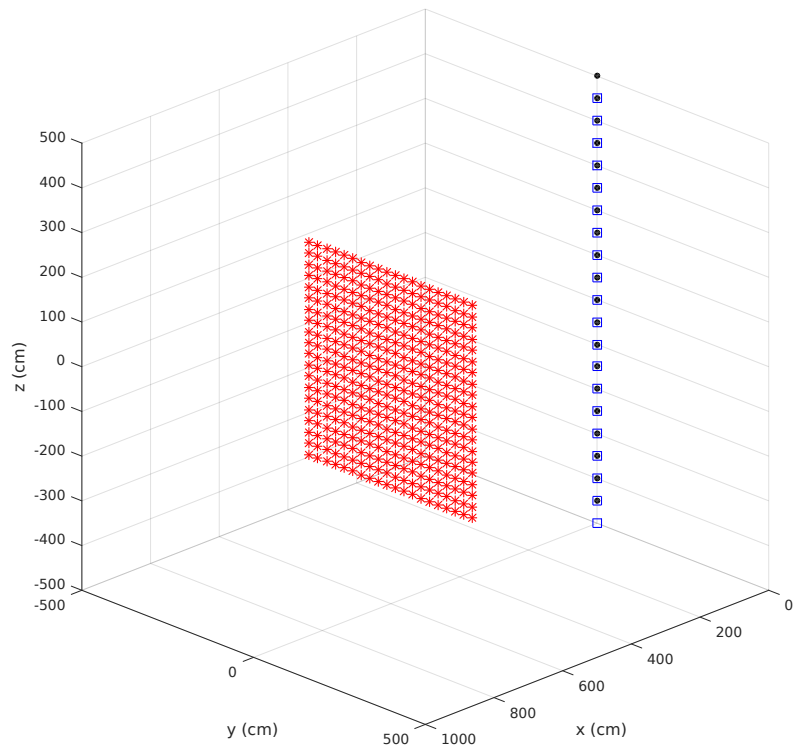
(b)
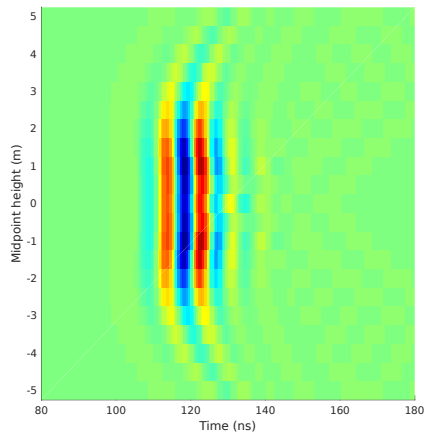
(c)
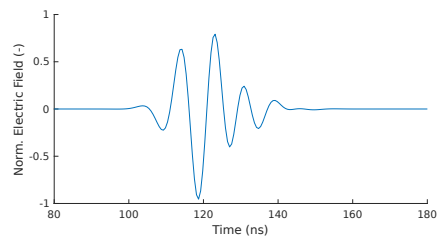
Figure A.1 – The three figures produced from the example given above. (a) The model on which the simulation is performed showing the fracture dipole locations (red asterisks), the transmitter (blue squares) and receiver (filled black circles) locations. (b) The GPR reflection data computed along the transmitter-receiver pairs. (c) The middle trace from (b).

Acknowledgements

It's tough to pinpoint all the events that lead to the completion of this thesis, and granted that many of them are probably random, I will try my best to highlight the ones that I am aware of. Apart from the important factor of a 4-year funding from the Swiss National Science Foundation, which I thank dearly, it is mainly due to people and experiences along the way that I made it to the end of these four years. The following is a synopsis of these; I apologize in advance for those who should be but are not mentioned.

In research, it is important to have objectives, e.g., to make interesting questions that can (hopefully) be answered within the time frame of a PhD. I thank **Niklas** not only for finding the time to ask but also to help answer these questions with me. His door was always open and his mind always sharp.

Collaborations and help from other researchers were essential along the way. I thank **Ludovic** for making fieldwork effective (and amusing!) and for all the bright discussions we had, **Olivier Bour** for his good humor and insightful feedback in manuscript submissions and **Tanguy Le Borgne** for his friendly presence and scientific input (and a great weekend in île-Grande!). I also thank the committee members, **Klaus Holliger**, **Stewart Greenhalgh** and **Philippe Davy** for the fruitful discussion during my defense (and yearly committees), as well as the president of the jury, **Michel Jaboyedoff** for his availability.

Géopolis is not the finest of university buildings for my taste - and not only because of the window blinds that automatically close twice a day, precisely at 12:20 and 18:02 pm on the North side of the building. Yet it can be a fun place if you have the right people around you. For this I thank **Sté** for Gloryland breaks (and for saying what she thinks), **Mike** for chess breaks (and warm hugs), **Nadja** for always smiling, **Vjeran** for keeping the hallway in order, **Magali** for helping out with pen smuggling from AGU, **Pietro** for spending time to discuss (or mostly argue, which I still appreciate), **James** for his funny stories, **Carmen** for all the tandem hours, **Nathalie** for awesome dance moves, **Renske** for sharing doubts about research, **Marco** for introducing me to the gardening community, **Serdar** for his daily "Hey men", **Aline** for keeping me company on those last few weeks before submission, **Laureline**, **Damien**, **Marina**, **Santiago**, **Tobias** and **Pavel** for making my first year in Lausanne joyful. During my years as a PhD I had a short chance to escape Géopolis and spend a few weeks at the university of Rennes, where my stay was warmly greeted by **Olivier**, **Jérôme**, **Eliot**, **Régis** and several other hydrologists!

"One good thing about music, when it hits you, you feel no pain". Music was definitely essential over the last years and for this I need to thank the music crew: first and foremost my music duo, **Giulia**, for her flawless flute solos, **Benjamin** for his unbeatable beats, **Jürg** for his appreciation of the 'Bare Necessities', **Leanne** for sharing her beautiful voice, **Gab** for his funky rhythms, **Guillaume** for his jazzy melodies, **Giacomo** for his bluesy licks, **Femi** for making music with whatever he could find, **Zoneibe** for repeatedly singing the 'Girl from Ipanema'...and many people who patiently listened or were just around: **Ignes**,**Mor1**, **Erica**, **Elfie**, **Seb**, **Martin**, **Monica**, **Nico**...

Outside of the campus bubble there are several people that made my time worthwhile, and deserve my gratitude: the boys (**Kiril** and **Isvo**) for sharing thoughts over glasses of whiskey, **Flo** for being a great roommate/climbing-buddy/scuba-diving-student, **Mark** for being my tennis-buddy/cocoach, cocoach **Adam** and the whole of LAUSANNE deux... for all those waterpolo moments, the **Crocos** for unforgettable Liverpool tournaments and my landlord **Robert** for taking the time to talk patiently while I practiced French over bottles of wine.

Every visit back home was a boost of energy for me, and for this I thank my close family; **Kanaris** for teaching me the anarchist way since early childhood, **Angelos** for his irony (that I still believe deep inside is a cry for love) and his whole family for the wonderful feasts they organize every time I return, **Alexandros** for his constant spark of energy, **Giorgos**, among other things, for Janis (who was a real pain), **Nikolas** for his support in rough times, **Angeliki** for making our lives brighter day by day and all my **Hadjiloizou** family for their support and delicious olive pies. Also, special thanks to my Finnish family, **Katri**, **Miranda**, **Kuisma**, **Gérard** and the **Pidgeon man**, with which every minute spent is precious.

However, there are a few people that deserve special consideration... I thank my mother **Angela** aka amma for remaining positive despite the circumstances and for responding to my criticism with love, my sister **Natalie** for being strong as a granite (no fractures here) and giving all-or-nothing and **Giulia** for always putting others first, of which I was lucky enough to be one. Finally, to my partner **Anna**: you have helped me mature in ways that no reading could ever do. Thank you for your guidance, patience and love.

To end, a quote that I don't always adhere to but that I find nevertheless ingenious:

> A mind is like a parachute.
> It doesn't work if its not open.
> — Frank Zappa

Alexis Shakas

PhD in Earth Sciences

Chemin de la Motte 8, Lausanne 1018, Switzerland

(+41) 786 856 450 | alexisshakas@gmail.com | alexis.shakas@unil.ch

Education

University of Lausanne (UNIL)   *Lausanne, Switzerland*

Ph.D. in Earth Sciences   *Nov. 2013 - Oct. 2017*

- Thesis title: Characterizing fracture aperture and transport dynamics with hydrogeophysics: Theoretical and experimental advances.

ETH Zurich (ETHZ), TU Delft (TUD), RWTH Aachen (RWTHA)   *Zurich, Switzerland*

M.Sc. in Applied Geophysics - IDEA League   *Sep. 2011 - Aug. 2013*

- Thesis title: Joint inversion strategies for experimental design.

UC San Diego (UCSD)   *California, US*

B.Sc. in Physics   *Sep. 2007 - Jun. 2011*

Work Experience

Professional Association of Diving Instructors (PADI)   *Cyprus; California; Switzerland;*

Scuba Diving Instructor   *Nov. 2006 - present*

- 217 students certified
- More than 2000 dives logged

Google   *Mountain View, California, US*

Software Engineer Intern for Google Earth   *Jun. 2011 - Sep. 2011*

- Implemented an update for Google Earth global bathymetry using sonar and satellite data
- Experience with QGIS, GDAL, GRASS

Scripps Institude of Oceanography   *San Diego, California, US*

Research Assistant   *May. 2010 - Jun. 2011*

- Labwork: Bathymetry and remote sensing data processing.
- Fieldwork: GPS field surveys along the San Andreas fault.

Skills

Programming	MATLAB, Mathematica, Python, Unix scripting
Fieldwork	Ground Penetrating Radar, Gravimetry, Ground Positioning Systems
Languages	Greek (native), English (bilingual), French (fluent), German and Italian (competent)
Hobbies	Playing music, waterpolo coach and player, gardening, cooking.

Honors & Awards

2011	**Student Ambassador**, Google	
2011	**M.Sc. Two Year Scholarship**, EON	
2006	**B.Sc. Four Year Scholarship**, Fullbright Cyprus-America Scholarship Programme	

137

Publications

- **Shakas, A.** and N. Linde (2017). Apparent apertures from ground penetrating radar data and their relation to heterogeneous aperture fields. *Geophysical Journal International*, **209**(3), 1418–1430.
- **Shakas, A.**, N. Linde, L. Baron, J. Selker, M.-F. Gerard, N. Lavenant, O. Bour and T. Le Borgne (2017). Neutrally buoyant tracers in hydrogeophysics: Field demonstration in fractured rock. *Geophysical Research Letters*, **44**(8), 3663–3671.
- Linde N., T. Ricci T., L. Baron, **A. Shakas** and G. Berrino (2017). The 3-D structure of the Somma-Vesuvius volcanic complex (Italy) inferred from new and historic gravimetric data. *Scientific Reports*, **7**:8434.
- **Shakas, A.**, N. Linde, L. Baron, O. Bochet, O. Bour, T. Le Borgne (2016). Hydrogeophysical characterization of transport processes in fractured rock by combining push-pull and single-hole ground penetrating radar experiments. *Water Resources Research*, **52**, 938–953.
- **Shakas, A.** and N. Linde (2015). Effective modeling of ground penetrating radar in fractured media using analytic solutions for propagation, thin-bed interaction and dipolar scattering. *Journal of Applied Geophysics*, **116**, 206–214.

Conferences

- **Shakas, A.**, N. Linde, L. Baron, M.-F. Gerard, N. Lavenant, O. Bour and T. Le Borgne (2016). Fractured-rock hydrogeophysics with electrically conductive and neutrally buoyant tracers. *AGU Fall Meeting Abstracts*, Poster Presentation.
- N. Linde and **A. Shakas** (2016). On Estimation of Fracture Aperture with Ground Penetrating Radar. *AGU Fall Meeting Abstracts*, Poster Presentation.
- **Shakas, A.**, N. Linde, O. Bour and T. Le Borgne (2016). Inference of Fractured Rock Transport Properties by Joint Inversion of Push-Pull and Single-Hole Ground Penetrating Radar Data. *AGU Fall Meeting Abstracts*, Oral Presentation.
- **Shakas, A.**, N. Linde, O. Bour and T. Le Borgne (2015). Inference of Fractured Rock Transport Properties by Joint Inversion of Push-Pull and Single-Hole Ground Penetrating Radar Data. *AGU Fall Meeting Abstracts*, Oral Presentation.
- **Shakas, A.** and H. Maurer (2015). Strategies for joint geophysical survey design. *EGU General Assembly Conference Abstracts*, Oral Presentation.
- **Shakas, A.**, N. Linde, L. Baron, O. Bochet, O. Bour, T. Le Borgne (2014). Characterization of Anomalous Transport in Fractured Rock through the Imaging of Push-Pull Experiments Using Single-Hole Ground Penetrating Radar Reflection Data. *AGU Fall Meeting Abstracts*, Oral Presentation.
- **Shakas, A.** and N. Linde (2014). Analytical modeling of electromagnetic wave propagation and fracture scattering in dielectric media using discretized dipole distributions. *EGU General Assembly Conference Abstracts*, Poster Presentation.

References

Niklas Linde   *University of Lausanne*

Associate Professor in Environmental Geophysics   *Ph.D. Thesis Advisor*

- Inst. des sciences de la Terre, Quartier UNIL-Mouline, Bâtiment Géopolis 3779, Lausanne, CH 1015
- email: niklas.linde@unil.ch, Tel.: +41 21 692 4401

David T. Sandwell   *UC San Diego*

Professor of Geophysics   *B.Sc. Thesis Advisor*

- IGPP 0225, Scripps Institute of Oceanography, La Jolla, CA 92093-0225
- email: dsandwell@ucsd.edu, Tel.: +1 858 534 7109

138